NORTHWESTERN UNIVERSITY

# Modeling Fundamental Processes in Soil-Machine Interaction

A DISSERTATION

SUBMITTED TO THE GRADUATE SCHOOL

IN PARTIAL FULFILLMENT OF THE REQUIREMENTS

for the degree

DOCTOR OF PHILOSOPHY

Field of Civil and Environmental Engineering

By

Zhefei Jin

EVANSTON, ILLINOIS

March 2021

# ABSTRACT

Soil-Machine Interaction (SMI) is ubiquitous on Earth and other planets. Over decades, ground-engaging equipment has been developed and widely used in various engineering applications, including civil construction, agriculture, terrestrial mobility, and even space exploration. However, systematic studies of SMI processes and the corresponding soil behavior are inadequate, which obstructs further advances in the automation and optimization of the machines.

This study focuses on the development of experimental methodologies and efficient computational techniques for promoting the fundamental understanding of loading histories and soil deformation patterns in SMI processes. The work starts from developing and evaluating a novel experimental system consisting of an industrial robot and fluidized bed to enable automated and efficient experimental studies in SMI. The fluidized bed allows a repeatable preparation of a uniform sand bed with a broad range of relative density, and the robot functions as a versatile actuator while simultaneously tracking multiple components of soil reaction acting on the tools. Experiments on fundamental penetration and cutting processes were performed on the newly developed system to observe the soil deformation evolution and measure force-displacement responses.

With the help of the test results on soil deformation, a sequential kinematic method is developed. This method consists of evaluating the incremental displacement field based on

the kinematic method of plasticity and then sequentially updating the deformed configuration. The model was calibrated against experimental results to investigate three fundamental problems: biaxial compression, cutting, and penetration. It is demonstrated that the model can accurately predict the complex response observed in the SMI processes, including soil deformation and force-displacement histories. Although the computational cost is affordable compared to conventional methods such as FEM and DEM, the run time is still high and cannot satisfy the requirement for design optimization and control algorithms used in robotics.

To overcome this limitation with respect to efficiency, a semi-analytical (also known as macro-element) modeling framework, inspired from the generalized yield envelopes widely adopted in geotechnical engineering, is developed. Despite its simplicity, the proposed model can generate force-displacement data in seconds for the loading scenarios of a plate moving translationally and rotationally, considering large deformation in sand. By integrating the experimental studies with the numerical investigations, this work opens opportunities for a comprehensive study on soil-machine interaction in an efficient way.

## Acknowledgments

First of all, I would like to express my greatest appreciation to my Ph.D. advisor Professor James Paul Hambleton, who is the Louis Berger Junior Professor in the Civil and Environmental Engineering Department at Northwestern University. Without his great academic knowledge, continuous encouragement, and dedicated advising, this work would not have been completed. His rigorous attitude towards research, wisdom to conquer challenges, patience and persistence to overcome difficulties, as well leadership skills have greatly influenced my professional growth. Besides, he has always been friendly, understanding, and supportive, which kept me motivated to succeed in my research. I have been extremely lucky to have him as my advisor. I also gratefully acknowledge the funding from the National Science Foundation under Grant Nos. 1742849 and 1846817, which supports all the work in this dissertation.

I would also like to express my sincere gratitude to Professor John Rudnicki, Professor Giuseppe Buscarnera, and Professor Paul Umbanhowar at Northwestern University for serving on my Ph.D. committee and advising me on the write-up of my thesis. Their encouragement and support for my future career are greatly appreciated.

I thank my colleagues in Hambleton's research group: Dr. Zhenhao Shi, Dr. Junyue Tang, Dr. Nima Goudarzi, Ms. Anastasia Nally, Mr. Ting Lu, Mr. Qinghao Yang, Mr. Hyunjin Lee, Mr.Olisaeloka Anazonwu, and Mr. Sam Asa. It was a great pleasure interacting with them both inside and outside of work. I would also like to thank all of my friends

at Northwestern who made my stay at Northwestern such an enjoyable experience. The generous help from the staff of the Department of Civil and Environmental Engineering and Machine shop at Northwestern University is also appreciated.

Finally, I would like to dedicate this thesis to my beloved parents, Jingwei Jin and Qingmin Zhao, who raised me with unconditional love and gave me the best education they can afford. None of this would have been possible without their encouragement and emotional support. My warmest thanks go to lovely WXL who brought great happiness and laughter to my life. His company means a lot to me.

# Table of Contents

# List of Tables

# List of Figures

CHAPTER 1

# Introduction

## 1.1. Background and motivation

Soil-Machine Interaction (SMI), occurring as machines contact, move, and shape soil, is widely observed in the natural and human-made environments. For thousands of years, people have been cutting the soil with plows and other agricultural tools in order to loosen it and increase food production [**9, 10**]. Even with the exclusion of various agricultural applications, the extensive requirements in civil construction (shown in Fig. 1.1(a)) result in movement of trillions of kilograms of soil annually worldwide. This includes residential construction, road construction, and mineral extraction [**11**]. Another important application of SMI is on- and off-road mobility (illustrated in Fig. 1.1(c)). While wheeled [**12, 13, 14, 15, 16, 17**] and tracked [**18, 19, 20, 21**] devices are still of interest, recently, non-traditional legged locomotion (walking or jumping) [**22, 23, 24, 25, 26, 27**] attracts significant attention, since the robot will have a considerable advantage in passing irregular terrains [**28, 25**].

For various SMI applications, the objectives in understanding and predicting the response of soil and machines are different. Considering the application of earthmoving and mobility, for example, one may wish to minimize forces on the machine to optimize its performance and efficiency [**29, 30, 31**]. On the other hand, tractive devices such as grousers tend to push significant volumes of soil as they move across a ground surface and are designed to maximize resistance [**32, 33**]. No matter the specific demand, the understanding of force-time/displacement histories and soil deformation during the process is essential for optimizing

(a) (b) (c)

Figure 1.1. SMI in (a) agriculture [**1**]; (b) civil construction [**2, 3, 4**]; (c) on- and off-road mobility [**5, 6, 7**].

performance. However, problems involving SMI have been mainly considered by those who design the machines rather than those who study the mechanical response of soils, resulting in the current situation that the methods for predicting soil response (force-displacement histories and soil deformation) are underdeveloped. The lack of prediction techniques is a major obstruction to further advances in SMI applications, such as the control, automation, and optimization of the machines, since these applications rely on accurate prediction of the machine's performance characteristics under all possible actions.

Methods for predicting the force-displacement histories during SMI processes in soil are limited. Currently, numerical techniques are the most common methods used to simulate the problems, such as the Finite Element Method (FEM) (e.g., [**34, 35**]), Discrete Element Method (DEM) (e.g., [**36, 37**]), and Material Point Method (MPM) (e.g., [**38, 39**]), but they have limitations. For FEM, the main problems are mesh distortion and the lack of proper continuum material law, where the former results from the inherent feature of large, plastic deformation in SMI. DEM and MPM can avoid the above problems; however, the development of appropriate constitutive models and the determination of model parameters is

a challenge (e.g., [**40**]). In all techniques, the work of validating results through experiments is insufficient, especially with respect to the material properties. Moreover, existing numerical techniques are inefficient, routinely requiring hours, days, or even weeks to complete a single simulation. Efficiency is paramount in algorithms used for the optimization-based SMI applications (such as determining the optimal shape/trajectory of a cutting tool) that typically require hundreds of iterations and faster-than-real-time simulation [**41, 42, 43**]. Analytical methods can instantaneously solve the problems, but they are normally problem-specific and overly simplify the parameters characterizing soil strength and deformability. For example, existing analytical methods for the cutting process are based on earth pressure theories (e.g., [**44, 45**]). These methods often fail to clarify the stage of cutting and do not consider the full process of deformation. Accumulated soil is often neglected entirely or modeled approximately as a surcharge applied to the soil surface. However, both the accumulated material and the undisturbed material can undergo significant deformation, and therefore disregarding the region of accumulated material leads to errors.

In summary, even though SMI problems lie on the interface between geotechnical and mechanical engineering, the previous research focused more on the machines and neglect the response of the soil. This study desires to fill the gap and promote the development of this problem by generating experimental data and developing new computational techniques for predicting force-displacement histories validated through experiments.

## 1.2. Aims of present work

The overarching goal of this study is to generate fundamental experimental data and develop efficient computational techniques for predicting force-displacement histories and

deformation patterns in SMI processes. Given infinite possibilities of material types and motions involved in SMI applications, this work focuses on the case that a plate moves in sand with large translational and rotational displacement. This work takes a step toward building a comprehensive understanding and predictive models for soil-plate interaction under arbitrary loading conditions. Specific research aims are:

1. Establish lab facilities for SMI tests and experimentally elucidate force-displacement histories and characterize soil deformation modes for the most important and fundamental cases, such as pure penetration and cutting process.

2. Formulate, benchmark, and validate a new numerical technique using the plasticity-based Sequential Kinematic Method (SKM) to simulate complete force-displacement histories and soil deformation during the cutting and penetration process, where the SKM consists of evaluating the incremental displacement field based on the kinematic method and sequentially updating the deformed configuration.

3. Construct a semi-analytical model (also known as macro-element model) that is inspired from the generalized yield envelopes, to predict the force-displacement history of a plate moving along an arbitrary complex trajectory and validate the model with experiments.

## 1.3. Outline of thesis

The dissertation is organized according to the research aims and includes six chapters. In each chapter, an introduction, a background specific to that topic and a conclusion are presented in addition to the main content.

Chapter 2 describes the design, operation, and evaluation of a new experimental system for small-scale geotechnical testing. The system consists of an industrial robot and a sand

bed capable of rapid reconstitution using fluidization, enabling automated and efficient experimental study in SMI. In the system, the robot functions as a versatile actuator while simultaneously tracking multiple components of soil reaction acting on attached tools, and the fluidized bed is used for rapid and repeatable preparation of a uniform sand bed over a broad range of relative density.

Chapter 3 presents the experiments performed for observing the evolution of soil deformation in the cutting and penetration process and for constructing the semi-analytical models. Full procedural details are given, along with a preliminary discussion of the results obtained.

Chapter 4 describes a sequential kinematic method for predicting the soil responses for the cutting and penetration processes. The problem of biaxial compression is also considered as a means of examining the performance of the proposed approach as applied to an elementary problem in geomechanics. The numerical formulations of the method are presented and its performance is evaluated by comparing against experimental observation.

Chapter 5 presents a semi-analytical model for predicting the force-displacement response as a plate performs a large translational movement in sand. An in-depth analysis of experimental results is given. Suggested by the test data, the mathematical expressions describing generalized yield envelope and flow rule necessary for the incremental plasticity model are derived. In addition, a summary of the component features and the full derivation of the incremental load-displacement formulation is also presented. Based on that, the model implementation with displacement control is described in detail. The numerical simulations of a plate moving along different trajectories are compared with the experimental results.

Chapter 6 explores the expansion of the semi-analytical model to rotational motions. It is assumed that the plate can perform combined translational and rotational movement. This

chapter's structure is similar to that of Chapter 5, including a description of key features (e.g., generalized yield envelope and flow rule) based on experimental data, model formulation, implementation, and the model evaluation by comparing with physical test results.

Chapter 7 summarizes the main findings of the thesis and suggests some areas of further work.

CHAPTER 2

# Test facilities and sand specimens

## 2.1. Introduction

In SMI processes, the motions of machines are complex and variable. Developing lab facilities capable of implementing the tests with performing required actions quickly and automatically are vital to experimental studies. For this purpose, an industrial 6-axis robot was set up and calibrated, and a sand bed based on the concept of fluidization was constructed, where the robot functions as a versatile actuator moving objects along arbitrary trajectories, while simultaneously tracking multiple components of soil reactions acting on a tool.

The first part of this chapter is concerned with the sand bed used for the physical modeling tests. The design, construction, operation and capability of the fluidized bed is outlined, and the performance of the bed is characterized, showing it allows the repeatable preparation of a uniform sand bed with a broad range of relative density. In the second part, the performance of the industrial robot is evaluated concerning the accuracy of motion control and force measurement. The collaboration of these individual functions and the application of the robot devising SMI problems is assessed by a benchmark test.

## 2.2. Preparation of sand specimens

### 2.2.1. Background

Relative density, defined as the ratio of the difference between the void ratios of a cohesionless soil in its loosest state and existing natural state to the difference between its void ratio in the loosest and densest states, significantly influences soil behaviour. In the laboratory, preparation of large soil samples to a required density is a fundamental step for investigating many problems in geotechnical engineering and terramechanics. For example, Meyer et al. [**46**] studied geosynthetic-soil interaction by performing pull-out tests in a 1.5 m by 0.6 m soil bed; Gottardi et al. [**47**] studied the response of footings under planar loading in sand prepared in a cylindrical tank 0.45 m high and with a 0.45 m inner diameter; Ishigami et al. [**48**] investigated the movement of rovers on loose sand in a 0.12 m deep bed. Traditionally, the reconstitution of dry sand samples is achieved by tamping, vibration and different types of pluviation. These methods are differentiated into two groups: for tamping and vibration, the density of the sample is adjusted after deposition; while for pluviation the density is determined during deposition [**49**].

With tamping, sand is poured in several layers with each layer compressed by a compactor. Using this method, Miura & Toki [**50**] prepared dry sand samples with relative density ranging from 40% to 90% in a 50 mm diameter cylinder, while El Sawwaf & Nazir [**51**] achieved an approximately homogeneous sample with relative densities of 40% and 75% in a 2 m $\times$ 0.6 m rectangular sand bed. Raghunandan et al. [**52**] investigated the influence of tamped layers and compactor drop height on the void ratio and found that neither increasing the number of layers from three to five nor increasing the drop height from 20 mm to 50 mm significantly altered the void ratio. The main drawbacks of tamping are particle crushing

during compaction, low repeatability, and relatively pronounced density variation along the depth [**53**].

Vibration is generally used to prepare medium to dense sand samples. The sample is first prepared in a loose state, and then vibrated under a small amount of surcharge provided by a cap. Byrne [**54**] and White et al. [**55**] successfully used this method to prepare dense sand samples for $1\,g$ laboratory and higher $g$ centrifuge tests, respectively. By monitoring subsidence of the cap, Miura et al. [**56**] obtained specimens with relative densities ranging from 50% to 90% while controlling the percentage error between actual and desired density to less than 1%.

Compared with tamping and vibration, pluviation in air is used more broadly because of its advantages of minimal particle crushing and better repeatability [**57**]. Air pluviation studies indicate that relative densities achieved by this method generally range from 40% to 100% [**58, 57, 59, 49, 60**]. For a given type of sand, the main factors affecting the relative density are the particle drop height, deposition intensity (i.e., mass flow rate), and the mesh size of the grid through which the sand particles fall [**61, 62**]. A higher drop height leads to a larger fall velocity which increases packing density. This trend is only effective for drop heights below a certain maximum, since the particle velocity plateaus at larger drop heights due to air drag [**63**]. For a given drop height, increased deposition intensity decreases deposition density [**64, 65, 66**], since the simultaneous fall of many particles increases inter-particle interference [**59**]. Increased deposition intensity can be achieved by increasing the mesh size of the grid [**64**].

Although air pluviation is arguably the most commonly used method for preparing soil samples [**63, 61, 67, 68, 69**], it is not without drawbacks. First, in each preparation process, the soil initially inside the bed needs to be emptied and then re-poured, which takes time

and manpower if the pluviation is not fully automated. Second, the surface of a pluviation reconstituted sample is typically uneven, requiring levelling by post-deposition vacuuming. Third, uniform low density ($\leq 30\%$) samples are hard to achieve, making pluviation more applicable to studies of medium or dense sand packings. These drawbacks motivate the search for a quicker and more repeatable preparation technique.

Air fluidization can overcome the limitations of the three techniques for reconstituting a sand bed described above (i.e. tamping, vibration, pluviation). The process of fluidization is similar to vibration induced liquefaction in which granular material is converted from a static solid-like state to a dynamic fluid-like state when a fluid (liquid or gas) flows upward through the granular material. Fluidization is widely used in the chemical processing industry for separations, heat transfer operations, and catalytic reactions. Recently, Goldman and co-workers used air-fluidization to reconstitute various beds of granular materials [**70, 24, 22, 71, 72, 73**]. They found that a fluidized bed allows control of the relative density and creation of repeatable homogeneous granular bed states, which were typically composed of $\sim 1\,\mathrm{mm}$ poppy seeds. Beds prepared in this way exhibit a spatially uniform penetration resistance that is highly repeatable. In one process, the bed of particles is reconstituted by fluidization and then settled by defluidization. Different degrees of compaction can be achieved by changing the defluidization rate [**74**]. A dense packing state is realized by slow defluidization while a loose packing state is obtained with rapid defluidization. Generally, varying only the defluidization rate is sufficient to prepare samples with loose to medium packing states. Samples can be densified by other techniques, such as vibration. X-ray absorption measurements confirm that vertical density variations in samples prepared using air fluidization are small, with less than 0.004 variation in the volume fraction [**74**]. The objectives of this part of study are to (1) provide details about using

air-fluidization to reconstitute sand beds; (2) characterize physical properties of sand beds created using this technique; and (3) demonstrate the suitability of this method to prepare sand beds for experiments in shallow-subsurface geotechnics (e.g., soil-pipeline interaction) and terramechanics (e.g., soil-wheel interaction).

### 2.2.2. Fluidized bed devices

**2.2.2.1. Fundamentals of fluidization.** In a gas-fluidized bed, fluidization behaviour differs depending on the superficial gas velocity and particle properties [**75, 76**]. In general, when gas flow is introduced through the porous bottom of a bed of particles, it moves upwards through voids between particles. At low gas velocities, the drag force exerted on each particle is low relative to particle weight, resulting in a static bed. With increasing gas velocity, a critical value is reached at which the upward drag force equals the downward gravitational force, causing the particles to become mobile. At this critical value, the bed is said to be fluidized and exhibits fluid-like behaviour in that it can no longer support internal stresses. With further increases in the gas velocity, the bed begins to bubble. The bulk density of the bed continues to decrease, and the fluidization becomes more violent until particles no longer form a bed but are "conveyed" upwards by the gas flow. Stopping the gas flow causes the particle bed to defluidize in three consecutive stages: a rapid initial stage for bubble escape, an intermediate stage of hindered sedimentation with a constant velocity of solids descent, and a final decelerating stage of solids consolidation [**77**].

Not all particle beds undergo the full process of fluidization and defluidization described above. The specific behavior depends on particle properties, primarily size and density. Based on particle size and density, Geldart categorize particles into Groups A-D [**75, 76**]. Group A designates aeratable particles. These materials (e.g., milk flour) normally have a

small mean particle size and/or low particle density. Beds of these particles can be fluidized at low gas velocities without the formation of bubbles and are subject to the full fluidization-defluidization process. Group B particles form bubbling beds. Most have particles with size between $150\,\mu$m and $500\,\mu$m and density from about 1.4 to $4\,\mathrm{g/cm^3}$. For these particle beds, once the minimum fluidization velocity is exceeded, the excess gas appears in the form of bubbles; in the defluidization process, the particle beds reach their final state as soon as bubbles are expelled [**77**]. Group C particles are cohesive or very fine powders. They are extremely challenging to fluidize and typically exhibit channeling in which gas flow is concentrated in a number of discrete "holes" in the bed. Group D particles form spouting beds and are composed of very large or very dense particles, such as coffee beans and wheat. As the gas velocity is increased, a jet forms in the bed, and the material may potentially be blown out of the bed. In this paper, we use silica sand which is a Group B particle.

Before discussing the design of the fluidized bed device, we review the air flow requirements to achieve particle fluidization. As stated above, the inception of fluidization is triggered when the air velocity reaches a value at which the upward drag force on the bed particles equals the downward gravitational force. Considering the entire bed, this force balance condition occurs when the product of the flow induced pressure drop across the bed and the bed cross-sectional area equals the weight of the soil in the bed [**78**]. The pressure drop across the bed depends on the air velocity, and it has been investigated and described by various models [**79, 80, 78, 81**]. To illustrate the general approach, we characterize the relationship between the pressure drop across the bed $\Delta P$ and the superficial airspeed $v$ (calculated as $Q/A$, where $Q$ is the volumetric air flow rate and $A$ is the cross-sectional bed

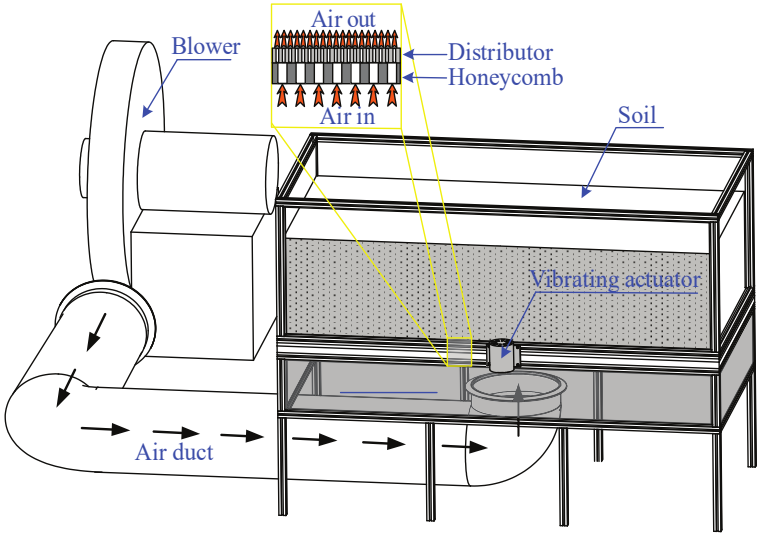


Figure 2.1. Schematic diagram of fluidized bed apparatus.

area) using Ergun's equation:

$$\frac{\Delta P}{L} = \frac{150\mu(1-\epsilon)^2 v}{d^2\epsilon^3} + 1.75\frac{1-\epsilon}{\epsilon^3}\frac{\rho_a v^2}{d}, \tag{2.1}$$

where $L$ is the particle bed height; $\mu$ is the dynamic viscosity of the fluidizing gas; $\rho_a$ is the gas density; $d$ is the average grain diameter; and $\epsilon$ is the bed porosity. The left-hand side of Equation (2.1) equals the unit weight of the particle bed ($\gamma_b$) at the fluidization transition. By transforming $\gamma_b$ to the unit weight of a grain ($\gamma_g$) with the relation $\gamma_b = \gamma_g(1-\epsilon)$, the minimum required flow rate ($Q_{mf} = v_{mf}/A$) for fluidization can be calculated from the relationship:

$$\gamma_g = \frac{150\mu(1-\epsilon)Q_{mf}}{d^2\epsilon^3 A} + 1.75\frac{\rho_a Q_{mf}^2}{d\epsilon^3 A^2}. \tag{2.2}$$

**2.2.2.2. Design of the fluidized bed device.** In principle, a flow of air at the minimum required flow rate ($Q_{mf}$) is required to achieve fluidization; however, in practice, a facility is needed to provide the required airflow. Figure 2.1 illustrates our 150 cm (length) × 75 cm

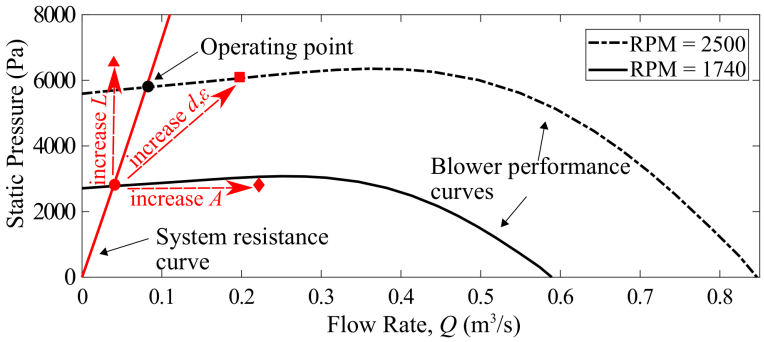


Figure 2.2. Estimated system resistance curve (red) and manufacturer provided blower curves (black) for fluidized bed device. The intersection of blower and system curves determines the operating point. Red arrows indicate new operating points due to changes in size and bed particle properties (see text).

(width) × 50 cm (height) fluidized bed located in the Soil-Structure and Soil-Machine Interaction Laboratory (SSI-SMI Laboratory) at Northwestern University. A centrifugal fan blower driven by a 10 hp three-phase motor (Chicago Blower Corp.) produces the required flow of high-pressure air. The blower is driven by a variable frequency drive controller (model #CFW110028T2ON1Z, WEG), which supports proportional voltage control of the fan speed. The 0-10 V fan speed control signal comes from a USB 6001 DAQ (National Instruments) controlled by a MATLAB program. A duct connects the blower to a 20 cm tall plenum, which pre-distributes the air and whose walls are 1.8 cm thick acrylic recessed in the extruded aluminum rails (80/20 Inc.) of the frame. At the top of the plenum is a 2.54 cm thick layer of steel honeycomb for structural rigidity and flow distribution. Above the honeycomb, a 1.27 cm thick layer of porous plastic with 20 $\mu$m pores (GenPore) forms the distributor. The distributor supports the particles in the bed, and, more importantly, promotes uniform airflow through the particle bed. The vertical space between the sand surface and the top of the apparatus helps to contain the sand.

To understand the design of the fluidized bed device, we first consider how the blower operates. Air enters the blower at atmospheric pressure, and then is pressurized by the blower. This pressure difference drives the air through the duct, plenum, distributor, and bed material. As described in the previous section, to fluidize the particles, the air flow through the bed must reach the minimum required air flow rate ($Q_{mf}$). The air flow rate is determined by both the operating motor speed of the blower and the flow resistance of the entire system. At any fixed motor speed, the blower is characterized by a 'performance curve' (see Figure 2.2), which specifies the relationship between the flow rate through it and the pressure increase across it. Similarly, the passive portion of the system, e.g., the fluidized bed apparatus minus the blower, is characterized by a system resistance for which the pressure drop across it increases monotonically with the flow rate through it. Since $Q$ through the blower and the passive portion of the apparatus are equal and the pressure drops across the blower and apparatus are equal and opposite, the actual operating conditions (i.e., flow rate and pressure drops) are determined by the intersection of the blower and system resistance curves, see Figure 2.2.

The operating point is a function of both system parameters and motor speed. For example, at fixed motor speed, the operating point can range from zero flow rate and finite static pressure when the system is sealed (i.e., infinite system resistance), to finite flow rate and zero static pressure with no load on the blower (i.e., zero system resistance). For a given system resistance curve (e.g., the red line in Figure 2.2), the operating point moves from the red point to the black point as the motor speed is increased from 1740 RPM to 2500 RPM (Revolutions Per Minute). Hence, to fluidize a given bed (corresponding to a fixed system resistance curve), a specific motor speed is needed to produce the required minimum flow rate ($Q_{mf}$). To calculate this speed, the system resistance curve must be known.

By design, the largest resistance in a fluidized bed device comes from the distributor and the particle bed. In most cases, the pressure drop is quadratic in the flow rate [**82**]. Here, the pressure drop across the distributor ($\Delta P_d$) is generalized as $\Delta P_d = \frac{m}{A_d^2}Q^2 + \frac{n}{A_d}Q$, where $A_d$ is the area of distributor, which is the same as the cross-sectional area of bed ($A$); $m$ and $n$ are parameters mainly determined by the hole size, hole number, and thickness of the porous sheet. For air flowing through the bed of particles, the pressure drop can be calculated from Equation (2.1) as $\Delta P_b = \frac{150\mu(1-\epsilon)^2 L}{d^2\epsilon^3 A}Q + 1.75\frac{1-\epsilon}{\epsilon^3}\frac{\rho_a L}{dA^2}Q^2$. Note that to uniformly distribute air flow across the bed, a constraint between the minimum distributor pressure drop and the bed pressure drop is imposed, i.e. $\Delta P_d \geq c\Delta P_b$, where $c$ is proposed to range from 0.02 to 1, with 0.3 as a widely quoted value [**83, 84**]. By combining the pressure drop from the distributor and the bed, the system resistance is characterized as:

$$\Delta P_s = \left(1.75\frac{1-\epsilon}{\epsilon^3}\frac{\rho_a L}{dA^2} + \frac{m}{A^2}\right)Q^2 + \left(\frac{150\mu(1-\epsilon)^2 L}{d^2\epsilon^3 A} + \frac{n}{A}\right)Q. \tag{2.3}$$

Assigning the value of the minimum required flow rate ($Q_{mf}$) to the flow rate ($Q$) in Equation (2.3), the desired operating point ($Q$,$P$) can be located on the system resistance curve, which determines the desired motor speed.

To validate the design methodology, tests of the fluidized bed in the SSI-SMI lab were performed using silica sand, obtained from Ottawa, Illinois (supplied by U.S. Silica Company) and characterized according to ASTM procedures. Figure 2.3 shows the grain-size distribution curve of the sand based on data from the supplier. The particles are round in shape and range in size from 0.075 mm to 0.425 mm with a mean diameter of $D_{50} = 0.19$ mm. Based on the curve, the coefficient of uniformity, $C_u$, and the coefficient of curvature, $C_c$, are 1.61 and 1.03, respectively; hence the sand is classified as poorly-graded (SP). The maximum

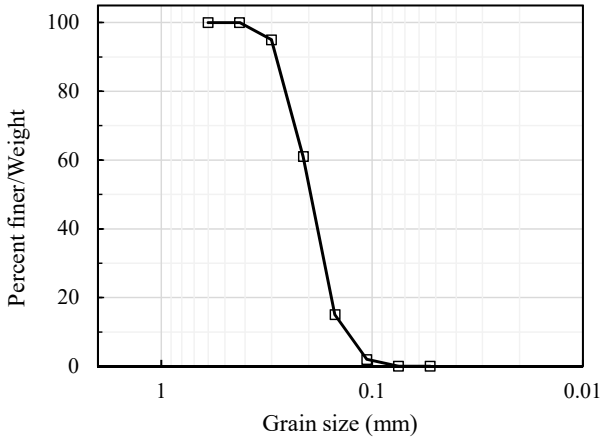


Figure 2.3. Cumulative grain-size distribution of the silica sand (Ottawa) used in this study (data provided by U.S. Silica).

density ($\rho_{max}$) of this sand is measured as 1730 kg/m$^3$ [**85**], and its minimum density ($\rho_{min}$) is 1450 kg/m$^3$ [**86**].

Figure 2.2 shows the actual blower performance curves and the estimated system resistance curve. The parameters used to determine the system resistance curve are $m$ = 26808 Pa·s$^2$/m$^2$, $n$ = 24488 Pa·s/m, $d$ = 0.19 mm, $\gamma_g$ = 26 kN/m$^3$, $L$ = 0.127 m, $\epsilon$ = 0.396, $A$ = 1.125 m$^2$, $\mu = 1.81 \times 10^{-5}$ kg/m·s (at 25 °C), $\rho_a$ = 1.225 kg/m$^3$. Among these parameters, $m$ and $n$ are obtained based on the information provided by the porous layer manufacturer; $d$ is determined from the grain size data provided by U.S. Silica; $\gamma_g$ is approximated as the unit weight of quartz, the main mineral component of Ottawa sand; $L$ is the average height of the sand bed measured before the verification test, which can be used to estimate the bulk density of the bed; and $\epsilon$ is determined by the sand particle density and the estimated bulk density on the premise that the sand is distributed uniformly. Based on the calculation, the minimum required flow rate and airspeed are 0.04 m$^3$/s and 0.035 m/s, respectively. The pressure drop across the distributor and particle bed at fluidization is predicted to be 2763 Pa, which is close to the actual gauge pressure measured in the plenum of 2922 Pa. According

to the above calculation and blower performance curve, the bed of sand should fluidize at a motor speed of 1740 RPM, while the actual value to achieve fluidization is slightly higher at 1780 RPM. The small difference may result from air leaks and the unaccounted for additional resistance from the duct, honeycomb and honeycomb support. Reducing these effects is vital to the efficiency and precise design of the fluidized bed device.

**2.2.2.3. Fluidized bed device capabilities.** The demands on a sand bed for geotechnical model testing vary with the soil properties and bed size. The fluidized bed device can be adjusted to accommodate specific demands, mainly through the selection of the distributor and the operation of the blower. The soil properties affecting the required airflow for achieving fluidization include the unit weight and average diameter of the grains and the soil porosity. Unit weight varies with grain mineral content. Most sand is made of quartz, so the unit weight is generally regarded as constant, i.e., $26\,\mathrm{kN/m^3}$ [**87**]. Consequently, only the influence of grain diameter and porosity are discussed below. With increase of average grain diameter or porosity of the sand bed, the minimum required flow rate increases, which raises the distributor pressure drop ($\Delta P_d$). However, the bed pressure drop ($\Delta P_b$), which equals the weight of sand per unit area, remains constant. Hence, the desired operating point moves to the position with higher static pressure and flow rate (red square symbol in Figure 2.2), which can be reached by increasing the motor speed. Note these desired points in Figure 2.2 are plotted to illustrate the influence of different factors on the airflow requirements, and do not correspond to any specific sand bed.

Now we consider the effects of bed height and the horizontal bed area on the operating point. The height of the sand bed has no influence on the minimum required flow rate and $\Delta P_d$, while $\Delta P_b$ increases linearly. Accordingly, the blower should provide higher pressure with the same flow rate (triangular symbol in Figure 2.2 is the new desired operating point).

Note that a distributor with higher resistance (higher $m$, $n$) might be required to maintain the design constraint $\Delta P_d \geq c\Delta P_b$. Distributor resistance can be increased by increasing thickness, decreasing hole size, or decreasing the number of holes. For the fluidized bed in the SSI-SMI lab, the maximum motor speed is 3600 RPM, at which the blower can produce a maximum pressure around 11960 Pa and a maximum flow rate of 0.7 $m^3/s$. At this speed and with the Ottawa sand described in the previous section, the maximum depth of the fluidized sand bed is 0.72 m. However, in this case, $\Delta P_b \approx 10812$ Pa, and $\Delta P_d \approx 855$ Pa, so the constraint between them, i.e. $\Delta P_d \geq c\Delta P_b$ is not satisfied with $c = 0.3$, and a higher resistance distributor is required to maintain spatially-uniform fluidization. With our existing blower, the deepest sand bed that can be fluidized uniformly is $\approx 0.61$ m deep with $\Delta P_d = 2760$ Pa, which can be accomplished by increasing the current distributor thickness to 4.1 cm.

For sand beds with larger cross-sectional areas, the minimum required flow rate increases, while the minimum required airspeed stays the same. According to Equation (2.3), system resistance remains constant at constant airspeed. Therefore, a higher flow rate but the same static pressure is needed. Correspondingly, the desired operating point is shifted purely horizontally (red diamond symbol in Figure 2.2). When the fluidized bed in the SSI-SMI lab is run at the maximum motor speed, the largest cross-sectional area of the fluidized bed is about 25 $m^2$ which limits the maximum sand bed depth to 0.61 m.

### 2.2.3. Sand bed characterization

In this study, sand beds are prepared using three different operating modes: defluidization only ($DO$), defludization followed by vibration ($DFV$), and defluidization concurrent with vibration ($DCV$). In mode $DO$, the sand settles gradually with decreasing airflow to form the

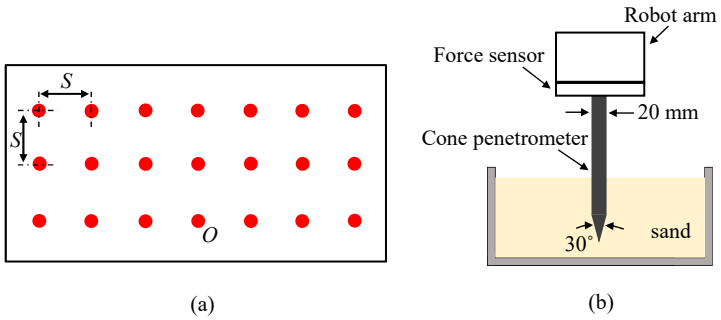


Figure 2.4. (a) Locations of sand height measurements and simple cone penetration tests. (b) Schematic of simple cone penetration measurement.

sample. Mode *DFV* extends the *DO* method by vibrating the sand bed after defluidization for the same time as the defluidization. Mode *DCV* vibrates the bed during defluidization. The vibration in the latter two modes is induced by a vibrating motor (Fasco #D1130) attached to the middle of one side of the fluidized bed frame, as shown in Figure 2.1. In the tests, 227 kg of sand is placed in the bed with an initial mean height of 0.130 m. The sand is fully fluidized by increasing the motor speed to 1780 RPM, at which point the pressure in the plenum ($P_0$) is 2922 Pa. The fully fluidized stage is maintained for 10 s, after which the defluidization stage is started. The motor speed is linearly decreased from 1780 RPM to 0 over a variable defluidization time ($T$) to reduce the pressure and flow rate of air. For each of the three modes listed above, defluidization times ($T$) ranging from 50 s (the stopping time of the blower is $\approx$ 40 s) to nearly 12 hrs are applied to reconstitute the sand beds. The volumetric density and local density of the resulting beds are then measured as described below. Note that in addition to vibration, beds also can be densified by short periodic air pulses [**22**].

**2.2.3.1. Volumetric density.** The volume-based density of the bed ($\rho_v$) is measured as a function of the defluidization time for the three operating modes. To do so, the volume of each reconstituted sand bed is determined with a laser based distance sensor (Leica Disto E7400X)

attached to a six-axis ABB IRB-4400 robot, whose movement is controlled automatically by a computer. First, the distance to the distributor (empty bed) $H_i$ is measured at 21 positions on a uniform 17.5 cm grid, see Figure 2.4(a), as the robot moves the distance sensor in a horizontal plane. Then, after the bed is filled and reconstituted, the distance between the end of the robot arm and the surface of the sand $h_i$ is measured at the same positions. The top of the distributor (bottom of bed) and the reconstituted sand surfaces are nearly flat: $H_i$ varies by less than 0.2 cm and $h_i$ by less than 0.6 cm for all cases. The volume of sand in the bed is then estimated as $V = A(\overline{H_i} - \overline{h_i})$, where $A$ is the bed cross-sectional area and the overline indicates the ensemble average. Assuming uniform sand bed density, the volume-based density of the sand bed is $\rho_v = M/V$, where $M$ is the mass of sand in the bed, and the corresponding relative density is $D_r = \dfrac{\rho_{max}(\rho_v - \rho_{min})}{\rho_v(\rho_{max} - \rho_{min})}$, where $\rho_{max}$ and $\rho_{min}$ are determined in Section 2.2.2.2.

The volume-based relative density of the sand bed increases with the defluidization time $T$ for all cases as shown in Figure 2.5. $D_r$ values ranging from nearly 0.1 to 0.9 are realized. The relative density is logarithmic in the defluidization time, and can be written as $D_r = \alpha \log(\beta T)$. Similar scaling was previously reported by Gravish et al. [**88**]. For the *DCV* mode, a single pair of $\alpha$ and $\beta$ values fit the data over the entire range of $T$. However, for *DO* and *DFV* operating, there are two distinct regions of response. At shorter defluidization times, the increase of $D_r$ with $T$ is noticeably weaker than at longer $T$. In addition, at the same defluidization time, the sample prepared by *DCV* achieves the largest $D_r$, while the sample prepared using *DO* has the lowest $D_r$. Comparing the results obtained from *DO* and *DFV,* the effect of vibration is weakened when the defluidization time is longer than 1400 s for *DFV.*

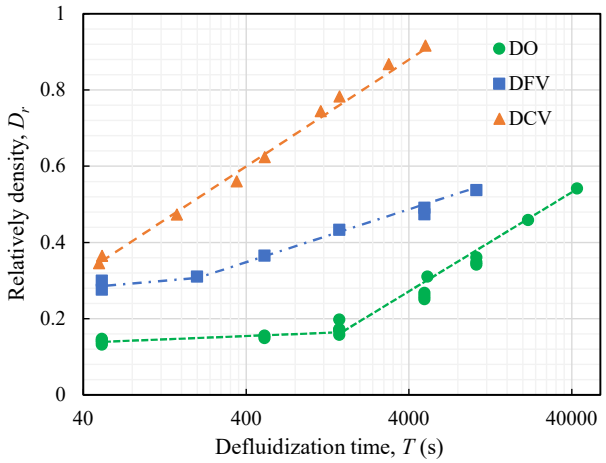


Figure 2.5. Relative density of sand prepared by defluidization only ($DO$), defluidization followed by vibration ($DFV$), and defluidization with concurrent vibration ($DCV$) for various pressure ramp rates.

**2.2.3.2. Local density. Penetration-based density measurement.** In addition to the volume-based density measurements described above, local density measurements can be used to characterize the bed homogeneity. In geotechnical engineering, local density is obtained using the cone penetration test (CPT) by acquiring information of *in situ* soil properties. In this study, for the sake of simplicity, we use the simple cone penetration test, which is widely adopted in terramechanics for determining soil trafficability [**89, 90, 91, 92, 93, 94, 95, 96**]. The test uses the robot arm to drive a penetrometer into the soil at a fixed velocity while recording the total resisting force on the penetrometer with a force sensor. Our penetrometer geometry (30° circular cone tip and a 3.2 $\mathrm{cm}^2$ base) is inspired by a United States Army Corps of Engineers Waterways Experiment Station penetrometer design [**89**]. The resistive forces and moments acting on the penetrometer are measured by a six-axis load cell (Sunrise Instruments #3314C) installed at the end of the robot arm, as illustrated schematically in Figure 2.4(b). The sensor simultaneously measures forces in three mutually perpendicular directions and torques about three corresponding axes, but

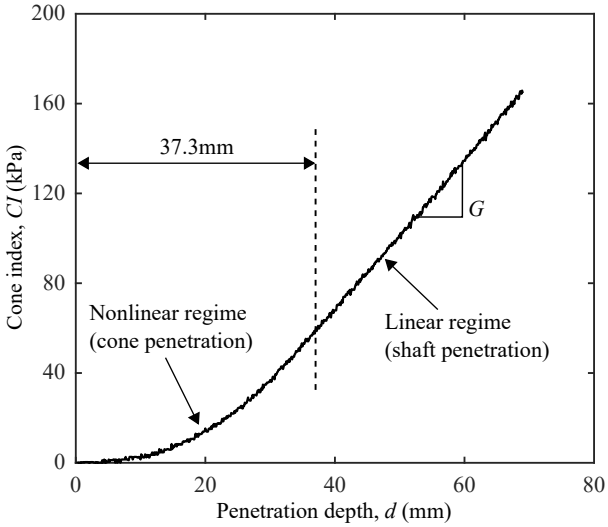


Figure 2.6. Illustration of a cone index profile (mode $DCV$ with $T = 3000\,\mathrm{s}$), where $G$ is the slope in the shaft penetration regime (see text).

only the vertical resistive force is used in this study. At each location tested, the cone penetrometer penetrated the soil to a depth of about 80 mm at a speed of 1 mm/s. The cone index ($CI$) characterizes the penetration resistance [**89**], and is defined as the force per base area required to penetrate the cone into the soil. A typical cone index profile for dry sand is illustrated in Figure 2.6 and consists of two stages: an initial non-linear with depth cone penetration regime followed by a linear with depth shaft penetration regime.

Previous studies indicate that factors affecting $CI$ include moisture content, density, and soil type. To illustrate the effects of different defluidization modes and times $T$, Figure 2.7 presents plots of $CI$ versus depth obtained at location $O$ in the prepared bed [see Figure 2.4(b)]. The $CI$ profiles become steeper with increasing $T$ for all defluidization modes and differ between modes for the same $T$. In all cases, $CI$ increases linearly with depth in the shaft penetration regime.

In simple cone penetration tests, local soil properties are inferred from $CI$ and the linearity of the cone index profile [**97, 98, 94**]. In the shaft penetration regime (cone fully

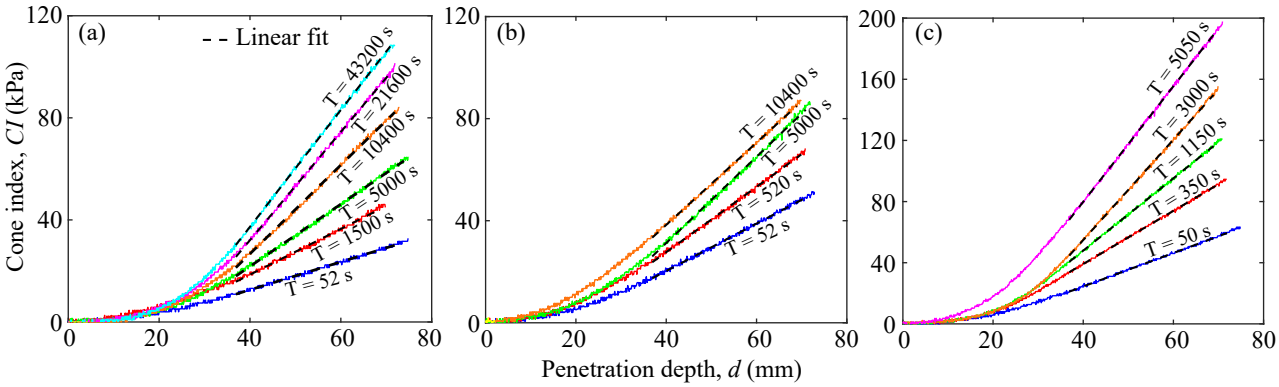


Figure 2.7. Cone index profiles of reconstituted beds prepared with various defluidization times for (a) *DO,* (b) *DFV,* and (c) *DCV.*

submerged), a linear relation between $CI$ and depth indicates a uniform density [**99**]. The slope of the cone index curve, $G$, can be directly related to density [**94**]:

$$\rho = a \ln(G/b), \tag{2.4}$$

where $a$ and $b$ are constants dependent on soil type.

To determine the bed density from $G$, constants $a$ and $b$ from Equation (2.4) must be determined. To do so, cone penetration tests are performed on 150 mm deep pluviated samples of known density in a cylindrical container (diameter = 400 mm). Different sample densities were achieved by varying the pluviator hole size and the uniform grid spacing of the holes (2 mm holes spaced by 25 mm, 4 mm holes spaced by 20 mm, and 6 mm holes spaced by 20 mm) and by placing the pluviator at various initial heights (15.2 cm, 30.5 cm, 71.0 cm, and 91.5 cm) above the soil surface. The penetrometer is inserted along the central axis of the cylindrical container, and at least three samples are prepared and tested at the same nominal density. By fitting the data to Equation (2.4) as shown in Figure 2.8(a), the constants $a$ and $b$ of the calibration curve are determined to be 110.6 kg/m$^3$ and 7.1 $\times$ $10^{-4}$ kN/m$^3$,

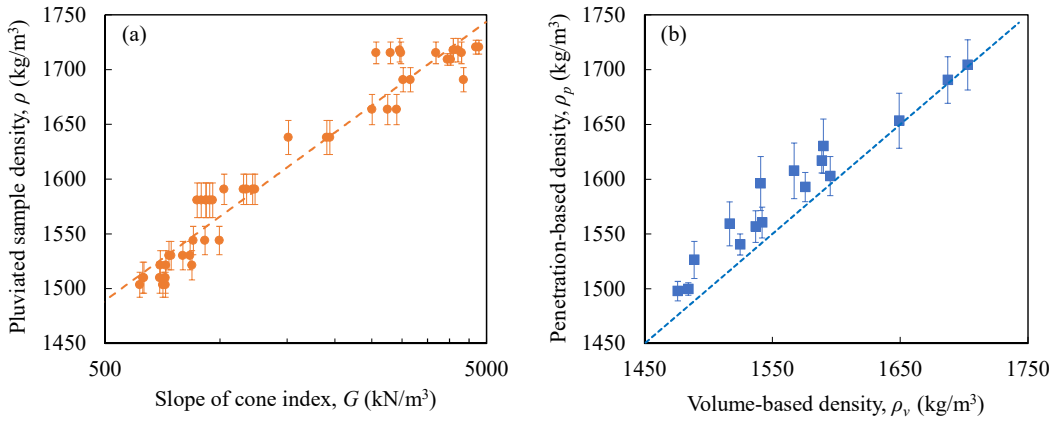


Figure 2.8. (a) Volume-based densities vs. dimensionless slopes of cone index curve for samples prepared by pluviation. Dashed line is a fit to Equation (2.4) and is used to determine fit parameters $a$ and $b$ (see text). (b) Comparison of volume-based and penetration-based density measurements for various defluidization rates and modes.

respectively with $R^2 = 0.94$. Using the calibration equation [Equation (2.4)] and the slope of the cone index curve, local densities can be calculated at any location in the bed. This method has its limitations, but it does provide a fast and simple indication of density, which is the objective of this test.

To assess the reliability of the penetrometer-based approach, the volume-based and penetrometer-based bed densities of various reconstituted sand beds are compared in Figure 2.8(b). The penetrometer-based density ($\rho_p$) is the mean of the densities obtained from the 21 bed positions, and the volume-based density ($\rho_v$) is determined as described in Section 2.2.3.1. The penetrometer-based densities are in good agreement with the volume-based values (coefficient of determination $R^2 = 0.78$), indicating that the sand density in the bed can be determined using the calibration curve. Note that the penetrometer-based densities are slightly larger than the volume-based values for $\rho_v < 1600\,\mathrm{kg/m^3}$; the reason for this discrepancy is not yet understood.

**Density variation with depth.** A linear relation between $CI$ and depth in the shaft penetration regime (see Figure 2.6) indicates a uniform density [**99**]. Accordingly, we characterize any variation in bed density with depth by examining the linearity of the cone-index profiles in the shaft-penetration regime.

Typical cone index profiles (obtained at location $O$ in the bed, see Figure 2.4(b)) are presented in Figure 2.7 and appear to be quite linear in the shaft-penetration regime. To quantify any possible variation, a linear regression is performed on the data in the shaft penetration regime for the three defluidization modes and various times, and the coefficient of determination ($R^2$) is calculated. $R^2$ values are determined at all 21 sampling locations, and the minimum values (worst cases) are presented in Table 2.1. The smallest value of $R^2$ for all sampling locations, all defluidization modes, and all defluidization times is 0.982, which indicates that variation of density with depth is small within the measured depth range of $\approx 80\,\text{mm}$.

**Density variation across the bed.** Having shown that density variation with depth is small, we now examine spatial variation across the bed. To quantify spatial variation, spatially averaged values and standard deviations (SD) of the slope of the cone index curve ($G$), density ($\rho_p$), and relative density ($D_r$) are listed in Table 2.1. The coefficients of variation of density ($COV_{\rho_p}$) and relative density ($COV_{D_r}$) are also provided, where $COV_X = SD_X/\overline{X}$ for variable $X$. $COV_{D_r}$ values are less than 13% except for beds prepared by $DO$ at intermediate $\overline{D_r}$. Beds prepared by $DO$ with short $T$ exhibit the smallest $\overline{D_r}$ where they also show small $COV_{D_r}$. $DFV$ mode prepared beds have $0.3 \leq \overline{D_r} \leq 0.7$ with a small variation of density. For sand beds with $\overline{D_r} > 0.7$, the variation of density is slight when $DCV$ is applied.

Table 2.1. Uniformity of sand samples prepared with three defluidization modes and various defluidization times.

| Mode | Defluidization time, T[s] | Uniformity in depth | Uniformity across breadth | | | | |
|---|---|---|---|---|---|---|---|
| | | $R^2_{\min}$ | Slope of cone index curve, $\overline{G} \pm$ SD[kN/m$^3$] | Density, $\overline{\rho_p} \pm$ SD [kg/m$^3$] | COV$_{\rho_p}$ [%] | Relatively density, $\overline{D_r} \pm$ SD | COV$_{D_r}$ [%] |
| DO | 52 | 0.987 | 551±28 | 1499.72±5.70 | 0.38 | 0.20±0.02 | 11.4 |
| | 1500 | 0.984 | 707±105 | 1526.28±16.93 | 1.11 | 0.30±0.07 | 21.6 |
| | 5000 | 0.989 | 957±166 | 1559.23±20.06 | 1.29 | 0.43±0.07 | 17.4 |
| | 10400 | 0.991 | 1346±299 | 1596.03±24.69 | 1.55 | 0.56±0.09 | 15.5 |
| | 21600 | 0.992 | 1498±346 | 1607.67±25.40 | 1.58 | 0.60±0.09 | 14.7 |
| | 43200 | 0.993 | 1832±409 | 1630.10±24.85 | 1.52 | 0.68±0.08 | 12.4 |
| DFV | 52 | 0.991 | 798±68 | 1540.42±9.65 | 0.63 | 0.36±0.04 | 10.2 |
| | 520 | 0.982 | 960±121 | 1560.44±14.06 | 0.90 | 0.43±0.05 | 12.0 |
| | 5000 | 0.993 | 1286±157 | 1592.83±13.35 | 0.84 | 0.55±0.05 | 8.58 |
| | 10400 | 0.993 | 1596±162 | 1616.97±11.30 | 0.70 | 0.64±0.04 | 6.13 |
| DCV | 50 | 0.992 | 928±118 | 1556.67±14.48 | 0.93 | 0.42±0.05 | 12.9 |
| | 350 | 0.992 | 1415±227 | 1602.82±17.86 | 1.11 | 0.59±0.06 | 10.7 |
| | 1150 | 0.995 | 2259±479 | 1653.32±25.14 | 1.52 | 0.76±0.08 | 11.0 |
| | 3000 | 0.998 | 3143±581 | 1690.57±21.26 | 1.26 | 0.88±0.07 | 7.67 |
| | 5050 | 0.997 | 3567±684 | 1704.31±22.96 | 1.35 | 0.92±0.07 | 7.82 |

The data in Table 2.1 show that density variations across sand beds prepared by fluidization are relatively small. However, there is some spatial correlation in density variations as shown in Figs. 2.9-2.11 for beds prepared with various defluidization times using *DO*, *DFV*, and *DCV*, respectively. These contours are obtained by spline interpolation (MATLAB function `interp2`) of the densities at the 21 sampled locations.

For *DO* (Figure 2.9), the highest density of sand appears in two isolated zones located on opposite sides of the shorter bed midline. From these two peak zones, the density of sand decreases approximately radially. The lowest density is generally found in an area on the left side of the bed (as presented in the figure). Additionally, the density variation in the bed is not symmetric, which might be caused by the momentum of the air exiting the duct. Under this operating mode, the spatial uniformity of the sand bed can be improved by more uniformly distributing the air across the granular bed. For homogenizing the air

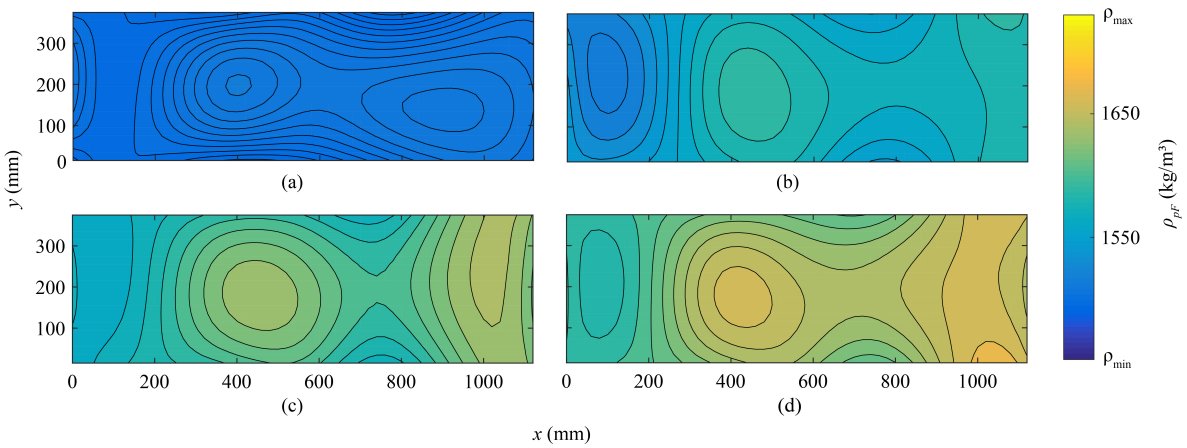


Figure 2.9. Density distribution across sand beds prepared by *DO* with defluidization times $T$ of (a) 52 s ($\boldsymbol{COV_{\rho_p} = 0.38\%}$); (b) 5000 s ($\boldsymbol{COV_{\rho_p} = 1.29\%}$); (c) 10400 s ($\boldsymbol{COV_{\rho_p} = 1.55\%}$); and (d) 43200 s ($\boldsymbol{COV_{\rho_p} = 1.52\%}$).

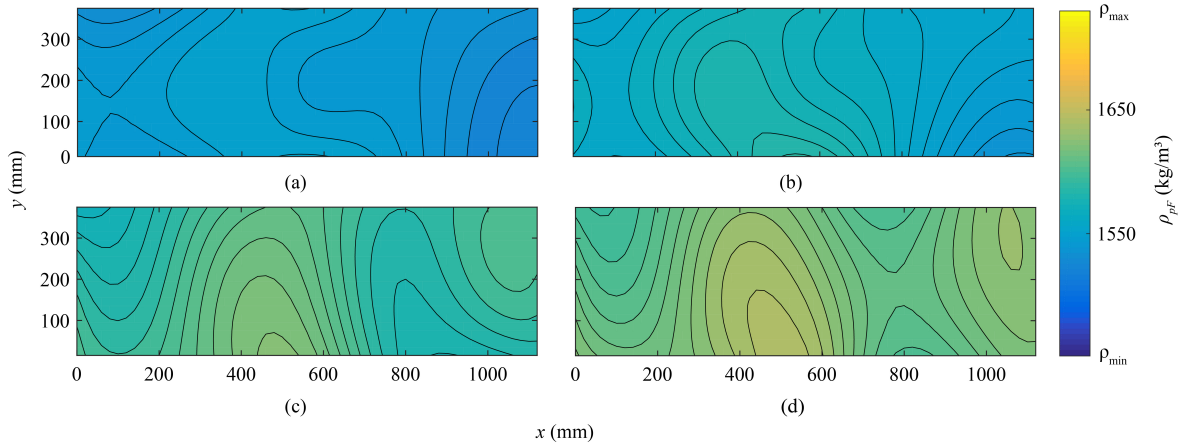


Figure 2.10. Density distribution across sand beds prepared by *DFV* with defluidization times $T$ of (a) 52 s ($\boldsymbol{COV_{\rho_p} = 0.63\%}$); (b) 520 s ($\boldsymbol{COV_{\rho_p} = 0.90\%}$); (c) 5000 s ($\boldsymbol{COV_{\rho_p} = 0.84\%}$); and (d) 10400 s ($\boldsymbol{COV_{\rho_p} = 0.70\%}$).

distribution, the fluidized bed described in this paper can be refined in three ways: (1) increase the height of the plenum and the diameter of the plenum duct inlet to make air distribute more uniformly beneath the distributor; (2) increase the length of the vertical duct segment connecting to the plenum to reduce the asymmetric density distribution caused by

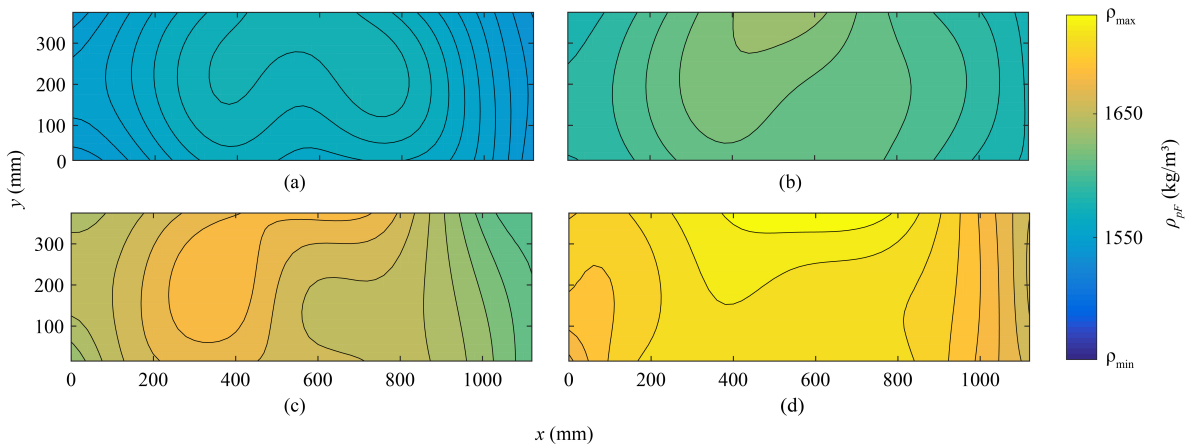


Figure 2.11. Density distribution across sand beds prepared by *DCV* with defluidization times $T$ of (a) 50 s ($\boldsymbol{COV_{\rho_p} = 0.93\%}$); (b) 350 s ($\boldsymbol{COV_{\rho_p} = 1.11\%}$); (c) 1150 s ($\boldsymbol{COV_{\rho_p} = 1.52\%}$); and (d) 5050 s ($\boldsymbol{COV_{\rho_p} = 1.35\%}$).

the momentum of the air flowing from the duct; (3) use a distributor with higher resistance to reduce flow variation by creating a higher pressure drop, which can be realized by either increasing the thickness or reducing the pore size of the distributor.

For *DFV* (Figure 2.10), relatively high density is observed to the left of the bed center, and the density mostly decreases gradually towards the left and right. Overall, the density on the left side of the bed is higher than on the right side. Additionally, the density of sand is higher toward the near side of the bed (smaller $y$ coordinates). For *DCV* (Figure 2.11), the density distribution of sand is similar to that of *DFV*. The density is high at the center of the bed and decreases gradually towards the left and right. Note that the density is higher on the far side of the bed (larger $y$ coordinates) which is the reverse of the case for *DFV*. This variation likely results from the position of the vibration source at one side of the middle of the fluidized bed's frame (see Figure 2.1). Compared to the result of *DO*, it is observed that vibration has a significant influence on the densification of a sand bed. By varying the attachment position(s) of the vibrator(s), one can obtain different density distributions of

the bed. Hence, more vibrators can be added to the bed with a rational arrangement to reconstitute the sand bed more uniformly.

### 2.2.4. Equivalence of beds prepared by fluidization and pluviation

To show that pluviated beds and beds prepared by fluidization are equivalent, Figure 2.12 compares the dependence of the penetration-based density $\rho_p$ in beds prepared by fluidization to those prepared with pluviation as a function of the slope of the cone index curve $G$. $\rho_p$ and $G$ are averages of measurements performed at the 21 sample locations and are given in Table 2.1. The horizontal error bars represent the standard derivation of $G$ at the different average densities, and the vertical error bars represent the standard derivation of $\rho_p$ at various $\overline{G}$. Error bars illustrate the variations of the corresponding quantities. Gray data points are from samples prepared by pluviation, and each data point represents the result from one test. The figure indicates that the density variations and $G$ for beds prepared by fluidization are within the range of the results from the widely used pluviation method, suggesting that fluidized beds are capable of reconstituting sand beds for physical modeling tests in shallow-subsurface geotechnics and terramechanics.

## 2.3. Facilities for model tests

### 2.3.1. Introduction

The sophistication level of model test apparatus, especially the actuating system, depends on the complexity of the mechanical processes one intends to model. Accordingly, as we expand the applications of geotechnical model tests from conventional problems (e.g., foundation bearing capacity) to the interface between geotechnical, mechanical and robotics engineering (e.g., the design of soils excavation equipment [**29**], the soil-wheel interactions and its

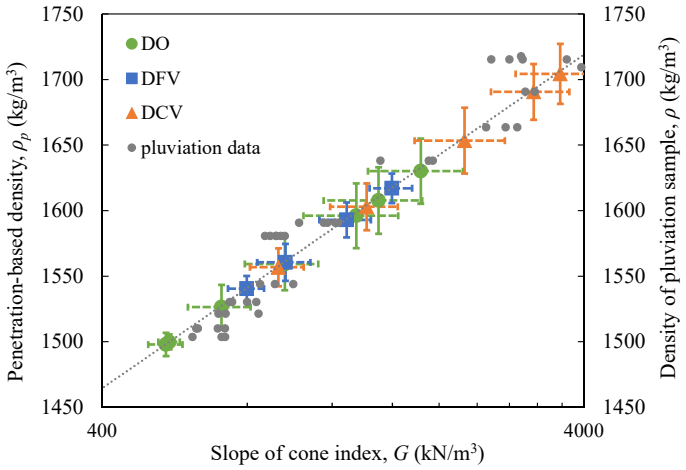


Figure 2.12. Bed density vs. cone index curve slope across sand beds prepared by fluidization (colored symbols) and pluviation (gray circles) indicates equivalence of the two bed reconstitution techniques (see text).

influences on the mobility of off-road vehicles [**100, 101, 102, 103**], and the locomotions of legged and wheeled robots on earth and other planets [**104, 72**]), advanced actuating systems capable of devising multi-planar loading and multiple degree-of-freedom motions are important.

Here a new concept of employing industrial robots as actuating apparatus for small-scale geotechnical tests is presented. This new approach offers three remarkable benefits. First, the robot can move attached objects virtually along any arbitrary trajectory with industrial-grade precision. This feature, augmented by an integrated force sensor capable of simultaneously measuring multi-components of forces and moments, makes the robot an ideal platform for modeling various types of interaction problems. Second, the robot is fully programmable in that all operations can be prescribed and executed automatically and repeated. Lastly, industrial robots, like any other industrial product, is manufactured by standardized processes with quality control, thus their performance is reliable and predictable. Once the robots are verified to be suitable for geotechnical model tests, the same

approach can be rapidly adopted in laboratories across the world. Accordingly, the goal of this work is to answer whether such an idea is viable.

### 2.3.2. Robot performance evaluation

Figure 2.13(a) shows the general arrangement of the robot-based laboratory. The robot is an IRB-4400 six-axis (or six-degree-of-freedom) robot manufactured by ABB, which is mounted to the ground floor. These six axes are depicted in Figure 2.13(b) and their corresponding motion types are briefly summarized here. Axis 1 allows the horizontal rotation of the entire robot against its base. Axis 2 controls the forward and backward extension of the lower arm, while Axis 3 extends the robot's vertical reach by raising and lowering the upper arm. Axis 4, also known as wrist roll, rotates the upper arm along its longitudinal axis. Axis 5 raises or lowers the wrist of the robotic arm, while Axis 6 is responsible for the twisting of the wrist (i.e., circular motion around the $X$-axis shown in Figure 2.13(b)). For detailed discussions on the kinematics of such articulated robot, the readers are referred to literature on modern robotics (e.g., [**105, 106**]). Any object used to model structures or machine parts (e.g., the blade shown in Figure 2.13(a)) is attached to the tip of the articulated arm, hereafter referred to as the tool center point (abbreviated TCP as shown in Figure 2.13(b)). Accordingly, interaction processes between the objects and soils can be modeled by either explicitly prescribing the trajectories of the TCP (i.e., displacement control) or implicitly controlling the TCP positions to match desired reactive forces/moments (i.e., force control). As displacement control is exclusively used, the discussion of force control is excluded. The selected robot offers three basic modes to define the TCP trajectories: (1) axis-by-axis, where the rotation angles associated with the six joints are explicitly defined; (2) linear motion, where trajectories are straight lines in space; and (3) reorientation, which changes the object's

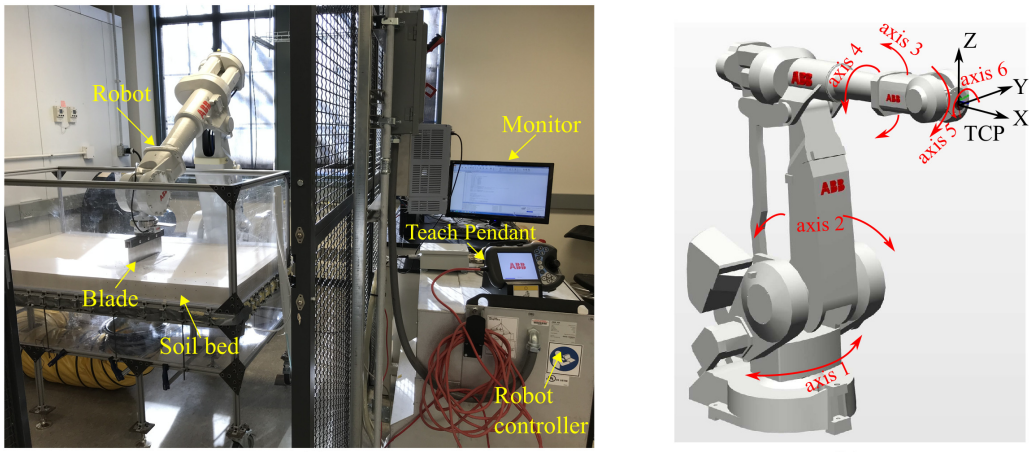


Figure 2.13. Robot-based model test laboratory: (a) picture showing the main components of the testing facility, including the ABB six-axis industrial robot, its control system, a soil bed, and an object that interacts with soils; (b) cartesian coordinate associated with the tool center point (TCP) and the six independent joints that controls the motion of the TCP.

orientation while fixing the TCP position. These modes can be combined together to achieve complex motion control of the object.

**2.3.2.1. Precision of motion control.** The robot uses the rotary encoders associated with the six axes to track the position of the TCP (also the position of attached objects). This quantity hereafter is referred to as "internal position". There can be a difference between the internal position and the actual TCP position due to mounting tolerances, deflection in the robot structure, and various other factors. To quantify the difference, an external independent measurement of the TCP position is introducted by using a linear potentiometer displacement transducer (LPDT) manufactured by GDS instruments. The LPDT is connected to the TCP and fixed planes to measure the TCP displacement when robot moves toward to the planes. The evaluation is repeated in multiple positions within the robot's working range to consider the influences of varying the spatial configuration of the robot arm on the measurement error of the TCP position. A dead weight of around

200 N is attached to the TCP to model estimated maximum external forces exerted in typical tests. Among all cases considered, the external force produces 0.35 mm TCP movement that cannot be detected by the robot measurement. Except this measurement error resulting from the elastic compliance of the robot structure, the difference between the displacements measured by the LPDT and the robot is less than 0.25% of the total displacement (i.e., 35 mm, available movement range of the LPDT). While this relative error is not expected to grow with increasing displacement, further confirmation over a wider range of displacements would require the use of instruments capable of providing sufficient accuracy over such a range.

**2.3.2.2. Resolution and accuracy of force measurement.** A load sensor (Sunrise Instruments, #3314C) is installed at the tip of the robotic arm, which measures forces in 3 mutually perpendicular axes ($F_x, F_y, F_z$) and 3 torques about the same axes ($T_x, T_y, T_z$). The capacity of force sensor varies in these components: 660 N for $F_x$ and $F_y$, 1980 N for $F_z$, 60 N·m for three torques $T_x$, $T_y$, and $T_z$. The force sensor is evaluated in terms of the resolution and measurement accuracy.

The resolution of a force sensor refers to the smallest forces/torques that the system can reliably make, which is essentially a measurement of noise in the output. It is detected to be 0.11 N for $F_x$ and $F_y$, 0.36 N for $F_z$, and 0.011 N·m for $T_x, T_y, T_z$. The accuracy of this sensor is assessed by applying known dead weight to the tip of a rigid bar connected to the load cell and rotating the robot Axis 6 (see Figure 2.13(b)) to align the force and moment generated by the dead weight with the load sensor's different axes. For force and moment up to 200 N and 20 N·m (both reflect the expected maximum force and moment in typical tests), the relative measurement error is less than 4%. The errors between measured and actual values might arise from the cross-talk of the sensor. Specifically, when a specified force (or torque)

applied to the object is to be measured using a strain gauge, other forces (or torques) acting on that object affect the sensor output as well. The cross-talk is the undesirable sensor response to such loads, which is a common problem for a multi-axis sensor.

**2.3.2.3. Stiffness of the robot.** The stiffness of robot structure was evaluated by measuring the displacement of TCP under a static load of 455 N. The measurement was conducted in the condition that the robot arm was inactive to exclude the displacement caused by the robot's controller. When the force was applied in the $Y$-direction, the displacement of the TCP along the $Y$- and $Z$-axis were 1 mm and 0.6 mm, respectively. When the force is loaded in the $Z$-direction, the displacement along the $Z$- and $X$-axis are 0.2 mm and 0.6 mm, respectively. Since these measurements may change if the position of the arm is changed, the results are served for reference purpose of the evaluation on the robot stiffness. It should also be noted that the displacement of the TCP can be detected and recorded by the data acquisition system (i.e., internal position) when it is larger than 0.5 mm without programming the movement of robot. In other words, the overall error in the displacement measurement due to the stiffness of root structure is less than 0.5 mm.

### 2.3.3. Benchmark test: strip footing under combined loading

The behavior of a strip foundation under general planar loading is a conventional geotechnical topic that has been thoroughly studied by small-scale tests [**107, 108, 109, 110, 111**]. This test is replicated to benchmark the performance of the robot, specifically by identifying a failure envelope for a strip foundation under combined loads.

**2.3.3.1. Experimental setup.** All tests are performed on dry silica sand, of which basic properties is provided in Section 2.2.2. By using the pluviation method described by [**62**], sand specimens were prepared with a dry density of 1.70 g/cm$^3$ (i.e., a relative density of $D_r$

$= 90\%$), and their friction angles range from $47.6^\circ$ to $32.7^\circ$ corresponding to the normal stress varying from 20 kPa to 110 kPa. The friction angles were measured by performing direct shear tests. In each test, the confining pressure kept constant, while a horizontal force was applied to the bottom part of the shear box at a constant speed, producing a gradual displacement. The resistance of the soil to this movement was measured and reflected the strength of the soil to shearing, i.e., the shear strength. Shearing was continued until shear stress reached its maximum value. The friction angle corresponding to each confining pressure was calculated based on the measured peak shear strength.

Previous studies generally employed the apparatus with sophisticated customized design of loading frame, hydraulic jacks, motors and measurement system to achieve different load combinations. In this study, as shown in Figure 2.14, the model foundation is connected to the robot and moved with it along various trajectories, simply achieving any desired loading path. More specifically, the foundation is modeled by a mild steel block with width ($B$) of 20 mm and length ($L$) of 160 mm. This aspect ratio $L/B = 8$ ensures that the deformation of soil beneath the foundation can be approximated as plane strain. The connector shown in Figure 2.14(a) was machined to connect the foundation to load cell rigidly, making the forces acting on the foundation identical to the forces measured by the force sensor.

Figure 2.14(b) shows the trajectories of the model foundation. In this study, straight-line motion was assumed for simplicity, with direction specified by the angle $\theta$. These inclination angles are selected by trial and errors, with the aim of making forces at failure be able to distribute uniformly on the envelope. Speed was kept at 0.02 mm/s to eliminate inertia effects.

**2.3.3.2. Analysis of the test result.** Figures 2.15(a)-(b) show the evolution of the vertical ($V$) and horizontal ($H$) forces for varying values of $\theta$. In all cases, the measured moments were

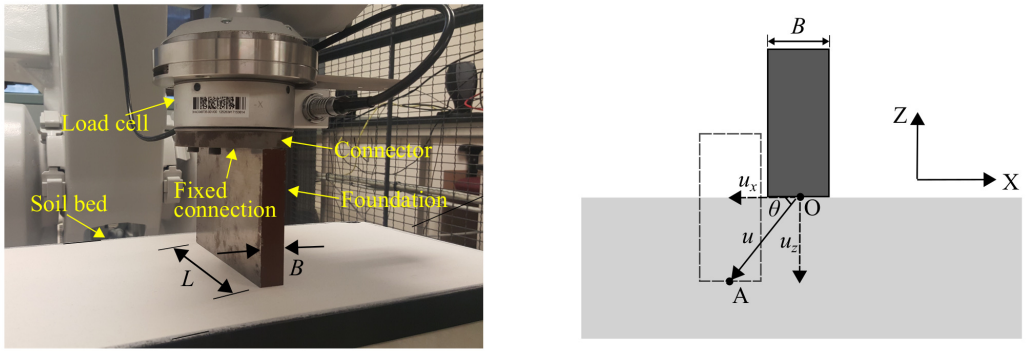


Figure 2.14. Experimental setup and procedures for evaluating the failure envelope of a strip footing under combined loads: (a) dimensions of the model foundation; (b) moving trajectory of the model foundation.

negligible. The force-displacement curves are characterized by post-peak softening typical of sand with low confinement and high relative density [**111, 110, 112**]. The softening in $H$ develops to a reversal of direction for $\theta = 76°$, and $63°$. These negative values can be explained by the nature of the failure mode for penetration-dominant motions, where motion of soil at the base of the foundation reverses the direction of relative sliding. However, in previous studies, most experiments were terminated at the peak, and the softening in $H$ was hardly investigated and reported. To fully understand the phenomenon, the experiments that measure particle motions (such as particle image velocimetry) are needed, which are considered as future work. Besides, it is observed that when the foundation moves vertically, there is small but noticeable horizontal resistance recorded (i.e., $\theta = 90°$ in Figure 2.15(b)). This response is likely to be caused by the slightly uneven soil surface created by the sample preparation process, which generates geometric non-symmetry with respect to the center line of the strip footing.

The combination of forces and moments leading to the failure can be represented by an envelope [**113, 114, 115, 108**]. In Figure 2.15(c), such an envelope bounding the different load paths is plotted. The envelope proposed by [**107**], which has been extensively verified in the literature (e.g., [**116, 117, 118, 119**]), is adopted:

$$H = \beta_1 V[1 - (V/V_{max})^{\beta_2}] \tag{2.5}$$

where $V_{max}$ is the bearing capacity under vertical load and measured as 165 N; $\beta_1 = \tan(\delta)$; $\delta$ is the friction angle at footing-sand interface; $\beta_2$ is a fitting parameter. By applying least square method to fit the combinations of forces at failure ($V$, $H$) to Equation 2.5, the fitted envelope can be obtained, which is shown as Figure 2.15(c). It is observed that the data can be well fitted by this envelope, showing that the test results are consistent with established knowledge. From the fitting parameter $\beta_1 = 0.578$, one infers $\delta = 30°$. Based on the measurement of $V_{max}$, $N_\gamma$ is calculated as 323. When combined it with the bearing capacity solution given by [**120**] ($N_\gamma$ values for friction angles in increments of 1 degrees and for $\delta/\phi$ of 0, 1/3, 1/2, 2/3 and 1.), this implies an approximation of friction angle $\phi = 46°$ $\delta/\phi = 2/3$. The back-calculation compares favorably with the value of $\phi = 47.6°$ measured from direct shear tests for the lowest normal stress considered.

## 2.4. Summary

This chapter discusses the new lab facilities, consisting of an industrial robot and a sand bed prepared using fluidization, and demonstrates their suitability for conducting physical model tests for problems in soil-machine interaction. It should be noted that in spite of the benchmarking test considering a small-scale testing for a geotechnical problem, it reveals the

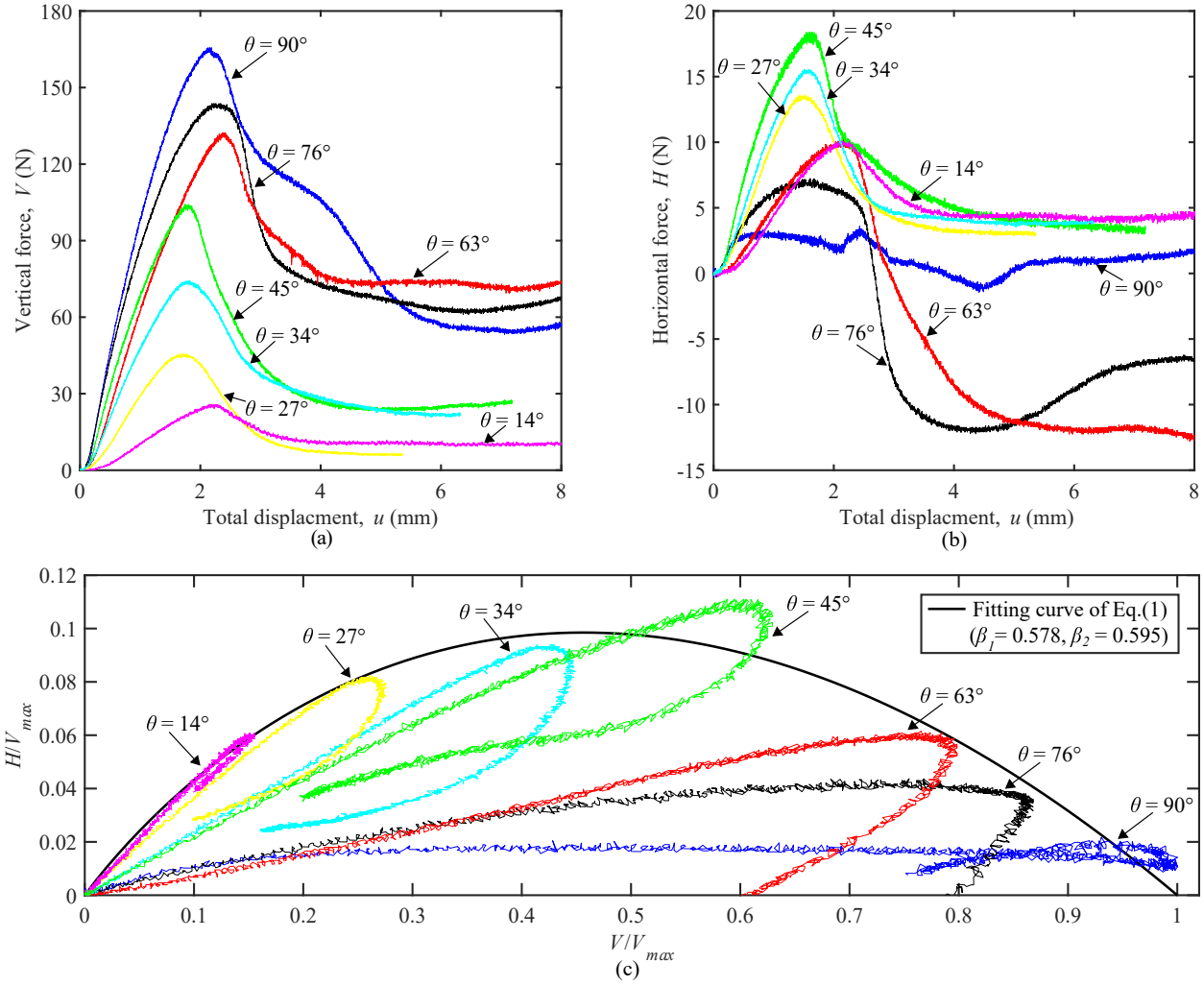


Figure 2.15. (a) Vertical and (b) horizontal force-displacement curves corresponding to the trajectories depicted in Figure 2.14(b); (c) failure envelope for the strip foundation under combined loads.

capability of the test setup for collecting data on a wide range of problems spanning both SMI and geotechnical engineering.

For the fluidized bed used to prepare sand samples, the details of the device and the design methodology are presented, which provides a reference for future applications of this

method. The reconstituted sand beds are characterized, and the performance of the fluidized bed device is evaluated. The main findings are:

(1) Three operating modes are used to prepare sand beds, i.e., defluidization only ($DO$), defluidization followed by vibration ($DFV$), and defluidization concurrent with vibration ($DCV$). Among them, $DCV$ is shown to be the fastest way to prepare dense sand beds of reasonable uniformity.

(2) Sand beds can be prepared with a broad range of relative density (10.4% to 91.7%) from volume-based measurements using the three operating modes and corresponding defluidization times illustrated in this study. The range can be further expanded by extending the bounds of the defluidization times used here.

(3) Sand beds prepared by air fluidization are spatially homogeneous with acceptable variation based on cone penetration measurements. Across the breadth of the bed, the coefficients of variation of relative density are less than 13% for all beds except for some prepared by $DO$. Along the depth, minimum $R^2$ values are close to 1 for all beds prepared by the three modes with different pressure ramp rates, suggesting that their density variations with depth are small.

(4) The fluidized bed is qualified for reconstituting sand beds for physical modeling tests in shallow-subsurface geotechnical engineering. The study demonstrates that fluidized bed is a viable alternative to pluviation, where the latter is the conventional approach. More work is needed to assess whether it can be extended to deeper beds and other materials.

The industrial six-axis robot can move attached objects along any trajectory virtually, which combined with a multi-component force sensor represents a unified platform of modeling various interaction problems. A series of performance evaluations have verified that the robot is capable of tracking objects' movements and measuring resistive forces with the

accuracy required for typical small-scale tests. A benchmark test has demonstrated the application of the robot for studying conventional geotechnical problems. The test example emphasizes the ease of use for conducting tests involving multi-axial motions, which typically would require complicated system for actuation.

By employing the two lab facilities, automated model tests can be achieved wherein the robot-based actuator is seamlessly integrated with the programmable fluidized sand bed. With the lab's automated functionality, efficient experimental study in SMI is allowed, which unlocks potential for parametric study involving different trajectories and is essential for developing the theoretical models in this study.

CHAPTER 3

# Experimental characterization of deformation and force-displacement histories

## 3.1. Introduction

This study mainly has two categories of tests according to the experimental purposes: tests for observing the evolution of soil deformation in the fundamental SMI process (refers to cutting and penetration) and tests to collect data for constructing semi-analytical models. The former was performed using the particle image velocimetry method, and the outcome is used to inform and validate the theoretical models produced in Chapter 4. The latter includes penetration test, cutting test, swipe test and probe test, which generated the force-displacement histories using the facilities described in Chapter 2. The results provide information about the generalized yield envelopes, hardening law, and flow rule necessary for the semi-analytical models described in Chapter 5 and 6. In this chapter, a detailed description of the carried out experiments, along with a preliminary discussion on the obtained results, are provided.

### 3.1.1. Soil deformation measurement

Strain localization into zones, such as shear banding, is a fundamental phenomenon commonly observed in soils. The localization might appear as single, multiple, or pattern of shear zones [**121**]. The zone of localization can be planar or curved, and both shear and volumetric deformation can occur on it [**122**]. The knowledge of the pattern of shear

zones and distribution of shear and volumetric strain in the zones is vital for understanding the mechanism of soil deformation and developing either theoretical or numerical models [**123, 124, 125, 126, 127**].

In geotechnical engineering, previous experimental studies on strain localization are mainly performed through laboratory soil element tests, such as the triaxial test [**128, 129, 130**], the biaxial test [**131, 132, 133, 134, 135**], and the direct shear tests [**136**]. Strain localization is observed in both dense and loose sand [**129, 135**]. Specifically, it is found that the formation of a shear band in sand is normally preceded by a diffuse, non-homogeneous mode of deformation [**121**]. As the shear band formed, the global volumetric response in dense sand is generally dilative, and that in loose sand is contractive [**121**]. The onset of a shear band always occurs near the peak of stress ratio - at, or slightly before it [**129, 137, 138, 121**]. The thickness and orientation of shear bands, as well as the strain level at which a shear band first forms depend on a number of factors, including the initial state of the material (mean effective stress and void ratio), its grading (grain size, uniformity, etc.), and the geometry of the specimen [**121**].

In practical deformation processes, some research has been performed on the strain localization caused by the interaction between soil and an object, such as soil cutting. Gravish et al. experimentally studied the response of dry spherical glass particles with different initial volume fractions ($\rho_0$) to plate drag [**139, 88**]. The volume fraction is defined as the ratio of the particle volume to the total volume occupied by the packing, which is in the same sense as density. The velocity field measurements indicated that the spatiotemporal evolution of the shear band differs with the $\rho_0$: in the sample with small $\rho_0$, the shear band fluctuates in space and time; as the $\rho_0$ is large, the shear band remains almost stationary and is created and destroyed periodically, resulting in the periodic fluctuation in the force. In this study,

the formation of the shear band is explained by the process of granular shear strengthening or weakening accompanied by local compaction or dilation induced by the plate drag. This explanation needs to be verified with explicit experimental evidence, e.g., spatial distributions of the incremental volumetric and shear deformations in materials. However, to the author's knowledge, such distributions, especially the incremental volumetric strain field, were not evaluated for the samples with different densities in the previous experimental work, which further obstructed the understanding of the soil deformation mechanism in the process.

To visualize deformation in soils, different techniques have been used in various laboratory tests: colored layers and markers [**133**], X-rays [**140, 141, 142**], $\gamma$-rays [**143**], stereophotogrammetry [**144, 121, 145**], electrical capacitance tomography [**146, 147**], and digital image correlation (DIC) or particle image velocimetry (PIV) [**148, 149, 150, 151**]. Among these methods, PIV is an optical non-invasive technique, which is implemented by comparing successive pairs of deforming specimen's digital photographs. The method enables the estimations of the displacements at user-defined discrete positions for each pair of photographs. In addition, the strains (i.e., gradients of the displacements) are generally determined by differentiating the displacement field. In this study, PIV was used to reveal the deformation mechanism in sand during cutting and penetration, which can further inform and validate the theoretical models produced in the following chapter.

### 3.1.2. Experimental loading capacity

In this study, the purpose of measuring the loading capacity is to collect data for developing the semi-analytical model model. The model framework draws inspiration from the generalized failure envelopes used in geotechnical engineering for analyzing soil structures subject to combined loading, which was first introduced by Roscoe & Schofield [**152**]. In previous

studies, this method has been developed based on considerable numerical and experimental works, and the latter is in particular overviewed here.

The experimental loading capacities under combined loading conditions ($V - H - M$) has been studied for a broad range of soil structure types, such as (a) shallow and embedded foundations (e.g. [**153, 47, 154, 155**]); (b) caisson foundations (e.g. [**156, 157, 158**]); (c) rigid piles (e.g. [**159, 160, 161**]). The experimental results provided the information to determine the failure envelope formulation. The specific formulation is developed with respect to each soil structure under the condition of small deformation. However, the plate is supposed to move with large displacement in this study. In one movement, multiple loading scenarios that mimic the different types of soil structure are involved. For example, the plate lying on the soil surface corresponds to the classical shallow foundation problem; as the plate penetrates soil deeper, it transfers to the study of soil-pile interaction. Therefore, experimental work for deriving a generalized failure envelope formulation that can recover the various loading scenarios of a plate is needed.

In general, there are three types of experiments that are commonly conducted to study the loading capacities of soil structure under combined loading, i.e., single swipe test, sequential swipe test, and displacement probe test. In the displacement probe test, a displacement increment in a prescribed direction is applied to the foundation from a zero load state, with the final (steady) load state determining a single point on the failure envelope. Provided that the prescribed displacement magnitude is sufficiently large, a well-defined failure load can be obtained. To find the full failure envelope, a series of these probe tests with varying displacement directions must be completed. However, this approach is relatively inefficient as each test only determines a single point on the failure envelope.

The single swipe test was first introduced by Tan [**162**] to investigate the $V$-$H$ failure envelope of a surface foundation using centrifuge model tests. In the test, the foundation is first pushed vertically to a prescribed embedment, after which the vertical displacement is held constant while the foundation is 'swiped' horizontally. This test was generalized to $V$-$H$-$M$ loading by Martin [**155**], Gottardiet al. [**47**] and Byrne [**54**], among other researchers. A fundamental assumption underpinning this type of test is that the swipe phase results in a load path that tracks closely along with the failure envelope, using analogies with hardening plasticity theory as applied in critical state soil mechanics (e.g., see the discussions in Tan [**162**], Martin [**155**] and Martin & Houlsby [**154**]). One drawback of this test is that the load path may deviate inside (or cut across) the failure envelope and thus underpredict the capacity [**163**]. A sequential swipe test is a multi-swipe test, which applies a more gradual change in direction (in displacement space) by way of a series of discrete swipe stages, compared with the abrupt directional change that occurs in the single swipe test. This type of test first appeared in physical experiments [**155, 54, 154**] under the term 'loop test.' More recently, Taiebat & Carter [**164**] and Shen et al. [**165**] used a similar approach referred to as 'modified swipe test.' It is argued that this method is more accurate and can resolve the potential under-prediction behavior of the single swipe test referred to above. However, the loading paths are complex to operate, and the obtained envelope depends on the specific designed paths, which can result in unstable experimental results. Given the pros and cons of each test presented above, in this study, the loading capacity of the plate is studied through the single swipe test for the sake of simplicity and robustness. Additionally, the displacement probe test is also performed to verify that the load path of the single swipe test can track closely along with the failure envelope.

## 3.2. Characterization of soil deformation in cutting and penetration process

The evolution of soil deformation (kinematics) was measured to inform and validate the theoretical models produced in Chapter 4. The tests were specifically performed in terms of the cutting and penetration process as they are the fundamental actions composing a translational movement.

### 3.2.1. Procedures common to the tests for tracking particle motions

The tests were conducted by using the facilities described in Chapter 2 with the addition of a camera. In each test, a sand bed was first prepared by fluidization. A plate with a length of 300 mm and a thickness of 3 mm was used to model the cutting and penetration process. The tests were quasi-2D (plane strain) given that the plate did not extend the full length (750 mm) of the sand bed, resulting in minor 3D effects at the free edge of the plate and effects of friction between the sand and the wall. However, these effects are expected to be insignificant, and the experimental technique follows well-established procedures [**12, 166**]. To reduce the effect of friction between the plate and the sand bed, a Teflon sheet was stuck to the face of the plate in contact with the wall of the soil bed. During the test, the plate was controlled to move at a rate of 0.1 mm/s. The displacements and forces on the plate in the process were obtained. Tests without sand were completed to measure the frictional force between the plate and the wall, and this was subtracted from the force obtained from the tests in sand to produce the real force-displacement history.

For measuring the soil deformation in the process, the camera was fixed in front of the sand bed and took pictures per 0.1 s as the plate moved in sand. It is noted that 25% of the total sand in bed was dyed by black ink to create sufficient contrast on pictures for

performing PIV analysis. These pictures were loaded in GeoPIV-RG, a free MATLAB-designed image analysis module to calculate the displacement fields of sand particles. Based on the obtained displacements, the incremental maximum shear strain ($\dot{\gamma}_{max}$) fields and incremental volumetric strain ($\dot{\epsilon}_v$) fields were computed, where $\dot{\gamma}_{max} = \sqrt{(\dot{\epsilon}_{xx} - \dot{\epsilon}_{yy})^2/4 + \dot{\epsilon}_{xy}^2}$, $\dot{\epsilon}_v = \dot{\epsilon}_{xx} + \dot{\epsilon}_{yy}$. These strain fields were calculated by using a method developed in this study, which can reduce the magnified errors of strains caused by the noise in displacement field [**167, 168**]. The method is evoked by Element Free Galerkin Method [**169**]. For any point we want to know its strain, a support domain around it is built, and the corresponding local shape function is constructed using the moving least square (MLS) method [**170**], which can remove the noise of displacement. The strain is computed by multiplying the displacement with the values of derivatives of the shape function. The details and validation of the method and are described in Appendix A.

### 3.2.2. Cutting process

The evolution of soil deformation in the cutting process was investigated on sand in both loose and dense states with a relative density of 10% and 85%, respectively. In the tests, a 3 mm thick steel plate first penetrated the sand to a depth of about 27 mm and then moved horizontally for a displacement of 40 mm to cut the soil.

Figure 3.1 shows the normalized force-displacement history of the cutting process in sand. Distinct behaviors are observed as cutting in loose and dense sand. For the case of loose sand, force generally increases with the displacement, but subtle fluctuations are also detected. The growth rate of force is high at first, and then it decreases to reach an approximately constant value. For the case of dense sand, the force oscillates with a large

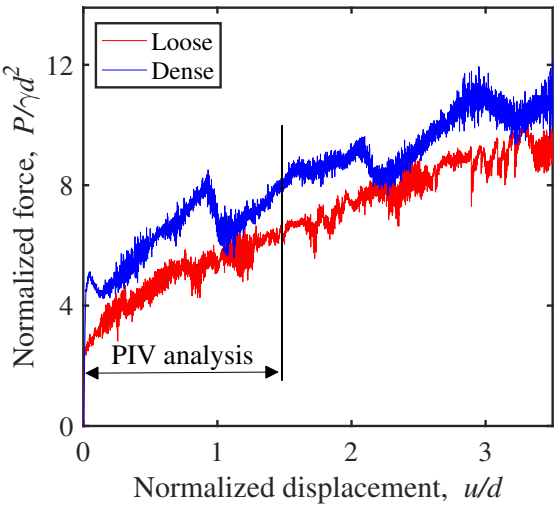


Figure 3.1. Experimental results of cutting in loose and dense sand: normalized force-displacement histories.

amplitude. The troughs of the curve are generally on the force-displacement history of loose sand.

The strain localization of cutting in loose sand has two distinct stages. Figure 3.2 and Figure 3.3 illustrate the typical incremental strain fields in the two stages, which were obtained at the cutting displacements marked in Figure 3.2(a). At the initial stage (A-C), the shear band rapidly advances and retreats, giving an expression of shear band sweeping over a zone. On the shear band, the sand is compacted, implied by the positive incremental volumetric strain (Figure 3.2(c)). After that, the shear band almost remains stationary in one position, while the sweeping appears randomly and temporarily (D-F). In the transition between stationary and sweeping, two shear bands are generally detected (E). It is noted that the incremental volumetric strain is subtle in the full field when the shear band remains in one position, and the compaction is observed in the new shear band developed during the temporary sweeping.

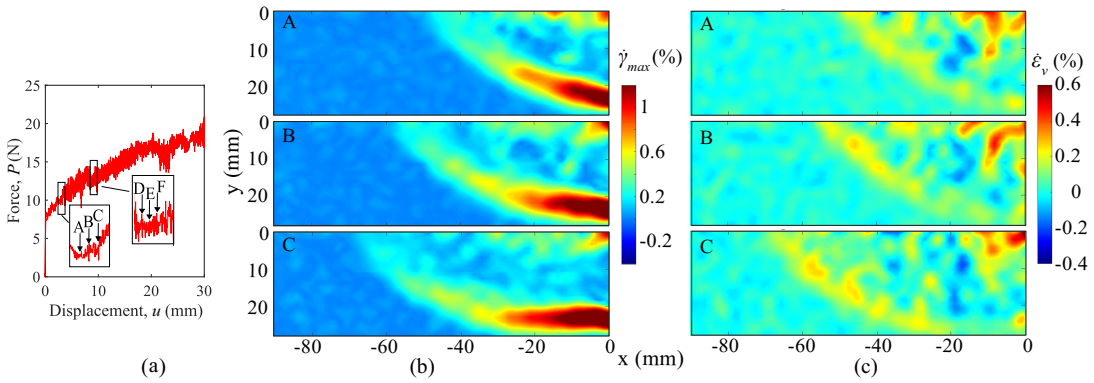


Figure 3.2. Experimental results of cutting in loose sand: (a) force-displacement history of the portion performed PIV analysis; (b) contours of incremental maximum shear strain; (c) incremental volumetric strain (corresponding to $\Delta u = 0.1\,\text{mm}$), where A: $u = 2.7\,\text{mm}$, B: $u = 2.9\,\text{mm}$, C: $u = 3.2\,\text{mm}$.

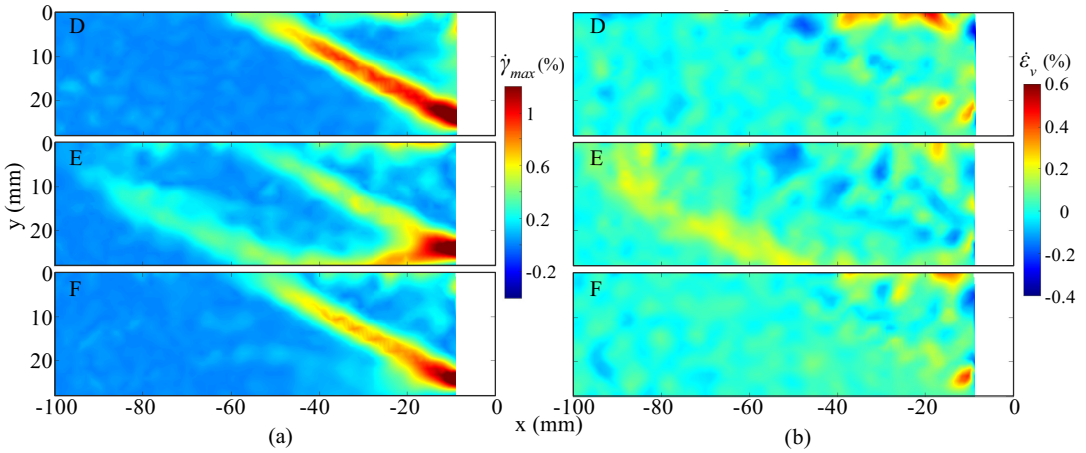


Figure 3.3. Experimental results of cutting in loose sand: contours of (a) incremental shear strain (b) incremental volumetric strain, where D: $u = 9.0\,\text{mm}$, E: $u = 9.2\,\text{mm}$, F: $u = 9.4\,\text{mm}$.

The evolution of strain localization observed in dense sand is different from that in loose sand. The incremental strain fields describing the evolution are presented, which are illustrated in Fig 3.4. It is observed that the position of the shear band remains fixed for long periods of time (a-b) until rapid, repeated fluctuations precede a jump forward to a new

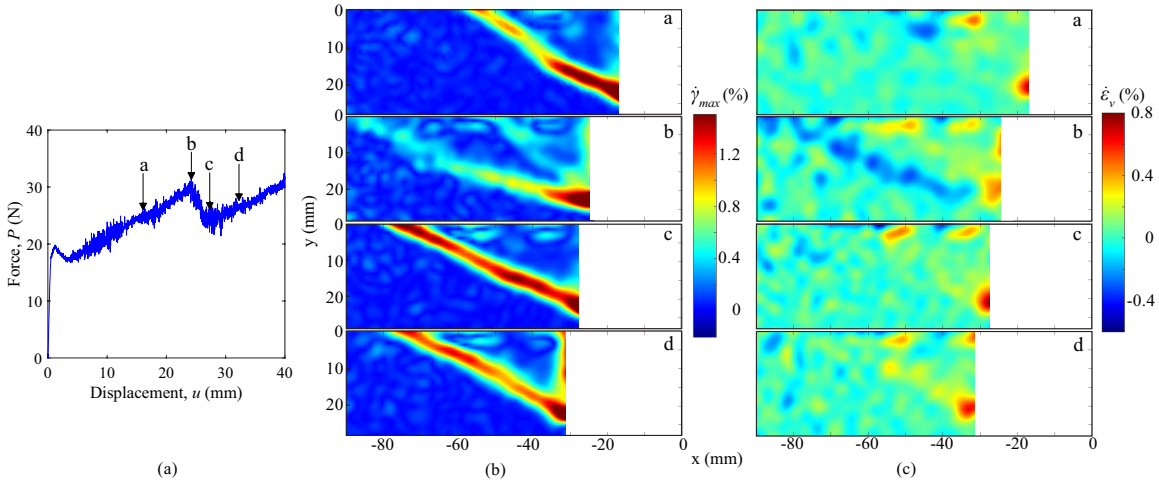


Figure 3.4. Experimental results of cutting in dense sand: (a) force-displacement history of the portion performed PIV analysis; contours of (b) incremental maximum shear strain; (c) incremental volumetric strain (corresponding to $\Delta u = 0.1\,\text{mm}$), where a: $u = 16.1\,\text{mm}$, b: $u = 24.2\,\text{mm}$, c: $u = 27.3\,\text{mm}$, d: $u = 32.4\,\text{mm}$.

location (b-c). During the transition of shear band location, two shear bands are detected simultaneously: one is disappearing while the other is developing. The sand is dilated on the newly forming shear band and compacted on the original shear band, indicated by the negative and positive incremental volumetric strain, respectively.

### 3.2.3. Penetration process

The evolution of soil deformation in the penetration process was investigated only on the sand at the dense state. In this test, the sand bed was prepared with $D_r = 78\%$. A plate with a width ($2B$) of 16 mm was pushed into sand vertically.

Figure 3.5(b) shows the field of incremental maximum shear strain ($\dot{\gamma}_{max}$) at stages corresponding to the points A-F in Figure 3.5(a). From A to B, the first shear localization is formed and extended to the surface at a distance of 2.5 times of plate width. Then it breaks

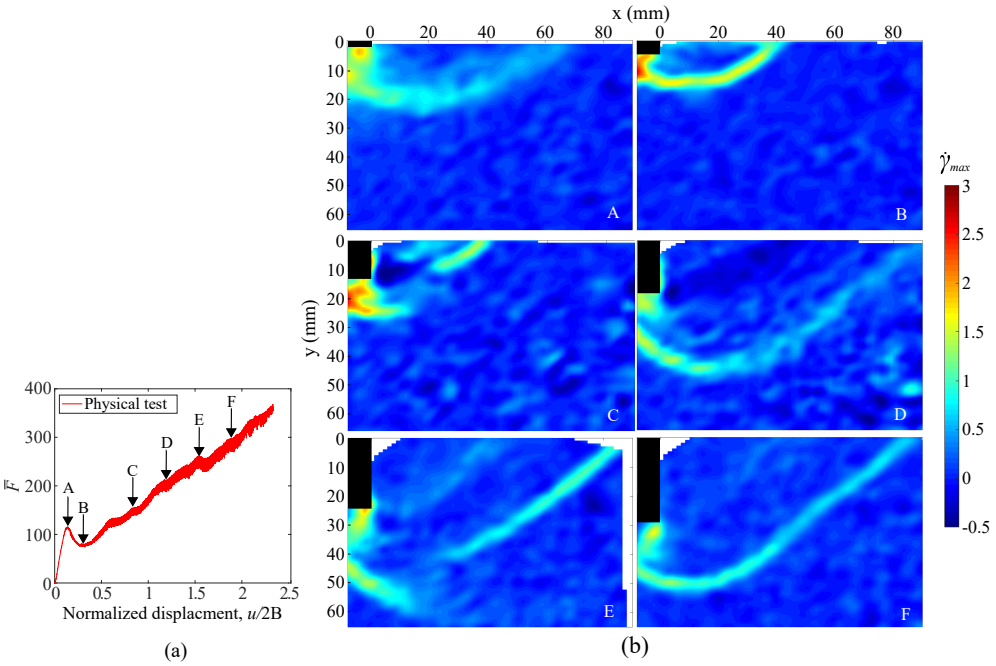


Figure 3.5. Experiments of penetration in sand (a) normalized force-displacement history; (b) contours of incremental shear strain field ($\Delta u$ = 0.1 mm) at six penetration depths corresponding to points A-F in (a).

down and fades away, followed by the development of a new shear localization. This process is repeated as the plate penetrates in soil. Note not every shear localization can be extended to the soil surface, and some of them terminate in the sand.

Figure 3.5(a) illustrates the normalized force-displacement history in the process, where $\overline{F} = F/(0.5\gamma(2B)^2L)$, and $L$ is the length of the plate in the direction normal to the front. A pronounced decrease of force is observed from A to B, resulting from the softening of sand as the shear band develops. From B, the force increases with the depth overall, while some fluctuations appear.

## 3.3. Experimental loading capacity of a vertical plate in sand

The loading capacity of a vertical plate was studied experimentally for developing the semi-analytical model described in Chapter 5. The tests were performed by moving the plate along various trajectories on both loose and dense sand, which are mainly categorized into four types: purely penetration test, horizontal cutting test, swipe test, and probe test. These tests can generate information about the generalized yield envelope, hardening law, and flow rule necessary for a plasticity model.

### 3.3.1. Common procedure

The tests were conducted by using the facilities described in Chapter 3. A steel plate with a length of 300 mm and thickness of 3 mm was attached to the robot arm and moved to an initial point before contacting soil. The forces at the initial point were recorded as the reference forces. Then the plate was moved to the start point, which is at the center of the bed in the horizontal plane. After preparing the sand bed to the desired state, the plate was loaded along one trajectory. During the process, the forces and displacements were recorded. By subtracting the reference forces, the forces corresponding to a specific trajectory of the plate were obtained. The definition of the plate displacements and measured forces for all tests are schematically shown in Figure 3.6, where $u$ is the horizontal displacement, $w$ is vertical displacement, $H$ is horizontal force, and $V$ is vertical force. $H$ is always positive since the soil response is the same when the lateral movement is in either direction, and $V$ is considered as a compression force and recorded by a positive sign when it acts upwards on the plate. It is noted the loose sand bed was prepared to a relative density of 10% by using operation mode 1 with the fluidization time of 40 s, and the dense sand bed was prepared to

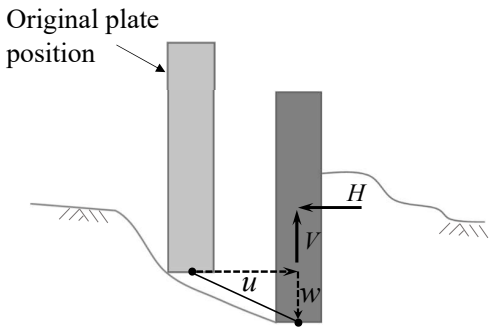


Figure 3.6. Definition of plate displacement and measured reaction forces.

a relative density of 79% by using the operation mode 2 with the fluidization time of 1500 s for all tests in this section.

### 3.3.2. Penetration test

The penetration test involved five vertical loadings. Their purpose is to study the development of loading capacity from the surface to deep penetration depth and get information about the plate's vertical elastic stiffness. In test 1, the plate started to penetrate the sand from its surface at a rate of 0.1 mm/s. The penetration displacement is 70 mm, which is about 23 times the plate thickness. For test 2-5, the plate was first buried at a depth of 15 mm, 30 mm, 45 mm and 60 mm, respectively, and then began to penetrate the sand with a slower rate of 0.05 mm/s. It was tested that the velocity difference (0.05 mm/s and 0.1 mm/s) does not influence the soil response.

Figure 3.7 shows the development of vertical loading capacity with the depth of the plate in dense sand. For test 1, the vertical force generally increases with the depth, while obvious fluctuations are also detected. The fluctuations might result from the periodic but not regular formations of shear band, which was observed in the PIV test presented in Section 3.2.3 (Figure 3.5). The same dynamics of shear bands were also detected in a study

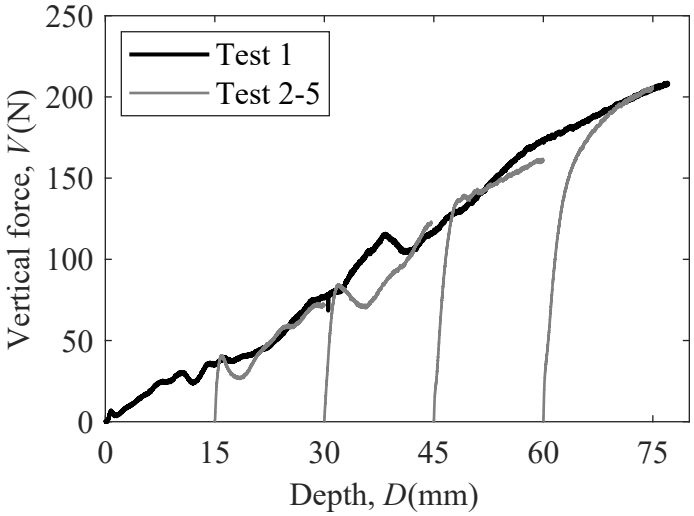


Figure 3.7. Vertical force with the plate depth in dense sand.

on the flow field around a moving finger in granular material [**171**]. For test 2-5, the force rises rapidly to reach the force curve of test 1. Among them, pronounced peaks of force were observed in the tests with plate buried at a depth of 15 mm and 30 mm, accompanied by the appearance of failure surface at the sand surface and bulging of the sheared mass of sand. As the buried depth are 45 mm and 60 mm, the force increase with the depth without sudden failure. The phenomena are consistent with the earlier investigation by Vesic [**111**]: in dense sand, general shear failure occurs at shallower depth while local shear failure or punching shear failure occurs at greater depth. However, the latter two types of failure happen at a much deeper relative depth ($D/B$) in this study than that in previous research [**111**].

Figure 3.8 shows the vertical loading capacity with the depth of the plate in loose sand. The vertical force steadily increases with the penetration depth without obvious fluctuation, which is distinct from the load-displacement behavior in dense sand (Figure 3.7). The inset shows high-frequency oscillations of vertical force in the test, which may result from the

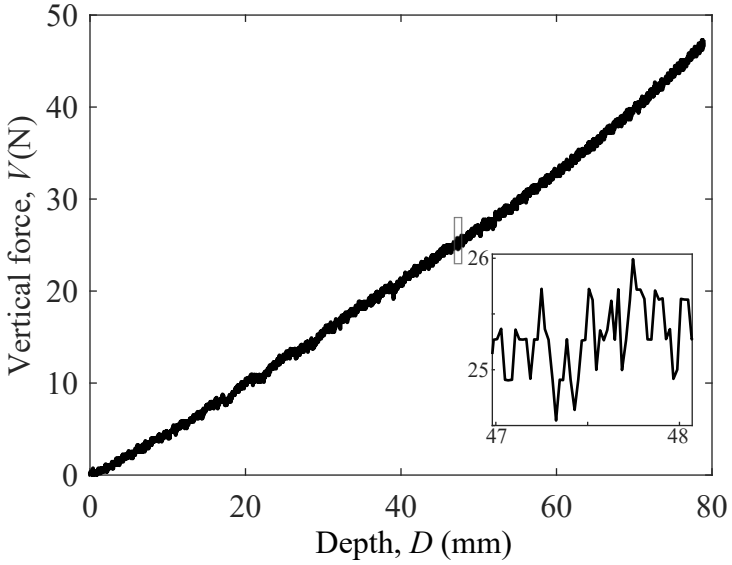


Figure 3.8. Vertical force with the plate depth in loose sand.

sudden movement of a single particle or the rearrangement of a few sand particles in a local neighborhood [**172**].

### 3.3.3. Cutting test

Cutting tests were conducted to investigate the loading capacity in the horizontal loading direction. In a test, the plate first penetrated the sands to a specific depth and then moved laterally at a rate of 0.05 mm/s. The cutting processes were performed at three penetration depths: 15 mm, 30 mm and 45 mm.

The experimental result of cutting tests in dense sand is presented in Figure 3.9. It is observed that the horizontal force generally grows with the displacement but is subjected to fluctuations for all tests performed at different penetration depths. The fluctuations are large relative to the magnitude of the force. The force paths (Figure 3.9(b)) show that vertical

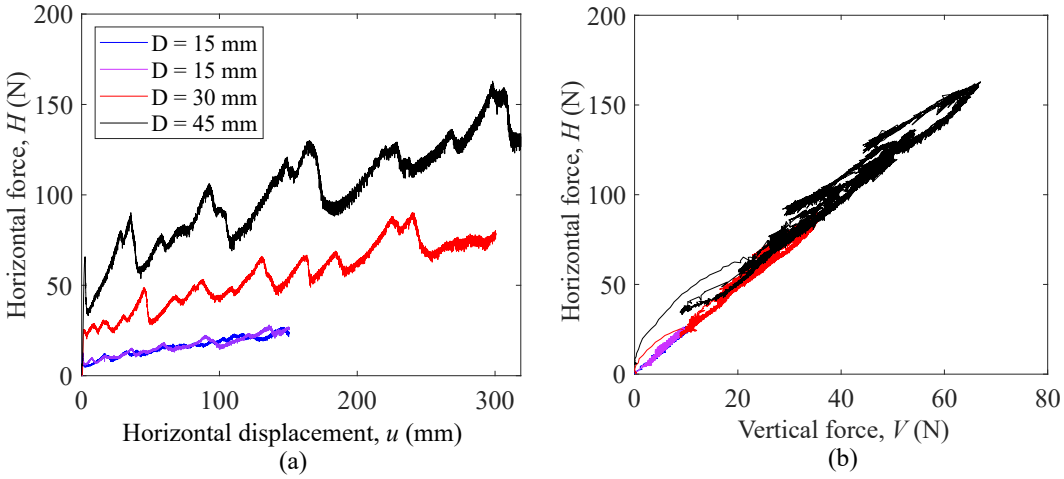


Figure 3.9. Results of horizontal cutting tests in dense sand: (a) horizontal force versus displacement; (b) force paths.

force changes with the horizontal force simultaneously to keep a constant force ratio in the process for all cases.

Distinct behaviors of force-displacement are observed when cutting in loose sand, illustrated in Figure 3.10(a). The horizontal force steadily increases with the displacement, and only subtle fluctuations are detected. The growth rate of force is high at first, and then it decreases to reach an approximately constant value. The force paths of cutting in loose sand (Figure 3.10(b)) is similar to that in dense sand. The vertical forces increase with the horizontal forces linearly, and the force ratios are constant.

### 3.3.4. Swipe test

Swipe tests were performed to evaluate the generalized yield envelope used in the semi-analytical model. The yield envelope is a envelope in the space of forces, and the state of forces inside the envelope is elastic. The original swipe test is proposed by Tan [**162**] as follows. A vertical displacement is applied until a footing reaches a specified penetration depth, and then the footing is driven purely horizontally. A horizontal load clearly develops

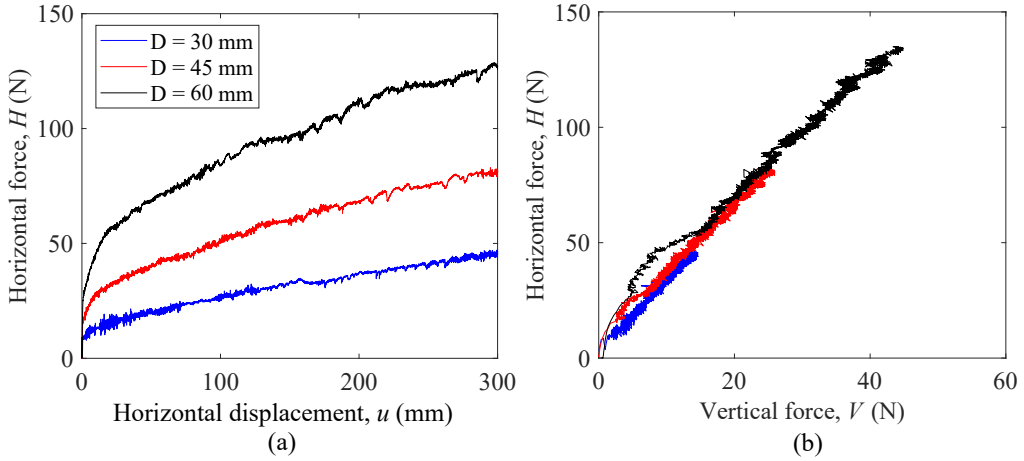


Figure 3.10. Results of horizontal cutting tests in loose sand: (a) horizontal force versus displacement; (b) force paths.

while the vertical load decreases so that the load path sweeps out a track in $V$-$H$-$M$ space. It is argued that this path is approximated closely to a track across the yield surface at the given penetration [**162, 155**]. In this study, the swipe tests were conducted by implementing the above procedure with two modifications. First, the moment $M$ in the process is ignored, and the force path is argued to represents a yield envelope in $V$-$H$ space instead of $V$-$H$-$M$ space. Second, two swipe tests were performed to obtain a complete yield envelope (an example is shown in Figure 3.11). The test labeled 'Swipe test1' was the same as that described above, and the generated force path was the right portion of the surface. The test labeled 'Swipe test2' was designed based on the original swipe test. The plate penetrated the sand with a vertical displacement over the specified penetration depth for 2 mm, followed by pulling the plate to the specified depth to produce vertical load in the opposite direction, and then the plate was driven purely horizontally. The resulting force path constitutes the left portion of the yield envelope. In these tests, the plate was moved at a rate of 0.5 mm/s.

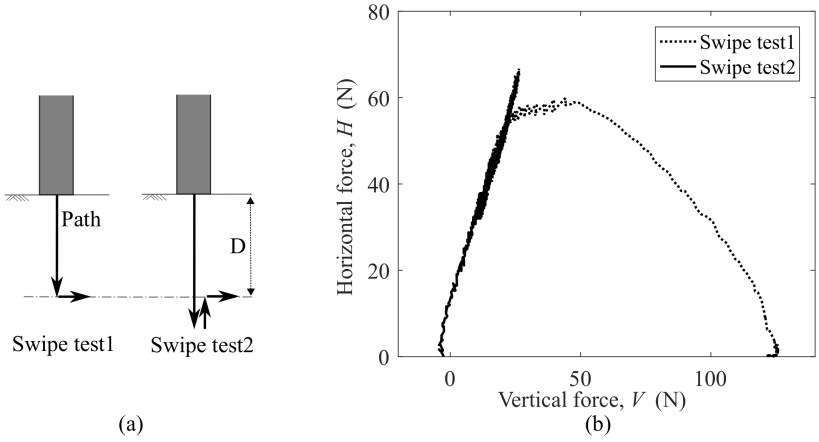


Figure 3.11. (a) Schematic of the loading configuration of swipe tests; (b) an example of a complete yield envelope generated from swipe tests.

Figure 3.12 shows the experimental results of swipe tests, where the envelopes were obtained at the depths of 30 mm, 45 mm and 60 mm in dense sand and were generated at the depths of 45 mm, 60 mm and 75 mm in loose sand. The results indicate that the generalized yield envelope are generally in the shape of a half ellipse. In loose sand, a pair of load paths composing a yield envelope intersect at the peak of an envelope, and the force ratios at the intersections ($H_I/V_I$) are almost the same with values around 4. In dense sand, the right portion of the yield envelope generated from 'Swipe test1' exceeds the envelope's peak. The horizontal force initially increases and then decreases with the decrease of the vertical force. At the intersections of each pair of load paths, the force ratios ($H_I/V_I$) are about 3.2. The observation, $H_I/V_I$ are roughly constant at different depths, is important in developing the semi-analytical model in Chapter 5. Besides, $H$ generally increases with $V$ linearly from the intersection point for both loose and dense sand.

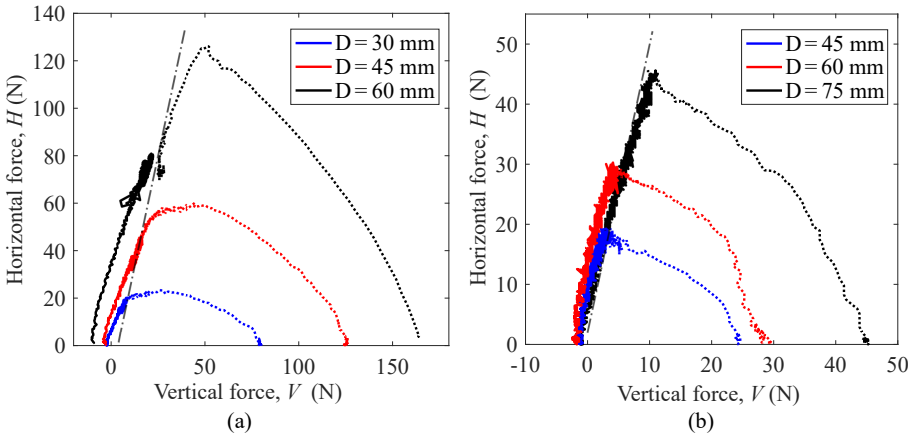


Figure 3.12. Results of swipe tests in (a) dense sand; (b) loose sand.

### 3.3.5. Displacement probe test

As point out in Section 3.1, the displacement probe test can be used to find the yield envelope. However, such a test was rarely conducted experimentally in previous research since a series of tests with varying displacement directions are required to complete one envelope. Therefore, instead of directly obtaining the envelope, the displacement probe test was conducted for two purposes in this study. First, the test is performed to verify that the swipe test's load path can track closely along with the failure envelope, informing the applicability of the swipe test. More importantly, the displacement probe test can explicitly investigate the displacement directions on the failure surface. It provides direct information for deriving the flow rule and plastic potential in the semi-analytical model.

In a displacement probe test, the plate was buried to a specific depth and then driven translationally in a direction by applying vertical and horizontal displacements at a constant ratio. A failure surface was derived by a set of tests, where the plate was moved in various directions at a depth. In this study, three sets of displacement probe tests were performed:

tests at a depth of 45 mm in loose sand, tests at a depth of 60 mm in loose sand, and tests at a depth of 60 mm in dense sand.

Figure 3.13 – 3.15 show the results for the three sets of tests, which are presented by plotting the loading path, the horizontal and vertical force versus the total displacement ($u_t$). The vertical force acting upwards on the plate is considered as a compression force and recorded by a positive sign. The horizontal force is all positive since the soil response is the same when the lateral movement is in either direction. In the figures, the red lines indicate the tests applying a negative vertical displacement ($w$), i.e., the plate is 'pulled out.' In contrast, the black lines show the results of tests performed with a positive vertical displacement. For each line, the marker highlights the failure point, which is determined based on the criterion that the rate of force ($V$ or $H$) reaches a constant value at the point. The results indicate that the plate has a much larger bearing capacity in compression than in tension. The failure envelope is overall in the shape of a half ellipse. The obtained failure points are plotted on the corresponding yield envelope generated by swipe tests (illustrated as Figure 3.16). These points are observed close to the envelopes, which provides some validation on the assumption that the swipe test can track along with the yield envelope. Further analysis of the displacement directions on the failure surface will be conducted in a later chapter.

### 3.4. Experimental loading capacity of an inclined plate

In this section, the experiments were performed to investigate the 'loading capacity' of an inclined plate in sand. This 'loading capacity' is not the same as that strictly defined in soil mechanics but refers to the characteristic soil responses to an inclined plate under different configurations and loading conditions. These characteristic soil responses will be extracted

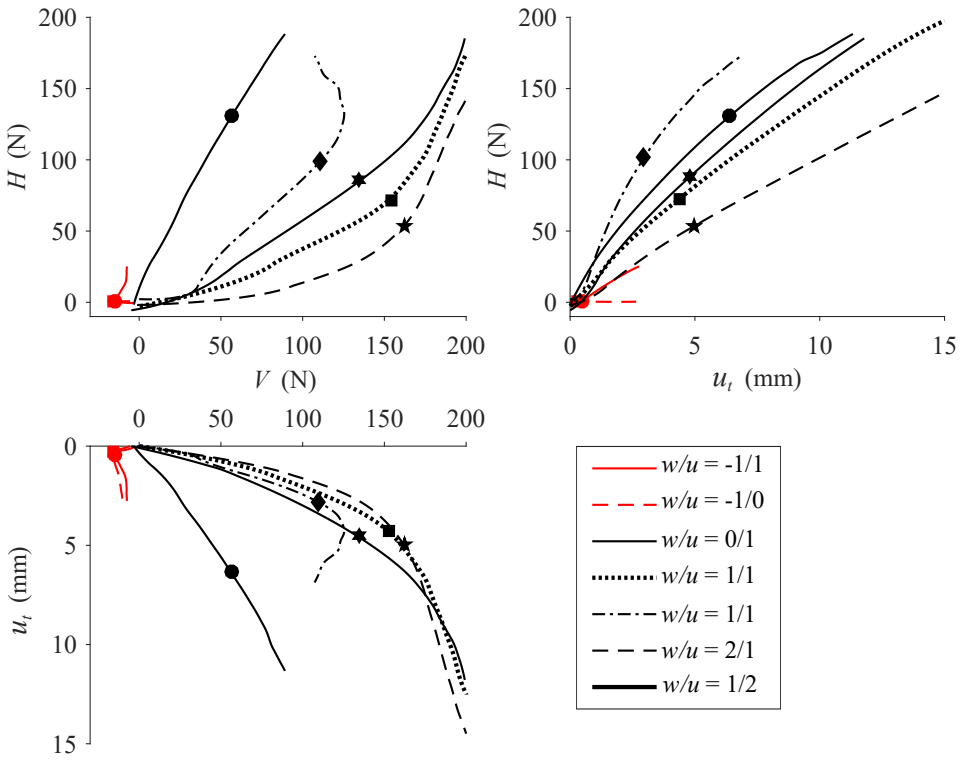


Figure 3.13. Results of probe tests in dense sand at penetration depth of 60 mm.

as features to develop a semi-analytical model (described in Chapter 6) that can predict the force-displacement response of a plate moving with both translational and rotational motions in sand.

### 3.4.1. Experimental design

The experiments are conducted to generate information about the generalized yield envelope, hardening law, and flow rule for constructing a semi-analytical model. As schematically illustrated in Figure 3.17(a), five types of experiments, i.e., penetration, positive swipe (PS), negative swipe (NS), horizontal cutting (HC), and reverse cutting (RC), are designed based on the experimental work for a vertical plate (in Section 3.3). The experiments were performed as a plate was placed at five different inclination angles (the angle between the plate

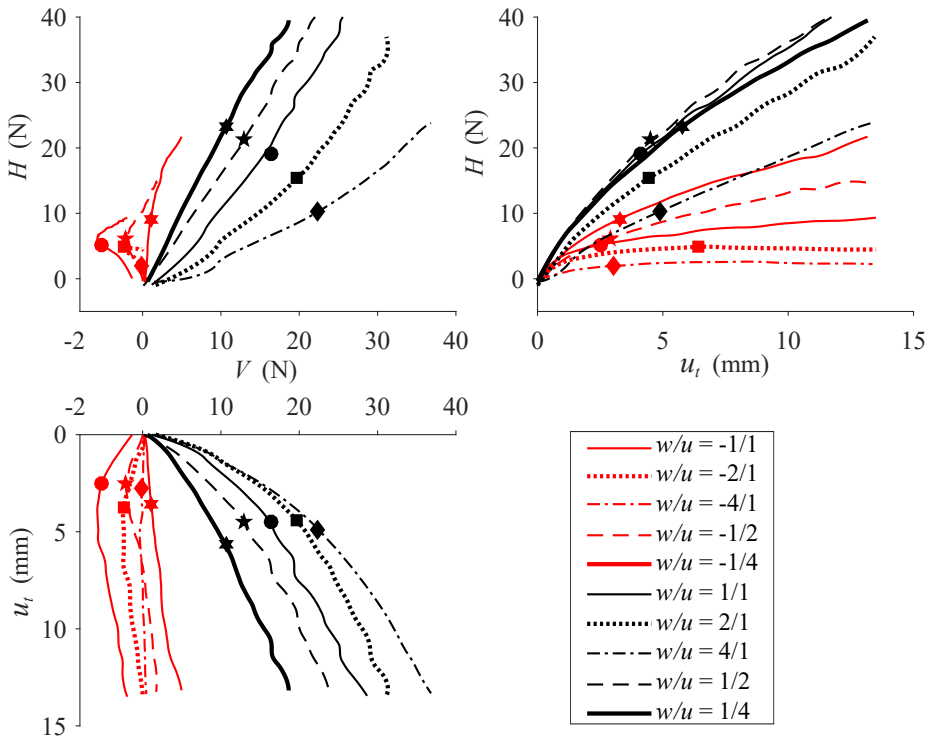


Figure 3.14. Results of probe tests in loose sand at penetration depth of 60 mm.

and the vertical direction): $\alpha = 0°, 15°, 30°, 45°, 60°$. For each test, the plate is rotated to a specified inclination angle $\alpha$ beforehand, and there is no rotation involved during the test.

For the penetration test, the plate penetrated the sand from the soil surface in the direction parallel to the inclined plate. During the process, the inclination angle of the plate and the direct of movement were kept constant. In the other tests, the trajectories of the plates consisted of two paths. The first path was identical for the four types of tests, i.e., penetrating sand to a depth of $D$, while the second path was diverse. For the positive and negative swipe test, the second path was perpendicular to the first path, and its corresponding horizontal displacement was positive and negative, respectively. In terms of the horizontal and reverse cutting test, followed by the first path, the plate moved horizontally with positive and

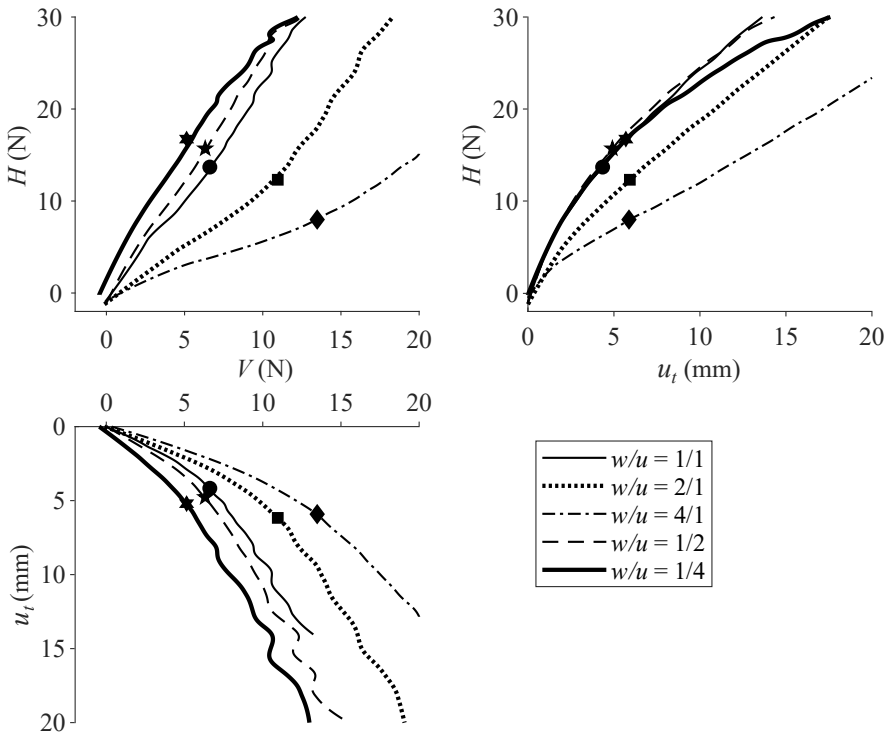


Figure 3.15. Results of probe tests in loose sand at penetration depth of 45 mm.

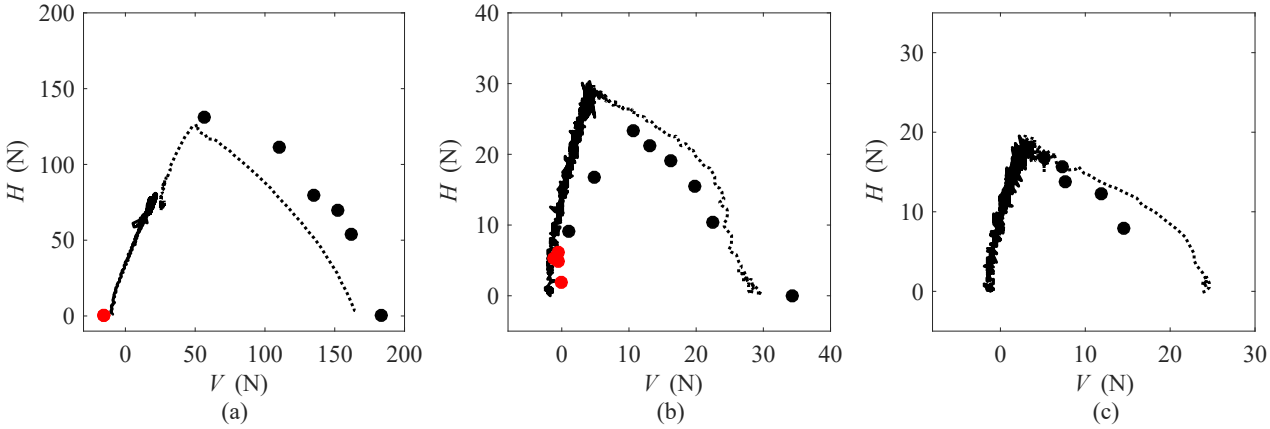


Figure 3.16. Comparison of the results of swipe test and displacement probe tests for the case of (a) $D = 60$ mm in dense sand; (b) $D = 60$ mm in loose sand; (c) $D = 45$ mm in loose sand.

negative displacement, respectively. In this study, the above experiments were performed tentatively, and the obtained results are analyzed for extracting useful information.

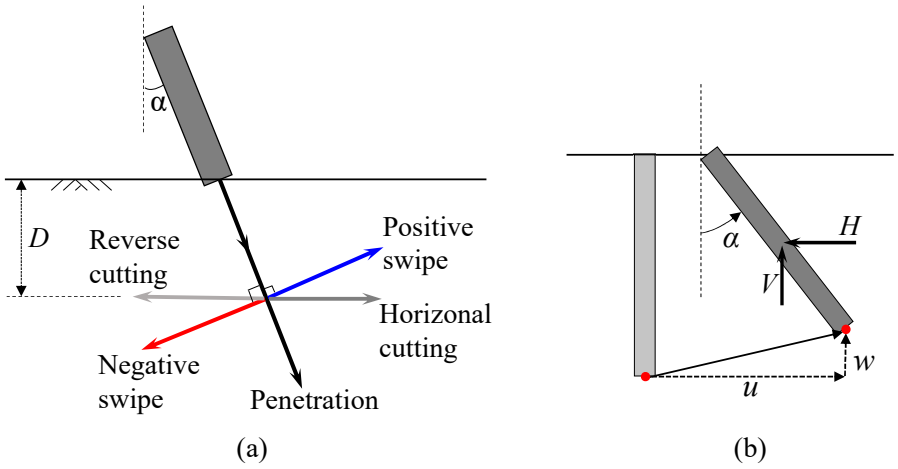


Figure 3.17. (a) Schematic of the experiments performed for an inclined plate; (b) definition of plate displacement and measured reaction forces in tests.

### 3.4.2. Experimental results

**3.4.2.1. Swipe and cutting tests.** Figure 3.18 shows the force paths in the swipe and cutting tests as a plate inclined with different angles, where the vertical force $V$ and horizontal force $H$ are defined in Figure 3.17(b). It is observed that the force path generated in positive swipe tests (blue lines) can generally form a closed envelope with the shape of a half-ellipse. For the positive swipe (blue lines) and positive cutting tests (black lines), the force paths developed before reaching a peak of $H$ are nearly overlapped. After reaching the peak of $H$, the $V$ and $H$ increase in the positive cutting tests, while in the positive swipe tests, $V$ and $H$ generally decrease except for the case of $\alpha = 15°$. Comparing the positive (blue lines) and negative swipe tests (red lines), their force paths are approximately symmetric about $H = 0$ for the plate inclined with a small angle (i.e., $\alpha = 15°, 30°$). However, this symmetry is not observed when the plate's inclination angle is large. In these cases ($\alpha = 45°, 60°$), the force paths of the negative swipe tests develop more irregularly, and the absolute value of

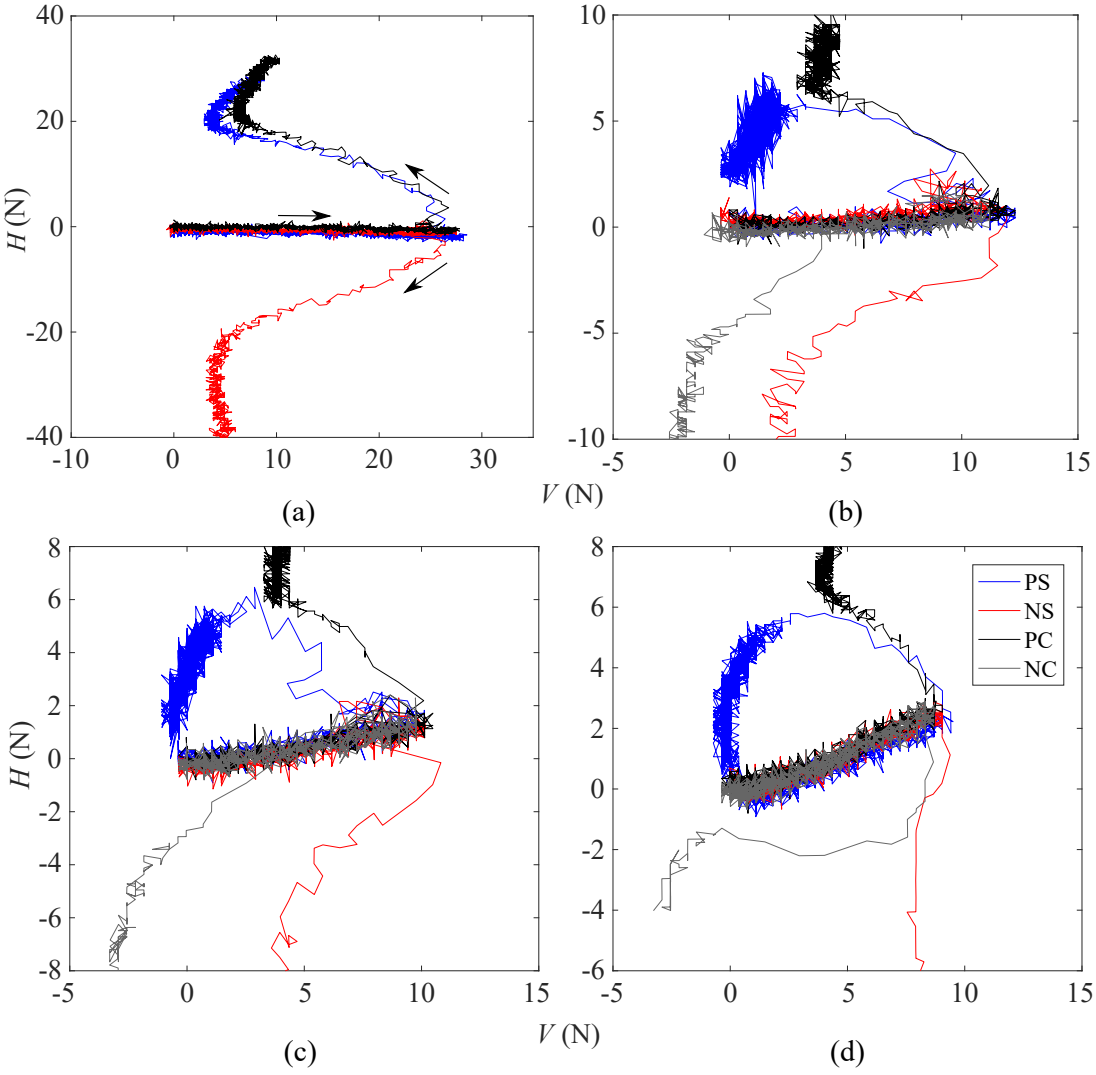


Figure 3.18. Force paths of swipe and cutting tests for a plate with inclination angle of (a) $\alpha = 15°$ ($D = 60\,\text{mm}$); (b) $\alpha = 30°$ ($D = 30\,\text{mm}$); (c) $\alpha = 45°$ ($D = 30\,\text{mm}$); (d) $\alpha = 60°$ ($D = 30\,\text{mm}$).

horizontal force increases much rapidly. Besides, limited information can be obtained from the force paths of negative cutting tests.

The test result obtained from the positive cutting tests at a depth of $D = 30\,\text{mm}$ is illustrated in Figure 3.19, which demonstrates how the horizontal forces develop with the horizontal displacement for a plate inclined at various angles. In the figure, the displacement

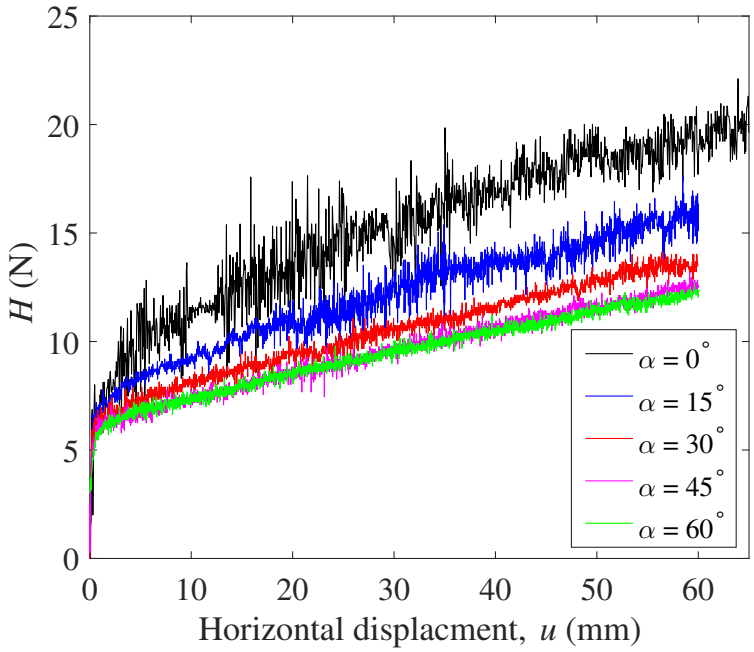


Figure 3.19. Development of horizontal force with horizontal displacement in positive cutting tests.

is measured once the plate penetrated to the depth $D = 30\,\text{mm}$ and started to displace laterally. The result indicates that when $u \approx 0$ (the start of the curve), the horizontal forces on the plate with different $\alpha$ are very close. Then, $H$ rises more slowly for the plate inclined at a larger $\alpha$, resulting in the observation that the horizontal force generally decreases with the increase of $\alpha$ at the same $u$. Furthermore, as $\alpha$ changes from 0° to 60°, the distance between two adjacent curves becomes smaller, and the curves of $\alpha = 45°$ and $\alpha = 60°$ are almost overlapped.

**3.4.2.2. Penetration tests.** Figure 3.20 illustrates the development of vertical loading capacity for a plate inclined at various angles. With the increase of the plate's inclination angle, the vertical force-displacement curves generally become flatter, which implies that the growth rate of the vertical loading capacity with the penetration depth is slower. This is

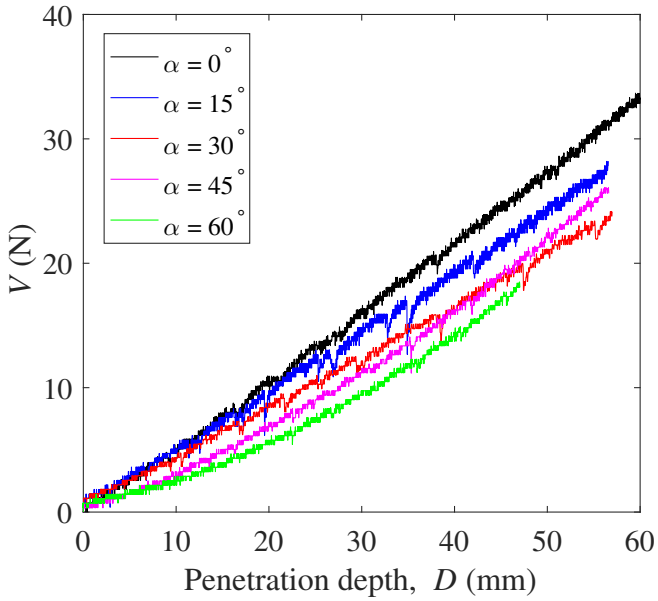


Figure 3.20. Development of vertical force with penetration depth in penetration tests.

clearly visible when the penetration depth $D < 35\,\text{mm}$. However, as the penetration depth $D > 35\,\text{mm}$, the increase of vertical loading capacity with the penetration depth for a plate with $\alpha = 45°, 60°$ are even faster than the other cases.

## 3.5. Summary

This chapter presented the experiments performed for observing the soil deformation evolution in the cutting and penetration process and for constructing the semi-analytical models described in Chapter 5 and 6. The detailed experimental procedure and preliminary discussion on the obtained results are provided. Key findings are summarized as follows:

(1) The progression of soil responses in the fundamental SMI processes, i.e.,cutting and penetration, was investigated by performing the PIV tests. For the cutting process, distinct soil responses were observed in loose and dense sand. In terms of the force-displacement

histories, the force generally increased with the displacement in loose sand, while the force oscillation with a large amplitude was observed during the process in dense sand. For the evolution of soil deformation, in loose sand, the shear band swept over a region first and then remained stationary at one position while some temporary sweep appeared randomly. In dense sand, the shear band remained fixed for long periods of time until rapid, repeated sweeps preceded a jump forward to a new location. In the penetration process, the evolution of soil deformation was investigated only on the sand at a dense state. The pattern of shear localization forming, breaking down, and fading away are repeatedly observed. In the process, the force increased with the depth overall.

(2) The experimental loading capacity of the vertical plate and inclined plate were investigated. For the vertical plate, the pure penetration test, horizontal cutting test, swipe test, and probe test were performed. For the inclined plate, the penetration test, positive and negative cutting tests, and the positive and negative swipe tests were conducted. The results of these tests were fully presented. With further analysis of the test results, the characteristic soil responses to the plate movements can be extracted as features for developing corresponding semi-analytical models, which will be presented in Chapter 5 and 6.

CHAPTER 4

# Theoretical model: sequential kinematic method in sand

## 4.1. Introduction

This chapter presents theoretical models using the sequential kinematic method (SKM) to predict soil responses during the process of biaxial compression, cutting, and penetration. The models are developed by enhancing the technique proposed by Kashizadeh [**173**] in the aspects of kinematics and material law, and generality. The models are built on a desire to achieve a balance between modeling accuracy and computation efficiency. In other words, they are expected to efficiently reproduce the primary information of interest for engineering practice, namely the resistance, deformation mechanism, and the evolution of material boundary and properties, without modeling or tracking other secondary information (e.g., stress and strain within the soil).

In this chapter, the numerical formulation of the model with enhanced material law is presented first, followed by a demonstration of the model performance with the example of biaxial compression. Then, a more practical deformation process — soil cutting is studied. The same cutting tests as the physical tests illustrated in Section 3.2.2 are simulated by using the theoretical model, and its predictions are compared with the experimental observations (Section 3.2.2) for validation. Furthermore, the theoretical model incorporating a richer deformation mechanism for simulating the penetration process is illustrated. The model's performance is evaluated by comparing the predictions against the experimental results obtained in Section 3.2.3.

## 4.2. Simulation of biaxial compression

This section provides an overview of the theoretical model with enhanced material law and kinematics. The numerical formulation and the model's performance are presented with the help of the example of biaxial (plane strain) compression.

### 4.2.1. Formulation

The theoretical model consists of first evaluating the displacement field within an increment of deformation based on the kinematic method of limit analysis [**174, 175**] and then sequentially updating the deformed configuration based on the optimal incremental displacement field. In analyzing the incremental displacement field, it is assumed that all plastic deformation occurs in a layer (i.e., shear band) with finite thickness. The soil in the shear band deforms with a homogeneous strain. The soil above it moves as a rigid block, and the soil below it is at rest. The features of the shear band need to be predefined for any particular test setup. Consider the biaxial compression test [**176**] as an example. The shear band is simplified as a single straight slope connecting the left and right side of the specimen at any elevation [**177**], which is shown in Figure 4.1(a). The inclination of the band from the vertical is $\beta$. The Mohr-Coulomb yield criterion with an internal friction angle, $\phi$, is applied to the soil. Based on the yield condition and equilibrium, the force $P$ required to load an increment of displacement can be calculated by:

$$P = -W + |P_{c1} - P_{c2}| \tan(\phi + \beta) \tag{4.1}$$

where $W$ is the weight of soil above the centerline of the shear band (red line in Figure 4.1(a)); $P_{c1} = \sigma_c L_1$; $P_{c2} = \sigma_c L_2$; $\sigma_c$ is the confining pressure; $L_1$, $L_2$ are the height above shear band

at the left and right side, respectively. In a generalized form, the force $P$ can be written as: $P = P(\boldsymbol{\alpha_s}, \boldsymbol{\alpha_b})$, where $\boldsymbol{\alpha_s}$ are for describing soil properties and $\boldsymbol{\alpha_b}$ are geometric parameters related to the shear band.

To determine the position and orientation of the shear band in biaxial compression, the edges representing the left and right faces of the specimen are discretized by the nodal points shown in Figure 4.1(b). As shown in the figure, nodes on the left and right are referred to $I$ and $J$ nodes, respectively. The slope connecting each pair of the nodes (one $I$ node and one $J$ node) represents a possible location of the shear band. The optimal location of the shear band and the force $P$ are determined based on the principle of minimum effort, which states that the expected deformation is the one requiring the least force. By using the grid search to minimize the force $P$ in Equation 4.1, the optimal position and orientation of the shear band $\beta^*$, and the corresponding optimal force $P^*$ within an increment, can be obtained. Then, the overall deformed shape is updated, as shown in Figure 4.1(b). The soil above the lower boundary of the shear band moves at an angle relative to the shear band equal to the dilation angle $\psi$. The magnitude of incremental displacement, $v$, is determined based on the defined displacement loading rate, $v_0$. It is noted that $v$ is linearly distributed on the shear band from its lower boundary to the upper boundary, the same as the incremental shearing displacement ($v_t$) and volumetric displacement ($v_v$).

Some additional features, such as updating the unit weight of sand in the process and adding/removing nodes to maintain the robustness of computation, are incorporated in this technique (see the work [**178, 173**] for details).

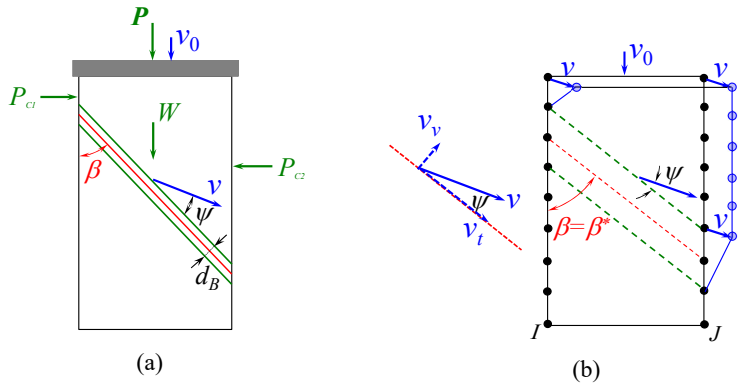


Figure 4.1. Theoretical model for biaxial compression test: (a) assumed deformation mechanism for an increment of displacement; (b) discretization, optimization, and updating.

### 4.2.2. Material model

A material law incorporating the effects of hardening and softening, as well as the dilatancy and compaction within the shear band, is schematically illustrated in Figure 4.2. The friction angle ($\phi$) and dilation angle ($\psi$) are defined as a piecewise linear function of the accumulated shear displacement $u_t$, which neglects elastic deformation and captures the essential features of hardening and softening observed in element tests on sand [**179**]. Friction angle $\phi$ increases linearly from the yield friction angle ($\phi_c$) to the peak friction angle ($\phi_p$) to capture hardening, and this is followed by a linear decrease to the residual friction angle ($\phi_r$) to capture softening. Similarly, dilation angle $\psi$ increases from $\psi_c$ to the peak dilation angle $\psi_p$ and then decreases to residual dilation angle $\psi_r = 0$. The soil contracts and dilates as $\psi$ is negative and positive, respectively. The peak values of $\phi$ and $\psi$ are reached simultaneously at $u_t = u_p$, and their residual values are reached at $u_t = u_r$. In the numerical simulation, each node is assigned an $u_t$, so as to assign the corresponding $\phi$ and $\psi$ to track the instantaneous soil properties.

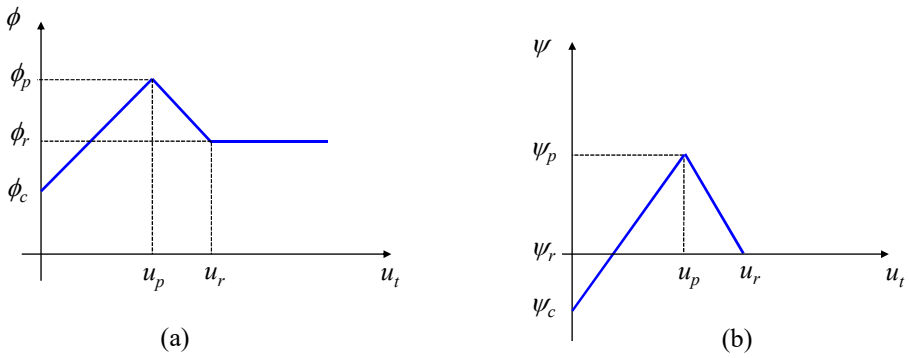


Figure 4.2. Material law of sand: variation of (a) friction angle with accumulated displacement (b) dilation angle with accumulated displacement.

### 4.2.3. Analysis of biaixal compression in sand

To show the performance of the proposed theoretical model, an example predicting the evolution of strain localization under biaxial compression is presented. The predictions are compared with experimental results obtained by Desrues on both loose and dense sand [**8**]. The loose specimen was prepared in a dimension of 25 cm (height) $\times$ 11.3 cm (width) $\times$ 3.5 cm (thickness) with the initial volumetric unit weight of 13.68 kN/m$^3$, and the test was performed at a confining pressure of 85 kPa. The dense specimen was prepared in a dimension of 35 cm (height) $\times$ 17.5 cm (width) $\times$ 3.5 cm (thickness) with the initial volumetric unit weight of 15.65 kN/m$^3$, and the test was performed at a confining pressure of 80 kPa. In the numerical analysis, the main parameters describing the soil properties for simulating the tests are listed in Table 4.1. Among these parameters, the shear band widths ($d_B$) are evaluated based on the experimental measurements [**8**], and all the other values are determined by matching the predicted force-displacement history to the experimental results as shown in Fig 4.3.

The predicted progression of soil deformation is compared with the experimental observations in terms of shear strain and volumetric strain fields for the photographic increments noted in Figure 4.3. The shear strain and volumetric strain are calculated as $\epsilon_s = (\epsilon_1 - \epsilon_3)/2$

Table 4.1. Main parameters used for simulating the biaxial compression.

| State | $E$ (kPa) | $\phi_c(^\circ)$ | $\phi_p(^\circ)$ | $\phi_r(^\circ)$ | $\psi_c(^\circ)$ | $\psi_p(^\circ)$ | $\psi_r(^\circ)$ | $\phi_w(^\circ)$ | $u_p$ (mm) | $u_r$ (mm) | $d_B$ (mm) |
|---|---|---|---|---|---|---|---|---|---|---|---|
| Loose | 14500 | 34 | 34 | 21 | -15 | 8 | 0 | 2 | 0.25 | 10 | 20 |
| Dense | 21000 | 47.3 | 43.3 | 37.4 | -5 | 15 | 0 | 0 | 0.2 | 10 | 25 |

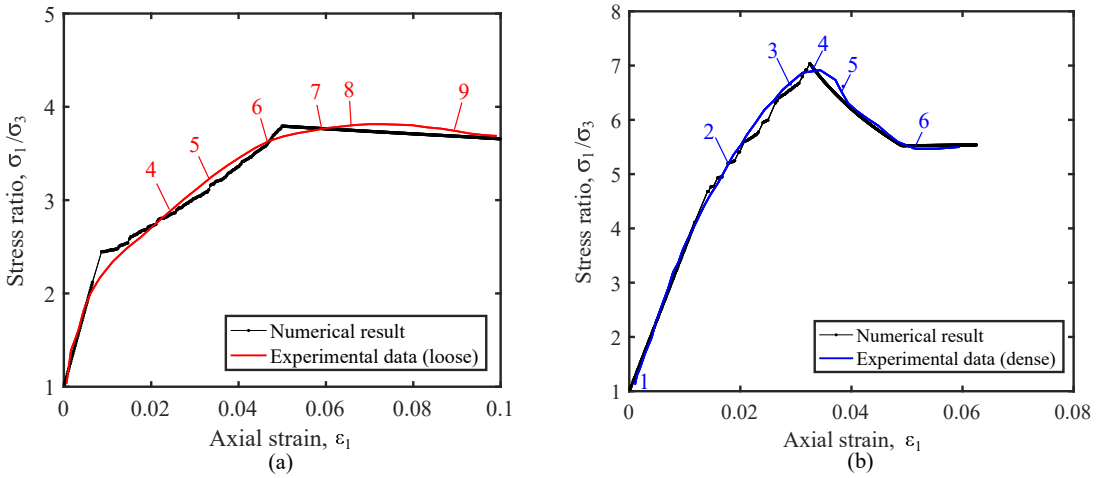


Figure 4.3. Axial stress vs. vertical strain curve of biaxial test in (a) loose sand (shf02 in [**8**]); (b) dense sand (shf06 in [**8**]). The numbers noted on each curve are the numbers of photographs for stereophotogrammetic analysis and PIV analysis.

and $\epsilon_v = \epsilon_1 + \epsilon_3$, respectively. In experiments, Desrues uses stereophotogrammetry as a quantitative tool to measure the (incremental) strain fields [**8**], which are shown as the top rows of Figure 4.4 - 4.7. The size of the symbols is proportional to the value of the relevant quantity. As far as volumetric strain is concerned, square symbols are for dilatancy and hexagons for contraction. In the numerical predictions, we obtain these incremental strain fields (illustrated in the bottom rows of Figure 4.4 - 4.7) by performing virtual particle image velocimetry (PIV) analysis. Specifically, a reference image with the size the same as the plane size of the specimen is firstly generated by projecting black dots on a white background. The following deformed images are created with imposing the predicted deformation at each increment, which is implemented by moving the dots on the image. Then, these virtual images

are loaded in GeoPIV-RG, a free MATLAB-based image analysis module to calculate the displacement fields. Based on the obtained displacements, the strain fields are computed by using moving least square (MLS) interpolants (the same method used in the physical PIV tests and the details are described in Appendix A). We use the positive volumetric strain to represent dilatancy and the negative value to represent contraction.

Figure 4.4 and 4.5 illustrate the evolution of the incremental shear strain and volumetric strain fields, respectively, for biaxial compression in loose sand. It is identified that the experimental observations can be predicted by the theoretical model quantitatively. Measured incremental strains (top row in Figure 4.4 and 4.5) indicate that the shear band takes place until the increment 6-7, before which the soil deforms in a diffuse and non-homogeneous mode (increment 4-5 and 5-6). Counterintuitively, this diffuse deformation can be interpreted as the accumulation of continuous localized deformation propagating over regions, as suggested by the theoretical model. Besides, incremental volumetric strain fields (Figure 4.5) show that the soil is mainly compacting at the stage of diffuse deformation and starts to dilate when shear band forms.

The predicted evolution of soil deformations in dense sand can also match the experimental measurements quantitatively, as shown in Figure 4.6 and 4.7. The measured shear strain fields (top row in Figure 4.6) illustrate that prior to 'photograph 3,' while no distinct shear band was observed, the deformation is non-homogeneous, and especially is roughly X-shaped in the increment 2–3. During increment 3–4, a pronounced strain localization forms in the middle portion of the specimen, and it maintains throughout the test and finally intersects the entire specimen. In the localized regions, volumetric strain fields (Figure 4.7) imply that soil is always dilating. The similar evolution of strain localization is predicted

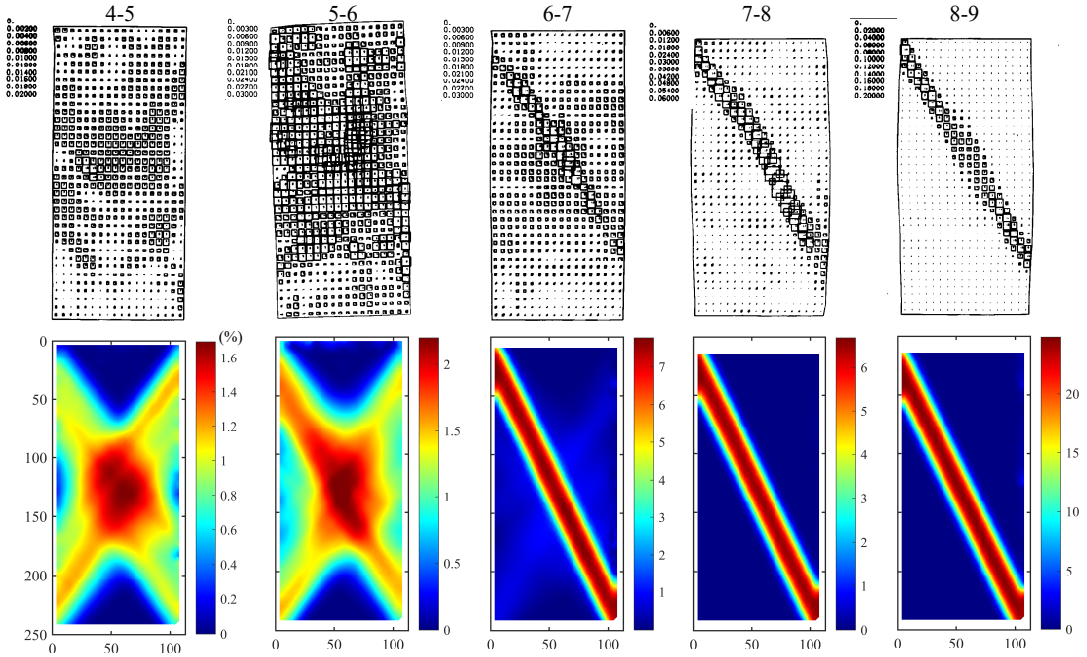


Figure 4.4. Experimental (top row) and predicted (bottom row) incremental shear strain field under biaxial compression in loose sand (shf02 in [**8**]).

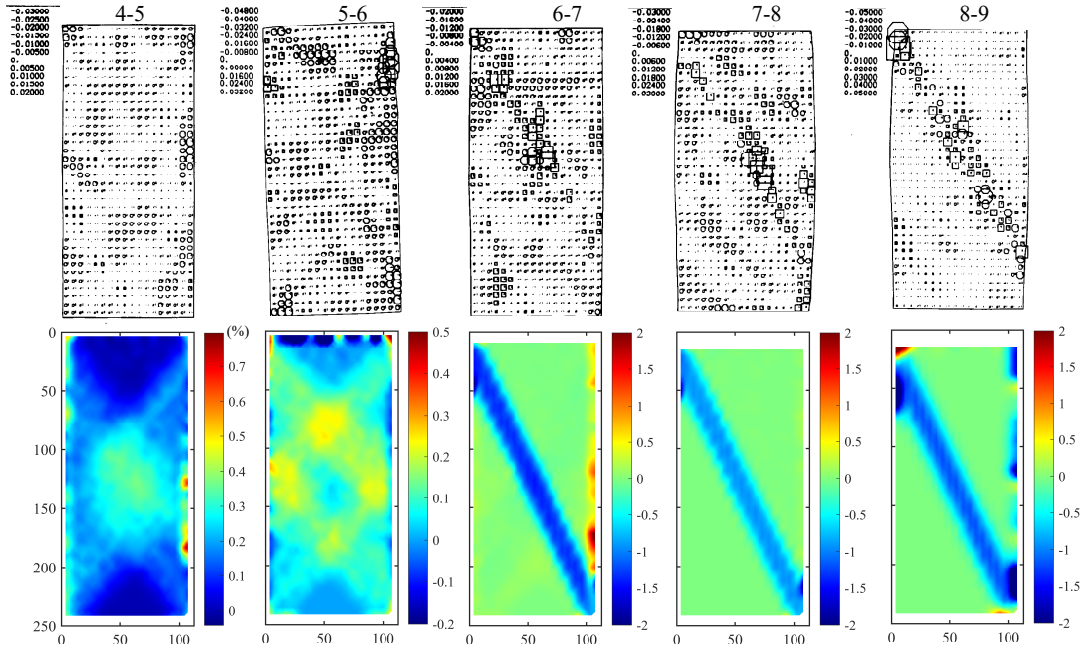


Figure 4.5. Experimental (top row) and predicted (bottom row) incremental volumetric strain field under biaxial compression in loose sand (shf02 in [**8**]).

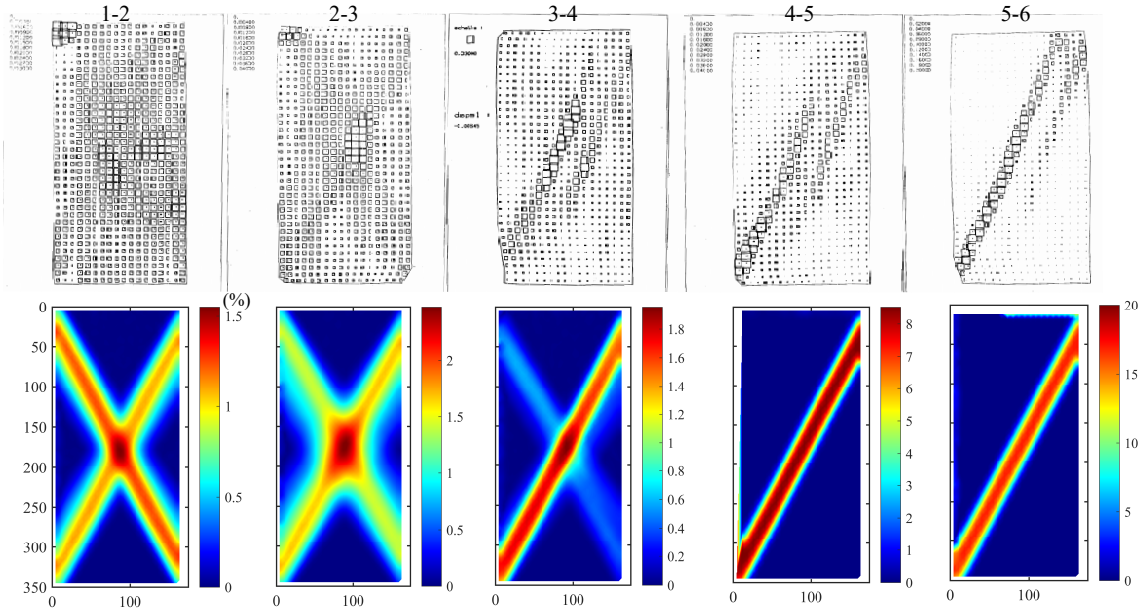


Figure 4.6. Experimental (top row) and predicted (bottom row) incremental shear strain field under biaxial compression in dense sand (shf06 in [**8**]).

by the theoretical model. At first, the shear band with various orientations continuously appears at different positions, composing the non-homogeneous deformation. Then the strain localization maintains at one location, forming the distinct shear band.

## 4.3. Simulation of cutting process

### 4.3.1. Numerical model setup

The assumed feature of localized deformation for the cutting process is described in Figure 4.8(a). The shear band is developed from the tip of the plate to the soil surface, and it is inclined at an angle $\beta$ from the horizontal. Based on the Mohr-Coulomb yield criterion and equilibrium, the force $P$ required to displace the plate is calculated by:

$$P = W \frac{\tan(\beta + \phi)}{\cos\phi_w - \sin\phi_w \tan(\beta + \phi_w)} \tag{4.2}$$

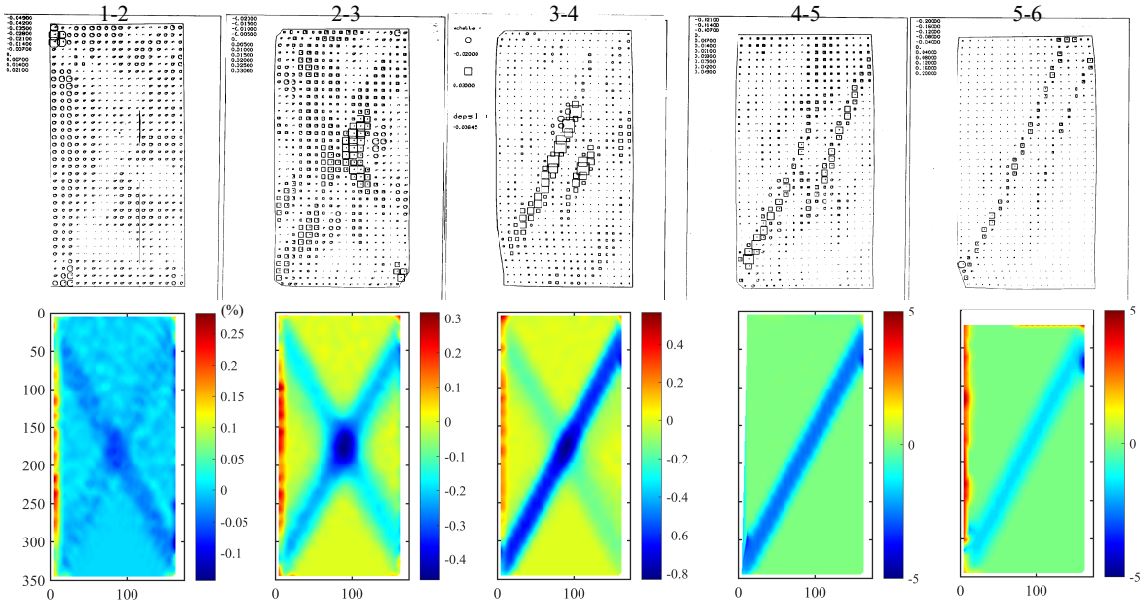


Figure 4.7. Experimental (top row) and predicted (bottom row) incremental volumetric strain field under biaxial compression in dense sand (shf06 in [**8**]).

where $W$ is the weight of soil above the mid of the shear band (red line in Figure 4.8(a)) and $\phi_w$ is the friction angle between soil and plate.

To simulate the cutting process, the soil surface is discretized by the nodal points shown in Figure 4.8(b). Each node represents a possible location for the shear band (referring to the mid-plane of the shear band). The optimal orientation of the shear band $\beta^*$ and optimal force $P^*$ within an increment are obtained by minimizing the force $P$. Then, as shown in Figure 4.8(c), the overall deformed shape is updated by translating the soil above the lower boundary of the shear band at an angle relative to the shear band equal to the dilation angle $\psi$.

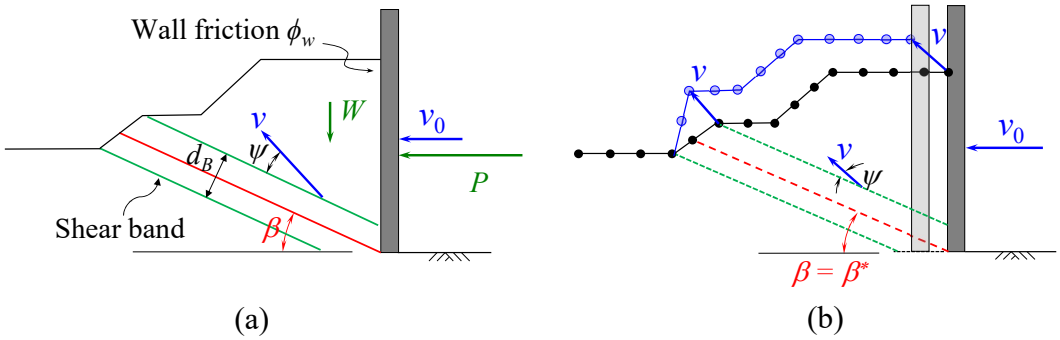


Figure 4.8. Numerical setup of soil cutting model: (a) assumed deformation mechanism for an incremental of displacement; (b) discretization, optimization and updating.

### 4.3.2. Theoretical modeling versus experiments

The same cutting tests as the physical tests described in Section 3.2.2 are simulated using the theoretical model, of which results are compared with the experimental observations (Section 3.2.2) in terms of characteristic force-displacement history and evolution of shear band positions. The comparisons are illustrated in Figure 4.9 and Figure 4.10 for cutting in loose and dense sand, respectively. In the figures, the shear band positions are located through finding the maximum shear strain along the centerline of the plate depth. Table 5.2 lists the main parameters used to generate the numerical predictions. Among these parameters, $D_{50}$ is the actual average particle diameter of the used sand. The band width $d_B$ is estimated based on PIV analysis, and all the other values are determined by matching the predicted force-displacement history to the experimental result. These fitting parameters are reasonable for describing the properties of loose sand and dense sand, providing some level of validation for the theoretical model. Besides, it is noted that the $\phi_p$, $\phi_r$ and $\psi_p$ for dense sand are interrelated by $\phi_p = \phi_r + 0.8\psi_p$ to satisfy the relationship of the strength and dilatancy of sand proposed by Bolton [**180**], and $\phi_w = 0.6\phi_r$, which is set based on the

Table 4.2. Main parameters used for simulating the cutting process.

| State | $\phi_c(^\circ)$ | $\phi_p(^\circ)$ | $\phi_r(^\circ)$ | $\psi_c(^\circ)$ | $\psi_p(^\circ)$ | $\psi_r(^\circ)$ | $\phi_w(^\circ)$ | $u_p$ (mm) | $u_r$ (mm) | $D_{50}$ (mm) | $d_B$ (mm) |
|---|---|---|---|---|---|---|---|---|---|---|---|
| Loose | 30 | 35 | 35 | -8 | 0 | 0 | 21 | 0.4 | 0.4 | 0.19 | $14D_{50}$ |
| Dense | 39 | 39 | | 5 | 5 | | | 0 | 4 | | |

study of interface friction angles between steel and sand [**181**] as well as the experimental setup used in this work, referring to the sand particle size and smoothness of the plate.

The results indicate that the theoretical model can predict the key features of the experimental observations. For the case of cutting in loose sand (Figure 4.9), the prediction is capable of capturing the force-displacement behavior and the evolution of shear band positions measured from the experiment. Specifically, the sweeping stage (indicated by the significant variation of shear band position), the stationary stage, and the temporary sweeping (suddenly drastic change of shear band position) are observed in the simulation. However, the predicted shear band generally appears at a location farther from the plate than that in experiments. For the case of cutting in dense sand (Figure 4.10), the predicted force-displacement history is also characterized by a succession of jumps corresponding to the transition of the shear band location, which is the same as that observed in experiments. The presented result shows the amplitude of the oscillation can be predicted while the frequency of the oscillation is not matched precisely. It is noted that, by trial and error, we found the theoretical model cannot accurately predict the magnitude of the force, the amplitude, and the frequency of the oscillation simultaneously.

In addition to predicting the force-displacement and soil deformation in the cutting process, the theoretical model identifies and explains the deformation mechanism in sand: continuous discontinuity evolves over regions. In loose sand, strain localization induces hardening on the soil, such that more effort (force) is required to continue the deformation on

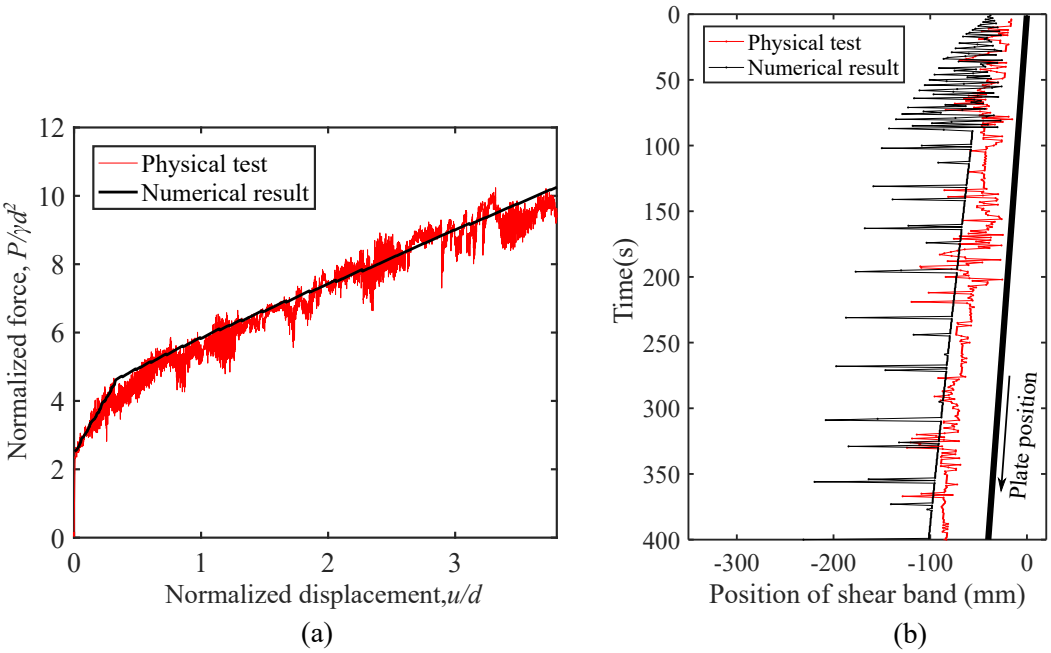


Figure 4.9. Comparison of experimental and predicted (a) force-displacement history; (b) positions of shear band in $x$-axis at the mid of cutting depth as cutting in loose sand.

the same shear band. In this case, the shearing tends to occur at a new location where the soil strength is lower. The new position usually is close to the previous one as the increase of force induced by the change of shear band position (reflected by the $\beta$ in Equation 4.2) is small. After successive shear bands form at variable locations, the sand over a region is hardened, and developing shear band either at a shallower or steeper inclination (larger or lower $\beta$) will take more effort than shearing the soil in the hardened region. Therefore, the localized deformation will continue at a location in the region. In dense sand, the soil on the shear band is softening, making it easier to continue the deformation on the same shear band. However, as the shear band stays at one position, its inclination ($\beta$) increases, resulting in the growth of force. At a time, shearing the softened sand on a steeper shear

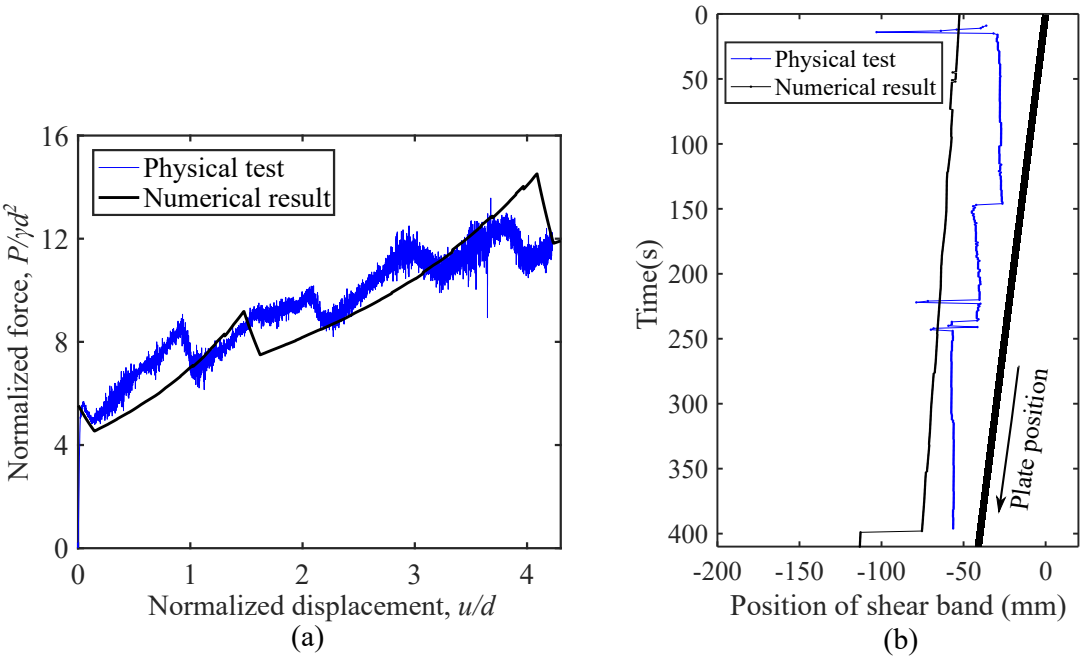


Figure 4.10. Comparison of experimental and predicted (a) force-displacement history; (b) positions of shear band in $x$-axis at the mid of cutting depth as cutting in dense sand.

band needs more force than shearing the sand with higher strength on a shallower position, so the transition of shear band occurs.

### 4.4. Simulation of deep penetration process

Based on the experimental observation of deformation field during penetration process (illustrated in Section 3.2.3), the deformation mechanism in the penetration process cannot be characterized by a single straight slip surface. To simulate the penetration process by SKM, the original model is enhanced by incorporating a richer deformation mechanism. Specifically, as illustrated in Figure 4.11(a), a system of rigid blocks separated by velocity discontinuities is introduced to capture the soil deformation mechanism. Within an increment of penetration, the deformation field is determined by minimizing the resistance on the

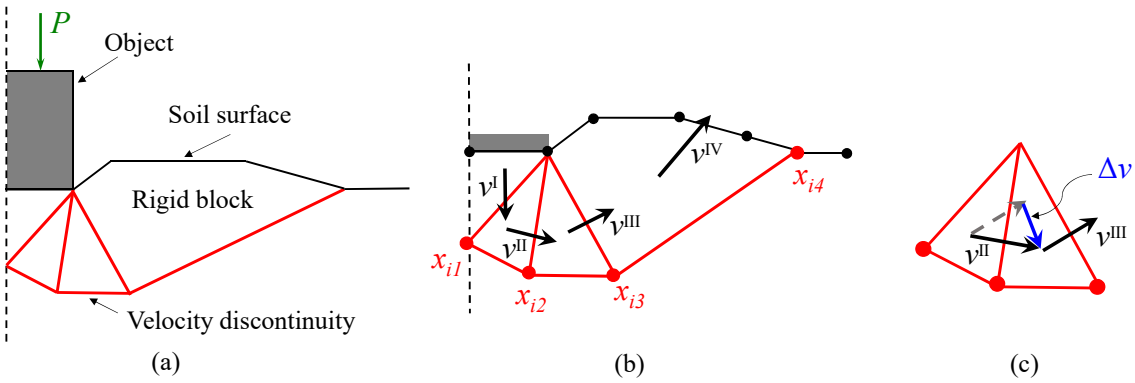


Figure 4.11. SKM-based model for simulating penetration process in sand (a) deformation mechanism; (b) variables subject to optimization; (c) difference of velocity between blocks.

plate. Then, the obtained optimal velocity field is integrated over time increments to update the material free surface and position of the plate. In this section, the numerical formulation and update strategy of the model are illustrated, and their performance is demonstrated by comparing the prediction against the experiment results obtained in Section 3.2.3). It should be noted that the work in this section is completed with the great help from Dr. Zhenhao Shi by private communication [**182**].

### 4.4.1. Numerical formulation

The deformation field represented by the mechanism in Figure 4.11(a) is constrained by the geometry of the blocks and their velocities. To determine the deformation field in one increment, the r-adaptive kinematic method is used, in which both velocities and nodal positions of the blocks (illustrated in Figure 4.11(b)) are treated as variables to be optimized [**183, 184, 185**]. In this model, the r-adaptive kinematic method is implemented through a nested optimization procedure. The lower layer of the optimization determines the optimal velocities with a fixed mesh by second-order cone programming (SOCP), and

the upper layer computes the optimal nodal positions from a non-linear optimization. The details of these two optimization layers are as follows.

**4.4.1.1. Optimization of velocity field for fixed mesh.** For a deformation field consisting of rigid blocks, the energy dissipation within the material only occurs at the velocity discontinuities between blocks. For a perfectly plastic material that obeys Mohr-coulomb yield criterion and the plastic potential of $g = \tau_n – \sigma_n \tan\psi - c$, the energy dissipation rate within a velocity discontinuity line can be expressed as [**186**]:

$$\dot{d} = [c + \sigma_n(tan\phi - tan\psi)]|\Delta v_t|l \tag{4.3}$$

where $c$, $\phi$ and $\psi$ are the cohesion, friction angle and dilation angle of the material, respectively; $\sigma_n$ is the normal stress at the discontinuity line; $l$ denotes the length of discontinuity; and $\Delta v_t$ is the tangential velocity jump along the discontinuity. By using the non-associated flow rule generated from the plastic potential $g$, the following 'jump condition' can be derived:

$$\Delta v_n = |\Delta v_t| \tan\psi \tag{4.4}$$

where $\Delta v_n$ denotes the normal velocity jump.

For the system defined in Figure 4.11(a), the energy balance (the rate of internal energy dissipation equating to the work rate of external forces for an assembly of blocks) can be expressed as:

$$\sum_{j=1}^{N_D} \dot{d}_j = -\sum_{k=1}^{N_B} \gamma A_k v_{2k} + P v_p \tag{4.5}$$

In the equation, $v_p$ is the velocity of the plate; $N_B$ is the number of blocks, $A_k$ and $v_{2k}$ are the area and vertical velocity of the $k^{th}$ block, respectively; $N_D$ is the number of the velocity discontinuities between the blocks, and the subscript $j$ denotes the quantities corresponding to the $j^{th}$ discontinuity line. In this problem, there are two types of discontinuities: the velocity discontinuities within the soil material and those occurring at the interfaces between the plate and the soil material. The energy dissipation at the interface is calculated by replacing the $c$, $\phi$ and $\psi$ in Equation 4.3 with $c_i$, $\phi_i$ and $\psi_i$. Based on the equation of energy balance, the resistance on the plate $P$ can be formulated, which will be minimized to obtain the optimal velocity field for this problem.

To preserve a linear objective function in the SOCP, the energy dissipation $\dot{d}$ should be computed by replacing the $|\Delta v_t|$ in Equation 4.3 with a dummy variable $\mu$:

$$\begin{aligned} \dot{d} &= [c + \sigma_n(tan\phi - tan\psi)]l\mu \\ \mu &\geq \sqrt{(\Delta v_t)^2} \end{aligned} \tag{4.6}$$

The constraint in the above equation is in the form of second-order cone constraint. Equation 4.6 can represent the exact energy dissipation rate only when the constraint is achieved with equality (i.e $\mu = |\Delta v_t|$). For the presented problem, this condition is always satisfied because that the SOCP is formed such that the dummy variable $\mu$ is minimized.

Finally, the optimization of the velocity field for a fixed mesh can be written in the form of SOCP as follows:

$$
\begin{aligned}
min \quad & P = \frac{1}{v_p}\left(\sum_{j=1}^{N_D} \dot{d}_j + \sum_{k=1}^{N_B} \gamma V_k v_{2k}\right) \\
s.t. \quad & \Delta v_{ij} n_{ij} = \mu_j \tan\psi, j = 1, ...., N_D \\
& \dot{d}_j = [c + \sigma_{nj}(\tan\phi - \tan\psi)]\mu_j l_j, j = 1, ...., N_D \\
& \mu_j \geq \sqrt{(\Delta v_{ij} t_{ij})^2}, j = 1, ...., N_D
\end{aligned} \tag{4.7}
$$

Note that to derive the above formulation, $\Delta v_t$ and $\Delta v_n$ are calculated by $\Delta v_i t_i$ and $\Delta v_i n_i$, respectively, where $\Delta v_i$ is the velocity jump (illustrated as Figure 4.11(c)); $t_i$ is the unit vector parallel to the plate of a discontinuity; $n_i$ is the unit vector normal to the plane, and the subscript $i = 1$, 2 represents the horizontal and vertical components of the variables. In addition, a velocity of unity is assigned to the plate ($v_p = 1$) for convenience. With these conditions, the SOCP optimization work is implemented by the Mosek toolbox integrated with MATLAB [**187**] to obtain the optimal velocity field for a fixed mesh of blocks.

**4.4.1.2. Optimization of nodal positions of rigid blocks.** Equation 4.7 computes the optimal resistance force on the plate and velocity field for a fixed set of blocks. The positions of these blocks, determining the locations of potential velocity discontinuities and weights of blocks, are free to move, and thus have vital influence on the optimization work in Equation 4.7. For optimizing the nodal positions of the blocks , a non-linear optimization problem is formulated as follows:

$$
\begin{aligned}
min \quad & P_{opt}(x_{im}), i = 1, 2, m = 1, 2, 3, 4 \\
s.t. \quad & A_k(x_{im}, x_{14}) \geq 0, k = 1, ...., N_B \\
& x_{im}^l \leq x_{im} \leq x_{im}^u \\
& x_{14} \geq B
\end{aligned}
\tag{4.8}
$$

where the objective function is the limit resistance force computed for a given set of nodal positions $x_{im}$ (the subscript $i$ represents the $i^{th}$ component of the position vector, and the subscript $m$ indicates the $m^{th}$ node), evaluated in the same way as in the previous section (4.7). In the model configuration (Figure 4.11 (b)), the last node can be either on the soil free surface or within the soil. For the former case, the coordinates of last node $x_{i4}$ are correlated. More specifically, only the horizontal coordinate $x_{14}$ is regarded as an unknown, and the vertical coordinate is determined accordingly. For Equation 4.8, the first set of constraints ensures that the areas of blocks $A_k$ are always positive for preventing the inter-penetration of rigid blocks and keep computational stability. The second set of constraints defines the allowable limits for certain nodal position components, which are used to ensure that the nodes do not surpass the material free surface. The last constraint requires the horizontal coordinate at the last node greater than the half-width of the plate ($B$), which is imposed to avoid the node being on the base of plate. The above non-linear optimization work (Equation 4.8) is solved by the FMINCON solver of MATLAB. It is important to note that the FMINCON is a local optimizer, and it behaves more effective when the initial nodal positions of the rigid block are close to the optimal ones. Therefore, a careful setup of the

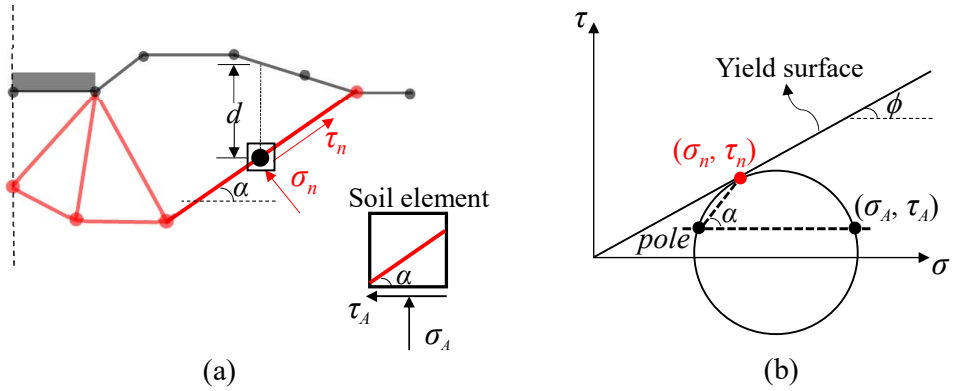


Figure 4.12. Method for estimating the normal stress on a velocity discontinuity (a) element analysis on a discontinuity; (b) Mohr circle for determining the normal stress.

initial nodal positions based on the PIV result of the physical test is crucial to the model performance.

In summary, by implementing the nested optimization framework consisting of a lower layer (Equation 4.7) and an upper layer (Equation 4.8), the limit resistance force corresponding to the optimal velocity field and optimal configuration of blocks can be obtained.

**4.4.1.3. Estimation of normal stress on discontinuities.** The above optimization formulations can be easily carried out for the penetration process in the material obeying the associated flow rule, such as metals and clay, since the energy dissipation rate ($\dot{d}_j$) in Equation 4.7 can be written in a purely kinematic form, i.e., $\dot{d}_j = c\mu_j L_j$. However, sand generally exhibits non-associated flow, resulting in a stress-dependent energy dissipation rate on the discontinuities. Hence, a method to estimate the stress on the velocity discontinuities ($\sigma_n$) is required.

Figure 4.12 schematically illustrates the method for estimating the normal stress on a discontinuity. The estimation is made with two assumptions: (1) the normal stress $\sigma_n$ on each discontinuity is uniform and can be represented by the value at its midpoint (the black

point on red line in Figure 4.12(a)); (2) the vertical stress $\sigma_A$ at any position in soil is the sum of the weight of the soil up to surface and the stress induced by plate. In this study, the latter is estimated by using the plane strain solution of Boussinesq's method, which can be readily derived by integrating the Boussinesq equation with respect to a uniform distributed load $P$. Thus, the total vertical stress is determined as:

$$\sigma_A = \gamma d + \frac{P}{\pi} f(x_1 + x_2) \tag{4.9}$$

In the equation, $\gamma$ is the unit weight of soil; $d$ is the depth of the midpoint; $P$ is the uniform stress that the plate performs at the soil surface, which is evaluated as the limit load obtained in the last loading step; $f$ is a factor determined by the position of the midpoint ($x_{1,2}$ are the coordinates at the position). For simplicity, the full expression of the second term in Equation 4.9 is not present here, and readers are referred to the literature [**188**] for complete details of the formulation. To estimate the normal stress on the velocity discontinuity, the soil element at its midpoint is taken for analysis. The normal stress on the horizontal plane of the element is the vertical stress $\sigma_A$ computed by Equation 4.9. By using the Mohr circle and the concept of *pole*, the stress state on the discontinuity can be calculated with the implication that the stress state is also on the yield surface. The concept of 'pole' is that any straight line drawn from the pole will intersect the Mohr circle at a point that represents the stress state on a plane inclined at the same orientation (parallel) as that line. Specifically, as illustrated in Figure 4.12(b), a line is drawn from the 'pole' with an angle of $\alpha$ to the horizontal, and the point interacting the yield surface indicates the stress state at the velocity discontinuity. By establishing a system of equations for the geometric relationships

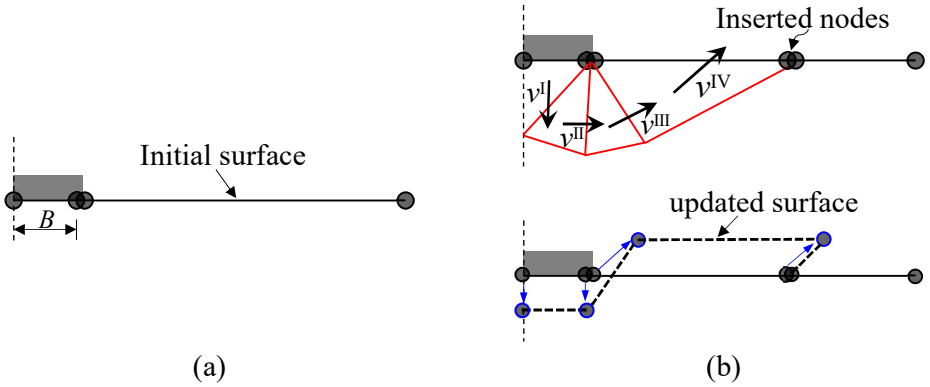


Figure 4.13. Schematic illustrating the update of the soil free surface according to the computed velocity field: (a) initial setup of free surface; (b) update process of the free surface.

in Figure 4.12(b), the equation for computing the normal stress on the discontinuity can be derived:

$$\left(\sigma_A - \frac{\sigma_n}{\cos^2\phi}\right)^2 + \left(\sigma_A(\tan\phi - \tan\alpha) + \left(\frac{2\sigma_n}{\cos^2\phi} - \sigma_A\right)\tan\alpha\right)^2 = \left(\frac{\sigma_n \tan\phi}{\cos\phi}\right)^2 \tag{4.10}$$

Taking Equation 4.9 into Equation 4.10, the full expression is obtained.

### 4.4.2. Update and correction of material free surface and soil blocks

In this model, the deformation of the soil is tracked by a discretized free surface. As shown in Figure 4.13(a), the free surface is initially set up with four nodes, among which two nodes are at the right edge of the plate. The two nodes are at the same position, but one is considered at the base of plate while the other one pertains to the last soil block. At each step, based on the obtained optimal nodal positions of blocks, two new nodes are inserted on the same position of the last node of the blocks (i.e., $x_{i4}$) to form the new free surface. For these two nodes, only one is considered belong to the last soil block. To update the displacements of

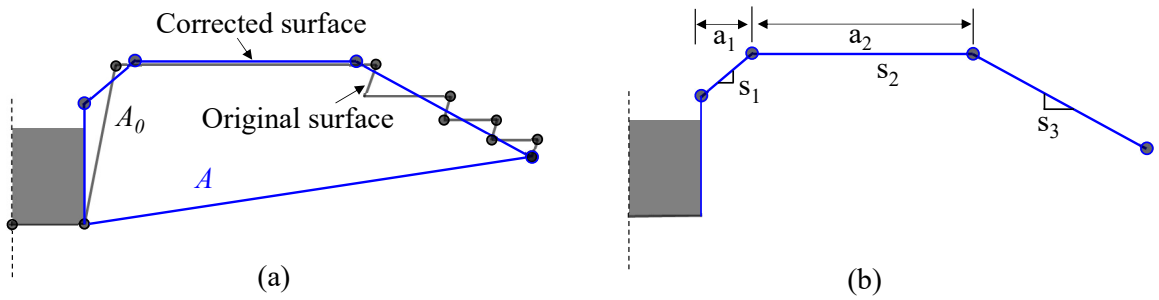


Figure 4.14. Schematic illustrating the simplification and correction of the soil free surface: (a) original and corrected free surface; (b) line segments describing the free surface and fitted to original nodes.

these nodes along the free surface, one-step forward Euler method is used in accordance with the obtained optimal velocity field. More explicitly, the nodal displacements at the end of a pseudo time increment $\Delta T_n$ can be computed by

$$u_{im}^{n} = u_{im}^{n-1} + v_{im}^{n-1}\Delta T_n, \quad i = 1, 2 \quad \text{and} \quad m = 1, 2, \ldots \tag{4.11}$$

where $u_{im}$ and $v_{im}$ are the displacement and velocity vectors at the $m^{th}$ node, respectively. In the similar way, the position of the plate is updated according to

$$u_{ip}^{n} = u_{ip}^{n-1} + v_{ip}^{n-1}\Delta T_n, \quad i = 1, 2 \quad \text{and} \quad p = 1, 2 \tag{4.12}$$

where $u_{ip}$ and $v_{ip}$ are the displacement and velocity vectors at the $p^{th}$ node on the base of the plate.

As the soil surface is updated as the number of time increments increases, a number of nodes are added to the surface and some unrealistic predictions of surface geometry might occur, such as a sharp inverse corner and a surface with inclination angle larger than the soil friction angle. Thus, the free surface needs to be simplified and corrected appropriately. The simplification and correction are performed simultaneously through fitting three line

segments to the original nodes with using a nonlinear least-squares solver in MATLAB. The line segments are shown in Figure 4.14(b) and can be described by a piece-wise function:

$$F(x) = a_0 + s_2 x + (s_2 - s_1)\max(a_1 - x, 0) + (s_3 - s_2)\max(x - a_1 - a_2, 0) \tag{4.13}$$

where $x$ denotes the horizontal coordinate of the lines; $s_1, s_2, s_3$ are the slopes of the three line segments; $a_1$ is the horizontal coordinate of the first break point; and $a_2$ is the horizontal distance between the first and second break point. The fitting parameters $s_{1,2,3}$ and $a_{1,2}$ are bounded as follows:

$$\begin{aligned} & s_1 < \tan\phi, |s_2| < tol, s_3 > -\tan\phi \\ & a_1 > min(x_{1m}), a_1 + a_2 < max(x_{1m}) \\ & |A - A_0| < tol \end{aligned} \tag{4.14}$$

where $x_1 m$ are the horizontal coordinates of the nodes along the original free surface; $A$, $A_0$ is the area enclosed by the new nodes and the original nodes, respectively. The first set of constraints ensure the inclination angles of the surface are less than the soil friction angle. To make the break points (junctions) of the line segments within the range of original free surface, the second set of constraints in Equation 4.14 are adopted. The last constraint is set to correctly satisfy the mass conservation with using a *tol* of $1e-4$. After obtaining the fitted line segments, the original nodes are replaced with the new nodes (i.e. all endpoints of the piece-wise line) for forming the corrected free surface.

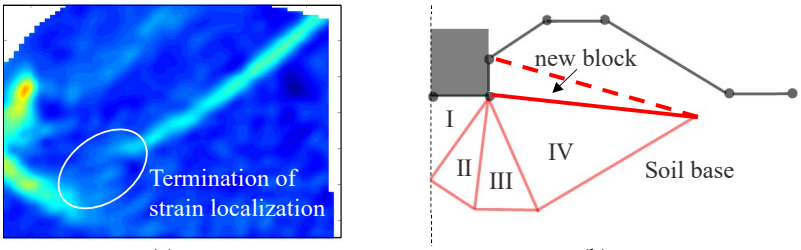


Figure 4.15. Schematic illustrating the correction of soil blocks: (a) physical evidence of velocity discontinuity terminating in soil (obtained from Section 3.2.3); (b) correction of soil blocks by adding a new block.

When the plate keeps penetrating into sand with a large displacement, the shear localization (velocity discontinuity) might terminate in soil instead of extending to the free surface. As illustrated in Figure 4.15(a), this phenomenon was observed in the PIV test presented in Section 3.2.3. In this case, the velocity discontinuities of the fourth block can never simultaneously satisfy jump condition of Equation 4.4. Therefore, an approach arranging the soil blocks for meeting the constraint is required. Figure 4.15(b) shows the correction of soil blocks: a new block is added to the original configuration with the assumption that only elastic compression happens along the interface between the block and base (dashed line in Figure 4.15(b)). This assumption implies the interface is not a real velocity discontinuity, and the new block consists of two velocity discontinuities (i.e. the sides of the new block except the dashed line in Figure 4.15(b)). Thus, the jump condition can be satisfied in the new configuration.

### 4.4.3. Analysis of penetration process: theoretical modeling versus experiments

The performance of the proposed SKM model is examined by the case of a flat rough plate penetrating in dense sand. In the example, the plate width is 2 m, which is chosen to

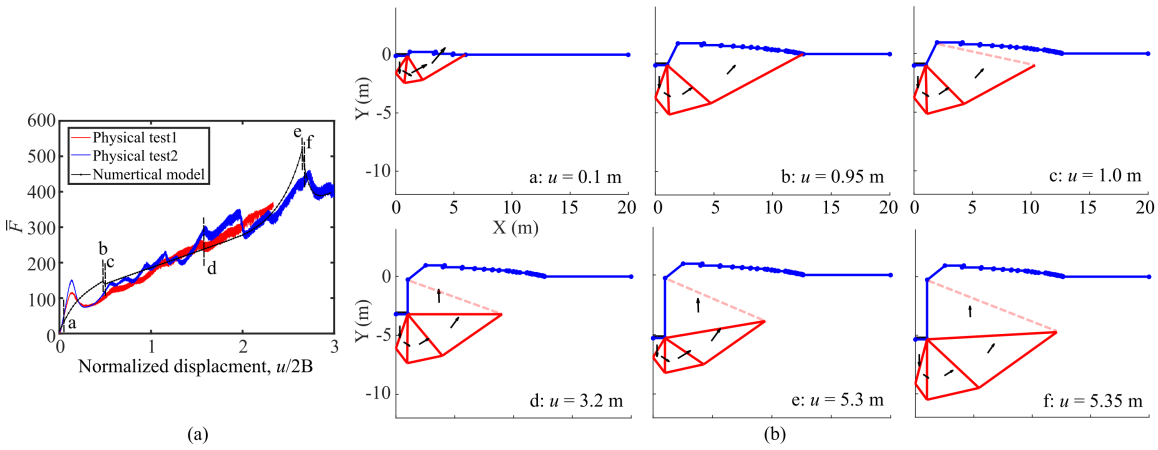


Figure 4.16. Results of penetration in sand (a) predicted and experimental normalized force-displacement history; (b) predicted evolution of velocity fields corresponding to points a-f in (a).

reflect a foundation problem rather than a problem in SMI. The penetration is processed by displacement control with $\Delta u = 0.05\,\text{m}$ $(0.05B)$.

Figure 4.16(a) shows the comparison of predicted and experimental normalized force-displacement histories. The deformation field for selected instances corresponding to the points in Figure 4.16(a) is given in Figure 4.16(b). In the simulation, the friction angle and dilation angle of sand are $\phi = 48°$ and $\psi = 18°$, respectively; the friction angle and dilation angle between the sand and plate are $\phi_i = 48°$ and $\psi_i = 2°$, respectively. These parameters are determined by matching the predicted force-displacement history with the experimental results. It is identified from the numerical results that the local peak (stage b-c and e-f) in force-displacement is related to the transition of shear localization (or deformation mechanism). Compared to the predictions with the experimental results, a general agreement is recognized. However, the model has deficiencies. For example, the optimization sometimes is infeasible even with using parameters that define reasonable soil properties.

## 4.5. Summary

This chapter constructs simplified theoretical models for predicting the soil responses during the process of biaxial compression, cutting, and penetration. The numerical formulations are presented, and their performance is evaluated by comparing against experimental observations. Overall, the SKM models can accurately predict soil responses, including both soil deformation and force-displacement histories, with efficient computational speed. Key findings from this study are summarized as follows:

(1) The progression of soil deformation under biaxial compression in loose and dense sand can be quantitatively predicted by the theoretical model. While the measured incremental deformations indicate that the shear band takes place close to the peak stress ratio, the SKM model implies it can appear much earlier and continuously form at same/different locations to shape the full observed evolution of soil deformation, i.e., soil deforms in a diffuse and non-homogeneous mode at first, followed by the appearance of a distinct shear band.

(2) For the cutting process, the SKM model can capture the distinct responses of loose and dense sand observed in experiments, including force-displacement histories and the evolution of soil deformation. More importantly, the SKM model identifies and explains sand's deformation mechanism in the cutting process: continuous discontinuity (localized deformation) propagates over regions. As it propagates, the sand on the localized region is hardening or softening, accompanying the compaction or dilation.

(3) For simulating the penetration process, an SKM model that incorporates a richer deformation mechanism is developed, which produces a prediction matching the experimental results as a whole. However, it is demonstrated that the model is to be improved in the aspects of prediction accuracy, generality, and stability. More specifically, the model

can incorporate the kinematics of sufficient complexity (e.g., using Extended Mohr-Coulomb Model [**189**]). To achieve the goal, one of the most critical tasks is to invent an effective method to estimate the energy dissipation rate within an increment, and ideally, the estimation should be purely stress-independent. Future efforts can be devoted to using a fictitious flow rule [**190**] or hyperplastic method [**191**].

CHAPTER 5

# Theoretical model: semi-analytical model for plate with translational movement

## 5.1. Introduction

The semi-analytical modeling framework is inspired by the generalized yield used in geotechnical engineering to analyze foundations and anchors subjected to combined loading [**192, 193, 194, 47, 195, 196, 197**]. The core concepts of the proposed model are described as follows. When a plate moves in the soil, the resistance consists of three components of force and moment: $H$, $V$, and $M$. The combinations of $H$, $V$, and $M$ that lead to a plate's movement are represented as a yield envelope, expressed through the yield function $f(H, V, M) = 0$. The displacement increments ($\Delta h$, $\Delta w$ and $\Delta\theta$, respectively) can be calculated based on a flow potential $P(H, V, M)$. Generally, the forces required to advance a plate through the soil will evolve due to geometric changes as well as hardening or softening of the soil. This can be accommodated by allowing the yield envelope $f$ to expand (hardening) or contract (softening) as a function of displacement. Ultimately, once the envelopes, flow potentials, and evolution rules are fully defined, calculation of force-displacement histories for particular load paths can be completed through simple numerical algorithms analogous to the 'stress integration' procedures used for constitutive models [**198, 199**].

This chapter focuses on developing a model that can predict the forces on a vertical plate as it moves in sand with arbitrarily large translational movement. The quantities related to the rotation (refer to $M$ and $\theta$) are neglected, so the envelope and flow potential will be

reduced from 3D to 2D. In other words, the model is constructed based on the assumption that the above concepts are also valid without $M$ and $\theta$. The model is demonstrated by first presenting a unified analysis of the experimental results reported in Chapter 3, which are used to define the important features in the model. The numerical modeling framework is then described, including the features, formulation, and implementation of the model. Finally, the model is validated by comparing the prediction against test results.

## 5.2. Analysis of experimental results: loading capacity of a vertical plate

### 5.2.1. Swipe test: normalized yield envelopes

The experimental result of the load paths in swipe tests (Figure 3.12) indicates that the yield envelope expands with increasing penetration depths. The two loads, $V$ and $H$, grow at different rates, where $H$ grows faster than $V$. Consider the results in dense sand as an example. The maximum $H$ increases considerably from 20 N to 120 N as the maximum compression $V$ expands from 80 N to 165 N. These yield envelopes are generalized by normalizing the load paths obtained in different experimental conditions, which depend on the relative densities of sand and the plate's penetration depths. An example is given in Figure 5.1 to illustrate the normalization method. The first step is to recognize the vertical tension bearing capacity ($V_{t0}$) and vertical compression bearing capacity ($V_{c0}$) from the original load path. These are the maximum value of $V$ in negative and positive axis, respectively. By horizontally shifting the original load path to the right with a distance of $V_{t0}$, the load path is plotted in the $V^*$-$H$ space, shown as Figure 5.1(b), where $V^* = V + V_{t0}$. From it, the horizontal bearing capacity ($H_0$) and the total vertical bearing capacity ($V_0$) can be obtained. Finally, the fully normalized load path is achieved by dividing the $V^*$ and $H$ by $V_0$ and $H_0$, respectively, as illustrated in Figure 5.1 (c).

Figure 5.2 presents the normalized versions of the yield envelopes appearing in Figure 3.12, where the dashed lines indicate the results of loose sand, and the solid lines represent the results of dense sand. Overall, the normalized yield envelopes are virtually identical, though some differences exist. For the yield envelopes generated in loose sand, the value of $V^*/V_0$ at the peak of $H/H_0$ is about 0.2 - 0.25, which is smaller than that in dense sand, i.e., 0.22 - 0.33. Comparing the yield envelopes obtained at different penetration depths, it is observed that the left portion of the yield envelope is generally steeper when the penetration depth is shallower. Another noticeable feature of Figure 5.2 is that for the cases of $D =$ 30 mm and 45 mm in dense sand, the swipe tests commencing from high $V$ (i.e., the right portion) reach steady-state of normalized horizontal load in the region of $V^*/V_0 = 0.22$ - 0.33 after producing a substantial increase in $H$.

Numerous equations have been proposed to fit the yield envelope in $V$-$H$ space for modeling the interaction between soil and structures (e.g. shallow footing, anchors, pile and pipe) [**155, 194, 107, 162, 200, 154, 195, 47, 193, 192, 201, 202, 203**]. As shown in Figure 5.2, the normalized yield envelopes obtained in this study are approximately parabolic and can be described by a form of 'parabola' with high flexibility

$$f = \left(\frac{H}{H_0}\right)^{\beta_1} - \beta_2 \left[\frac{V^*}{V_0} - \left(\frac{V^*}{V_0}\right)^{\beta_3}\right] \tag{5.1}$$

where $\beta_1$ controls the overall curvature of the 'parabola' and $\beta_3$ determines the vertical load level at which the peak horizontal load occurs. For these normalized yield envelopes, an

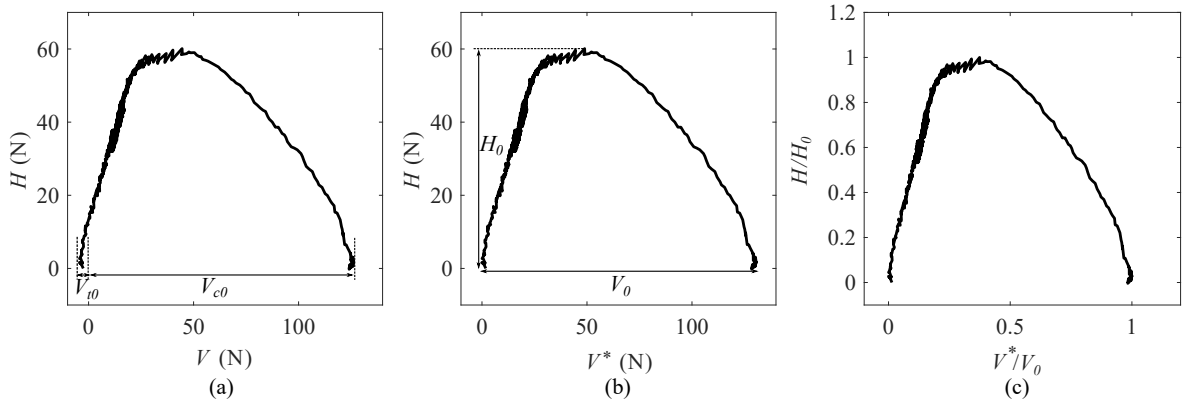


Figure 5.1. Method to normalize the load paths obtained in swipe tests: (a) original load path; (b) load path after translation; (c) load path in normalized space.

important hidden feature is that $H/H_0 = 1$ at the peak. To preserve the desired peak horizontal load, the parameter $\beta_2$ should be adjusted to $\beta_2 = \beta_3^{\beta_3/(\beta_3-1)}(\beta_3 - 1)^{-1}$. Substituting this function of $\beta_2$ into Equation 5.1 gives

$$f = \left(\frac{H}{H_0}\right)^{\beta_1} - \frac{\beta_3^{\beta_3/(\beta_3-1)}}{\beta_3 - 1}\left[\frac{V^*}{V_0} - \left(\frac{V^*}{V_0}\right)^{\beta_3}\right] \tag{5.2}$$

With this expression, $\beta_1$ and $\beta_3$ can be varied to adjust the curvature of the fitting curve and shift the peak to any desired normalized vertical load ($0 < V^*/V_0 < 1$), while maintaining the maximum normalized horizontal load equal to 1.

### 5.2.2. Displacement probe test: flow rule

The associated flow rule is commonly used in the semi-analytical models for clay under various applications, which has been verified by experiments and numerical analysis. However, the behavior of a plate in sand does not obey an associated flow rule. Direct evidence can be found in the swipe tests in dense sand (Figure 3.12(a)). As the yield envelopes produced by

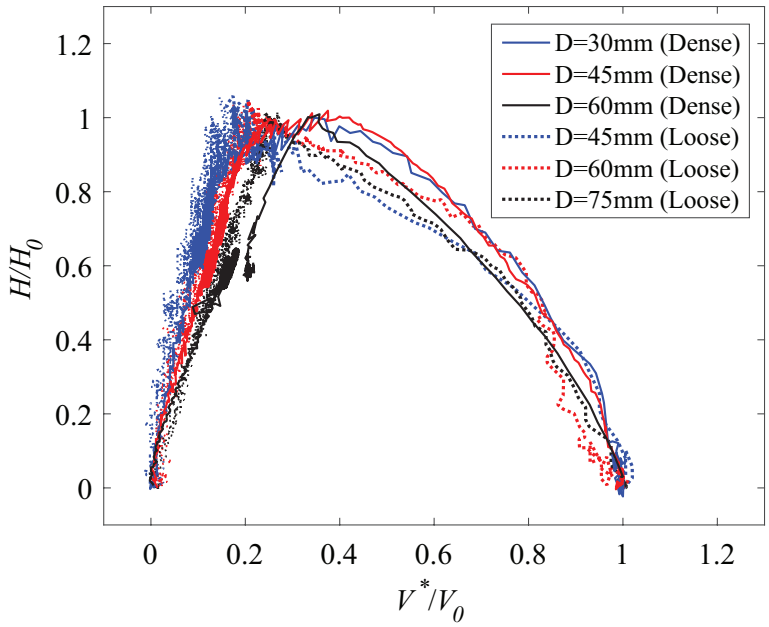


Figure 5.2. Yield envelopes in normalized space.

the test commencing from high $V$ do not terminate at the peak of the envelope but exceed the peak, the two load paths intersect at a position where $V/V_{c0}$ is lower than that at the peak. At the intersection point, the direction of incremental displacement should be purely horizontal, i.e., $\Delta w = 0$, which clearly contrasts with the yield envelope's behavior on the left side of the peak where its normal vector has a component of $\Delta w$.

To more explicitly study the flow rule, the results of displacement probe tests are analyzed. Figure 5.3 illustrates the directions of incremental plastic displacement ($\Delta \mathbf{u}^p$) on the yield envelope for three cases, where the yield envelopes are generated by fitting the experimental data from swipe tests and displacement probe tests to Equation 5.6. It should be noted that since the ratio of vertical displacement $w$ and horizontal displacement $u$ is constant throughout a probe test, the two components of elastic displacement are at the

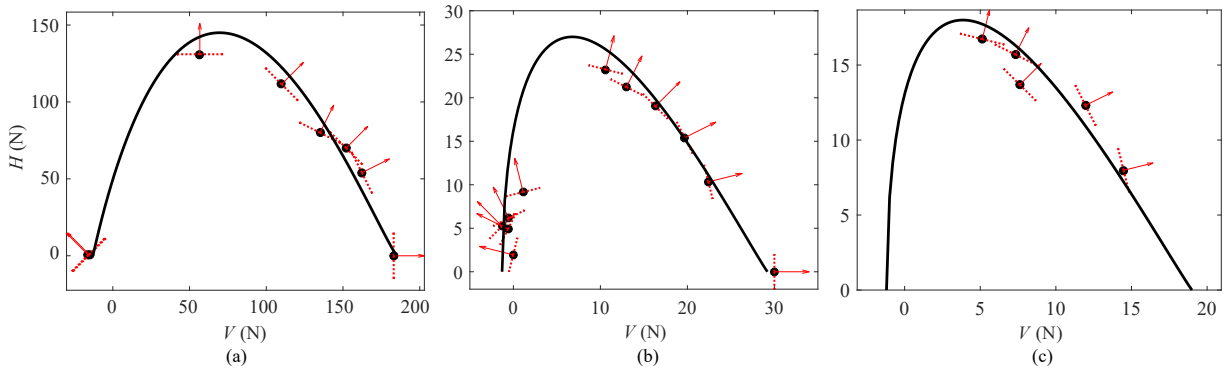


Figure 5.3. Directions of the incremental displacement (red rows) on yield envelope (black lines) for three cases: (a) $D = 60$ mm in dense sand; (b) $D = 60$ mm in loose sand; (c) $D = 45$ mm in loose sand.

same ratio at the yield point, which suggests that the direction of the incremental plastic displacement is identical to that of the incremental displacement. The figure identifies that at high $V$ ($V/V_{c0} > 0.6$), the angle of the $\Delta\mathbf{u}^p$ with the horizontal is typically smaller than that between the normal vector of the envelope and the horizontal; at relatively lower $V$ ($0.3 < V/V_{c0} < 0.6$), the angle of the $\Delta\mathbf{u}^p$ with the horizontal is larger. This provides a direct evidence that the plastic flow is not associated with the yield envelopes.

Based on all above analysis, the features that a flow rule should be able to capture include: (1) the incremental plastic displacement vector should be purely vertical ($\Delta u^p = 0$) at $V = V_{c0}$ where $H/V = 0$; (2) the incremental plastic displacement vector should be purely horizontal ($\Delta w^p = 0$) at the intersection of a pair of load paths composing a yield envelope, where the force ratios ($H/V$) are found to be approximately same for different cases in loose sand and in dense sand, respectively (refer to Section 3.3.4); (3) $\Delta u^p/\Delta w^p$ (reflecting the direction of the incremental plastic displacement) should be able to change from 0 to infinity quickly. With these basic properties of the flow rule, the ratios of incremental displacement components versus the force ratio at the yield points for three different yield envelopes are

plotted, as illustrated in Figure 5.4(a). By tentatively fitting these data, it is found that the relationship can be described by:

$$\frac{\mathrm{d}u_p}{\mathrm{d}w_p} = \frac{\partial P/\partial H}{\partial P/\partial V} = \alpha_1 \tan\left[\frac{\pi}{2}\left(\frac{H}{V}\alpha_2\right)^{\alpha_3}\right] \tag{5.3}$$

where $\alpha_1$ and $\alpha_3$ control the shape of the curve; $\alpha_2$ determines the position of the vertical asymptote. The parameter $\alpha_2$ equals the force ratio at the intersection point of yield envelope $(H_I/V_I)$. As described in Section 3.3.4, the value is observed to be a constant for loose and dense sand, respectively. This equation can be characterized more fully with the following theoretical analysis. As the plate is pushed further horizontally after the intersection point, the vertical force on the plate is generated from the friction between soil and plate. From Figure 3.9 and 3.10, the force ratios $(H/V)$ are demonstrated to be approximately the same at and after the intersection point. Therefore, it can be inferred that $\alpha_2 = H_I/V_I = 1/\tan\phi_w$, where $\phi_w$ is the friction angle between sand and plate. Additionally, it is found that the experimental data can be better described by Equation 5.3 by setting $\alpha_3 = 1.5$, which is indicated by the linear relationship between the incremental displacement ratios and $g(H/V)$ shown in Figure 5.4(b). According to the above analysis, Equation 5.3 is reformed to express the relationship between incremental displacement ratio and force ratio:

$$\frac{\mathrm{d}u_p}{\mathrm{d}w_p} = \frac{\partial P/\partial H}{\partial P/\partial V} = \alpha_1 \tan\left[\frac{\pi}{2}\left(\frac{H}{V\tan\phi_w}\right)^{1.5}\right] \tag{5.4}$$

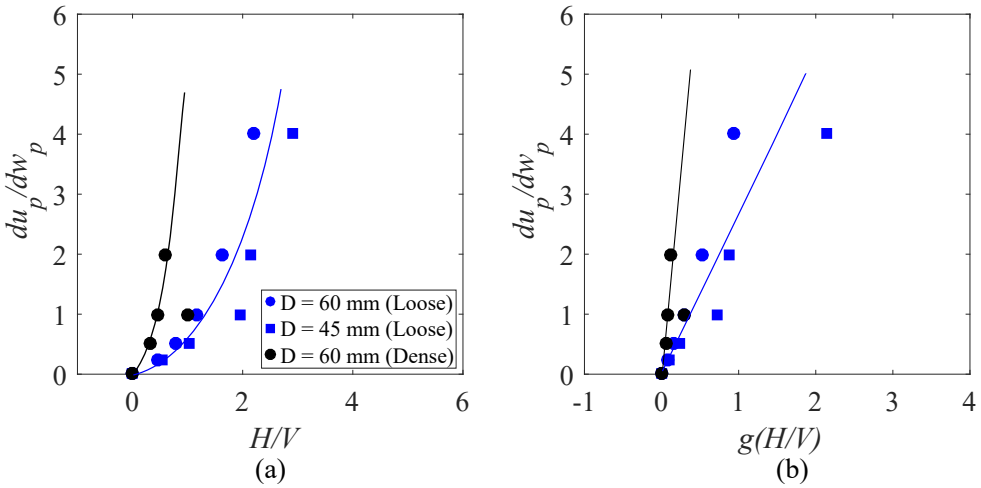


Figure 5.4. Incremental displacement ratio versus (a) the force ratio on three yield envelopes; (b) a function of force ratio, where $g = \tan\left[\frac{\pi}{2}\left(\frac{H}{V\tan\phi_w}\right)^{1.5}\right]$.

In this equation, $\alpha_1$ determines the slope of the line shown in Figure 5.4(b) and is associated with soil properties. It should be noted that these lines are plotted to show schematically the behavior of the equation. The selection and determination of the parameters in the equation will be discussed in Section 5.3.1.3.

### 5.2.3. Penetration test: normalized loading curves

A preliminary analysis of the penetration test has been undertaken in Chapter 3 (Section 3.3.2; Figures 3.7-3.8). A dimensionless form of normalized penetration resistance $q/(\gamma B)$ versus normalized vertical displacement $w/B$ is presented in Figure 5.5, where $q$ is defined by $V/(BL)$; $B$ and $L$ are the width and length of the plate, respectively. The penetration resistance consists of tip resistance and side resistance resulting from friction between the plate and sand. The figure indicates that at $w/B = 20$, the normalized penetration resistance is about 4000 for dense sand and 850 for loose sand. This would imply a friction angle of about 41° and 33°, respectively, by using the analytical solution proposed by

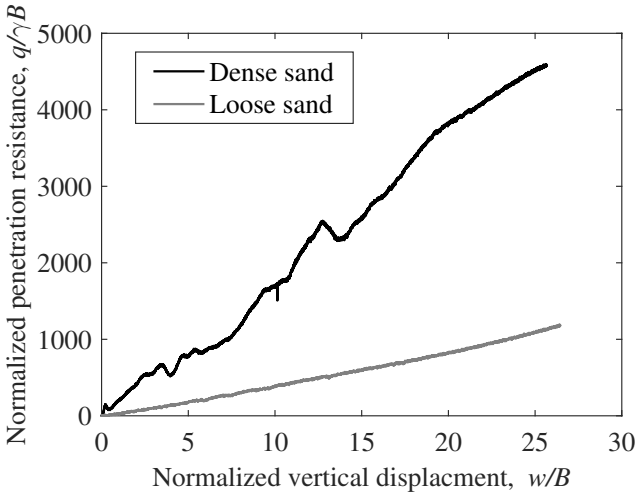


Figure 5.5. Normalized penetration resistance with normalized vertical displacement.

Table 5.1. Measured elastic stiffness of a plate system at different relative depths

| Relative depth, $D/B$ | $K_v$ (kN/m) | | $K_h$ (kN/m) | |
|---|---|---|---|---|
| | Dense | Loose | Dense | Loose |
| 0 | 17,778 | 556 | | |
| 5 | 94,444 | | 22,222 | |
| 10 | 75,556 | | 38,889 | 23,333 |
| 15 | 112,222 | | 50,000 | 36,667 |
| 20 | 170,000 | 17,778 | | 45,442 |

Durgunoglu and Mitchell [**204**] without carefully considering the influence of friction between the soil and plate. These properties are reasonable for the sand used in the tests. By fitting the elastic part of the loading curves with straight lines, the vertical elastic stiffnesses ($K_v$ in V = $K_v w_e$, where $w_e$ is the elastic vertical displacement) at different relative depth are evaluated, as listed in Table 5.1. It is noted that the values are normalized by the width and length of the plate. A more in-depth discussion about the elastic response will be presented in Section 5.3.1.1.

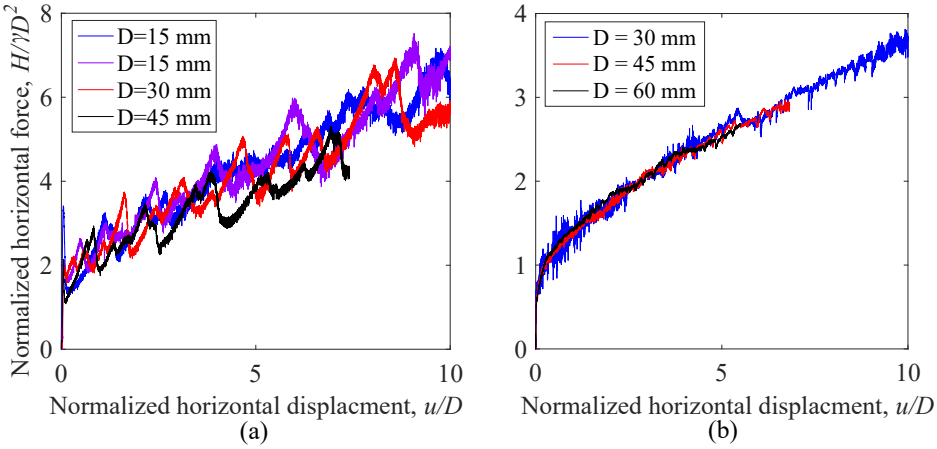


Figure 5.6. Normalized cutting resistance with the normalized horizontal displacement.

### 5.2.4. Cutting test: normalized loading curves

The preliminary analysis on the evolution of horizontal force with displacement is performed in Section 3.3.3. Figure 5.6 illustrates the normalized force-displacement curves corresponding to the plots in Figure 3.9(a) and 3.10(a). The normalization is implemented using the method described in the previous study on modeling the cutting process in soils [**11**]. The figure indicates that the relationships between the normalized cutting resistance and the relative horizontal displacement at various cutting depths are almost identical, holding for sand at both loose and dense states. In addition, by fitting the elastic part of the force-displacement curves with a straight line, the horizontal elastic stiffnesses ($K_h$ in $H = K_h u_e$) at different relative depth are evaluated, as listed in Table 5.1.

## 5.3. Numerical modeling

This section describes the formulation of the semi-analytical model based on strain-hardening plasticity for predicting the load-displacement response of a plate moving in sand translationally. The principal concepts adopted in the model are summarized as follows. At

any condition of a plate moving in soil, a yield envelope in ($V$, $H$) space will be established. Any changes of load within this envelope will only result in elastic deformation. The elastic behavior is linear, specified by a set of elastic constants. Load points touching the yield envelope can result in plastic deformation, which is determined by using the non-associated flow rule. The size ($V_0^*$, $H_0$) of this yield envelope varies as the object is pushed into the soil or moved horizontally further, and the hardening law is specified by a relationship between the size of the yield envelope and the plastic vertical and horizontal displacements. This relationship is established based on analytical solutions.

### 5.3.1. Features of model

**5.3.1.1. Elastic response.** The elastic relationship between the load increments (d$V$, d$H$) and the corresponding elastic displacements (d$w_e$, d$u_e$) is

$$\begin{bmatrix} \mathrm{d}V \\ \mathrm{d}H \end{bmatrix} = 2B \begin{bmatrix} k_v & 0 \\ 0 & k_h \end{bmatrix} \begin{bmatrix} \mathrm{d}w_e \\ \mathrm{d}u_e \end{bmatrix} \tag{5.5}$$

where $B$ is the half-width of the plate; $k_v$ and $k_h$ are the elastic stiffness factors in vertical and horizontal direction of the plate system. Their values mainly depend on the relative density of sand and the relative depth of the plate, which has been suggested in previous studies [**116, 205, 155, 206**]. Based on the experimental measurements of the elastic stiffnesses at different relative depths (listed in Table 5.1), $k_v$ and $k_h$ (unit: kN/m$^2$) are determined as: $k_v/(\gamma B) = 600 + 130D/B$, $k_h/(\gamma B) = 180 + 60D/B$ for dense sand; $k_v/(\gamma B) = 13 + 20D/B$,

$k_h/(\gamma B) = 40 + 50D/B$ for loose sand. Here the depth $D$ refers to the plastic vertical displacement $w_p$, which means that the elastic stiffness factors are a function of $w_p$ not of total vertical displacement.

**5.3.1.2. Generalized yield envelope.** In Section 5.2.1, it was found that the experimental yield envelopes can be described by the form:

$$f = \left(\frac{H}{H_0}\right)^{\beta_1} - \beta_2 \left[\frac{V^*}{V_0} - \left(\frac{V^*}{V_0}\right)^{\beta_3}\right] \tag{5.6}$$

where $V_0$ is the total vertical loading capacity under purely vertical loading; $H_0$ is the horizontal loading capacity under purely horizontal loading. Inside the yield envelope $f < 0$, the behavior is elastic and governed by Equation 5.5. For points $(V, H)$ lying on the yield envelope, $f = 0$, and the plate behavior is elastoplastic. By using least-squares method to fit the yield envelopes obtained from swipe tests, best-fit parameter values are derived for a plate in sand: $\beta_1 = 0.885$, $\beta_3 = 1.005$. The fitting performance is illustrated in Figure 5.7, indicating that the fitting curve can represent the experimental yield envelopes satisfactorily. Despite the well-fitted result, one may notice that the value of $V^*/V_0$ at the peak of $H/H_0$ for the yield envelopes generated in loose sand is slightly smaller than that in dense sand, which has been mentioned in Section 5.2.1. To capture the discrepancy of the fit associated with soil density, Equation 5.6 can be further developed by relating $\beta_3$ with a parameter characterizing soil density (such as friction angle). The development requires the yield envelopes generated from either numerical or physical tests in sand at various densities. However, this is out of the scope of this study and can be regarded as future work.

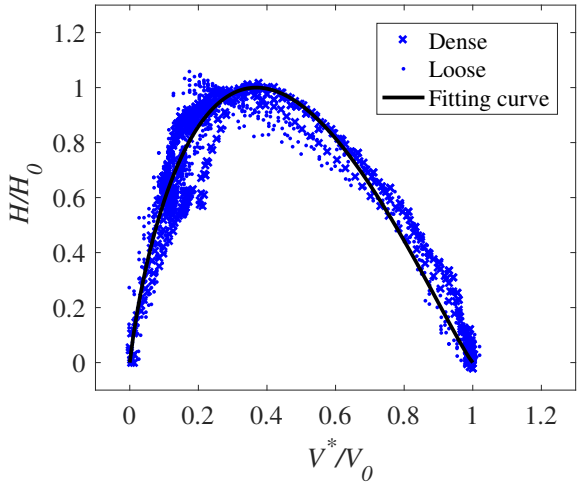


Figure 5.7. Fitting yield envelope with Equation 5.6.

**5.3.1.3. Flow rule.** As discussed in Section 5.2.2, a non-associated flow rule is more reasonable to define the incremental plastic displacements, and their ratio can be described by:

$$\frac{du_p}{dw_p} = \frac{\partial P/\partial H}{\partial P/\partial V} = \alpha_1 \tan\left[\frac{\pi}{2}\left(\frac{H\tan\phi_w}{V}\right)^{1.5}\right] \tag{5.7}$$

where $\phi_w$ is the friction angle between soil and plate, determined by measuring the slope of the dashed line in Figure 3.12. For the plate in dense sand, $\phi_w = \text{atan}(1/2.7) = 20.3°$; for the plate in loose sand, $\phi_w = \text{atan}(1/3.6) = 15.5°$. The parameter $\alpha_1$ is derived by using least-squares method to fit the data in Figure 5.4(b): $\alpha_1 = 3.8$ for dense sand and 2.1 for loose sand. The friction angle of dense and loose sand is evaluated to be 40° and 31°, respectively (the evaluation process will be presented in Section 5.3.1.4). In this study, it is assumed that the parameter $\alpha_1$ is associated with soil properties exclusively. Because the friction angle is

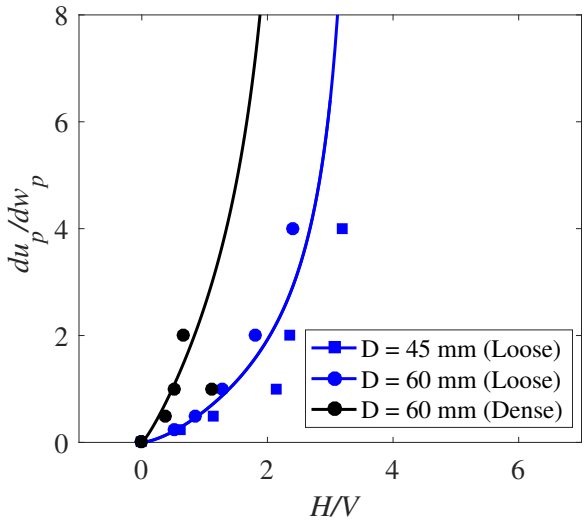


Figure 5.8. Incremental displacement ratio versus the force ratio on three yield envelopes fitted with Equation 5.8.

the only parameter, $\alpha_1$ can be determined as $\alpha \tan^2 \phi$. Accordingly, Equation 5.7 is modified to

$$\frac{du_p}{dw_p} = \frac{\partial P/\partial H}{\partial P/\partial V} = \alpha \tan^2 \phi \tan \left[ \frac{\pi}{2} \left( \frac{H \tan \phi_w}{V} \right)^{1.5} \right] \tag{5.8}$$

where $\alpha$ is determined as 7.1 using the least-squares method. The fitting performance of the equation is demonstrated in Figure 5.8, indicating that the proposed equation can match experimental data fairly well. It is important to note that $\alpha_1$ may also vary with penetration depth $D$, given that the behaviors for tests in loose sand at $D$ = 45 mm and 60 mm (illustrated in Figure 5.8) are slightly different. However, for the sake of simplicity, the association between $\alpha_1$ and $D$ is not investigated in this study, which can be regarded as future work.

It is acknowledged that a rigorous plasticity model would require a definition of a plastic potential function $P$, which was not given in this study. However, for developing the model, it is convenient to define the flow rule based on the ratio without deriving the explicit expression of $P$:

$$\begin{bmatrix} \mathrm{d}u_p \\ \mathrm{d}w_p \end{bmatrix} = \lambda \begin{bmatrix} \alpha \tan^2\phi \tan\left[\frac{\pi}{2}\left(\frac{H\tan\phi_w}{V}\right)^{1.5}\right] \\ 1 \end{bmatrix} \tag{5.9}$$

**5.3.1.4. Hardening law.** The size of the non-normalized $V-H$ yield envelope is controlled by the maximum vertical and horizontal load capacity, and their values are determined based on the analytical solutions.

As defined in Section 5.2.1, the vertical loading capacity is composed of tension bearing capacity $V_{t0}$ and compression bearing capacity $V_{c0}$. The former is estimated as the friction between soil and plate, i.e, $V_{t0} = \tan\phi_w \gamma D^2 K_0$ with $K_0 = 1 - \sin\phi$ (coefficient of lateral earth pressure). On the premise of ignoring the local hardening and softening shown in dense sand, $V_{c0}$ is determined by applying the analytical solution proposed by Durgunoglu and Mitchell [**204**]. Its main concepts are briefly summarized here. The analytical solution is a plane strain solution, which is developed by using the limit equilibrium method based on the failure mechanism observed from model tests. During the wedge penetration process, a plane shear zone exists adjacent to the base of the penetrometer. The dimensions of this zone depend on the interface friction angle $\phi_w$ and soil friction angle $\phi$. A logarithmic spiral bounds a radial shear zone to the point of vertical tangency, above which the yield envelope rises vertically to the ground surface for large-depth penetration. For shallow penetration depths, the spiral breaks out at the ground surface before vertical tangency is reached. Based on the failure mechanism, the penetration resistance is calculated by

solving the moment equilibrium about the base edge of the penetrometer. Adopting this method, $V_{c0}$ can be written as $V_{c0} = V_{c0}(D/B, \phi, \phi_w, \gamma)$. The complete expression of the equation is not presented here, and readers are referred to the original work [**204**]. As indicated in Figure 3.9(b) and 3.10(b) (Section 3.3.3), the vertical forces increase with the horizontal forces linearly, and the force ratios are constant during the horizontal cutting process. The force ratio $H/V$ is analyzed to be equal to $1/\tan\phi_w$ (Section 5.2.2). Therefore, the development of horizontal loading capacity has a contribution on the vertical loading capacity, i.e., $\Delta V_{c0} = \Delta H_0 \tan\phi_w$. With all the above analysis, the total vertical loading capacity can be expressed as:

$$V_{c0} = V_{c0}(D/B, u, \phi, \phi_w, \gamma). \tag{5.10}$$

The method to calculate the horizontal loading capacity is developed based on an analytical model for the cutting process proposed by Hambleton [**11**], which is depicted in Figure 5.9(a). The model rests on three key assumptions: (1) all deformation occurs along a single, straight slip surface that extends from the tip of the plate towards the soil surface at some unknown inclination angle $\beta$; (2) the unknown free surface is approximated by a straight line; (3) potential volume change within the material is neglected. Over the soil-plate interface, Coulomb friction is assumed, and the wall friction angle is denoted by $\phi_w$. The Mohr-Coulomb yield criterion with an internal friction angle of $\phi$ is applied to the soil. Based on the yield condition and equilibrium, the force $H_0$ required to displace the plate can

be derived and expressed as

$$H_0 = W\frac{\tan(\beta+\phi)}{1-\tan\phi_w\tan(\beta+\phi)}. \tag{5.11}$$

where $W$ is the weight of soil above the slip surface. Instead of using the original equation in the previous study [**11**] to calculate $W$, here it is estimated as

$$W = \gamma D^2/(2\tan\beta) + \gamma u D. \tag{5.12}$$

In Equation 5.11 and 5.12, the only unknown is $\beta$. Based on the principal of minimum effort, $\beta$ is evaluated by minimizing $H$, which is readily obtained by solving $\partial H/\partial\beta = 0$

$$\tan\beta_{opt} = \frac{D\sin\phi\,(\tan\phi_w\cos\phi - sin\phi) + \sqrt{\cos\phi(D\tan\phi_w + 2u) + \sin(D - 2u\tan\phi_w)}}{D\cos\phi(\cos\phi\tan\phi_w + \sin\phi) + 2u} \tag{5.13}$$

By taking $\beta = \beta_{opt}$ into Equation 5.11, the force $H_0$ can be obtained

$$H_0 = H_0(D, u, \phi, \phi_w, \gamma). \tag{5.14}$$

It is important to note that, as with the elastic stiffness factors $k_v$ and $k_h$, the penetration depth $D$ and cutting displacement $u$ in Equation 5.14 and 5.10 refer to the plastic vertical and horizontal displacement ($w_p$ and $u_p$) but not the total displacement. This ensures that purely elastic load increments do not result in expansion or contraction of the yield envelope.

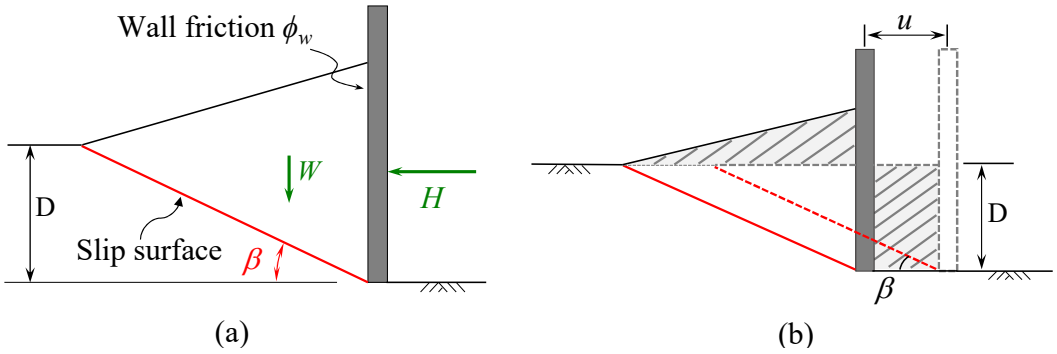


Figure 5.9. Analytical model for cutting in dry sand: (a) assumed mode of deformation and (b) change of soil weight above slip surface corresponding to the plate displacement $u$.

Figures 5.10 and 5.11 present the comparison between experimental and estimated normalized loading curves for tests in dense and loose sand, respectively. In the computations, the parameters are estimated as $\phi_w = 20.3°$ and $\phi = 38.5°$ for dense sand; $\phi_w = 15.5°$ and $\phi = 30.7°$ for loose sand. These values of $\phi_w$ are determined as described in Section 5.3.1.3, and the values of $\phi$ are estimated by simultaneously matching the calculated vertical and horizontal force-displacement histories to the measured curves.

### 5.3.2. Mathematical formulation

With the defined features of elastic response, yield envelope, flow rule, and hardening rule, the elastoplastic force-displacement matrix can be derived. As a loading increment is purely elastic, the incremental force vector d$\mathbf{F}$ is related to incremental displacement vector d$\mathbf{u}$ with the relationship illustrated in Equation 5.5.

When the stress state is on the yield envelope ($f(\mathbf{F}, V_0, H_0) = 0$) and the incremental loading causes plasticity, the force point remains on the yield envelope to satisfy the

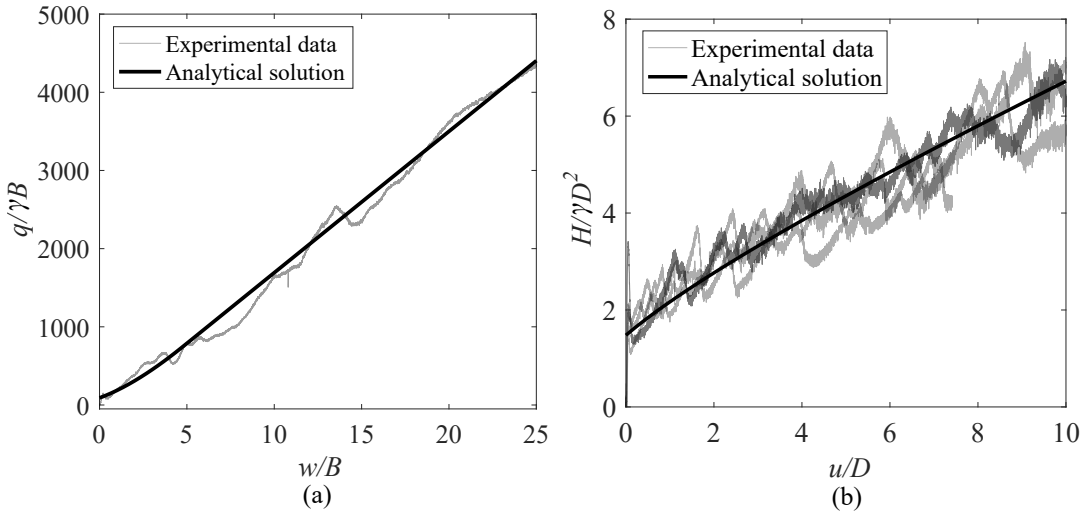


Figure 5.10. Estimated and experimental force-displacement histories for (a) penetration tests; (b) cutting tests in dense sand.

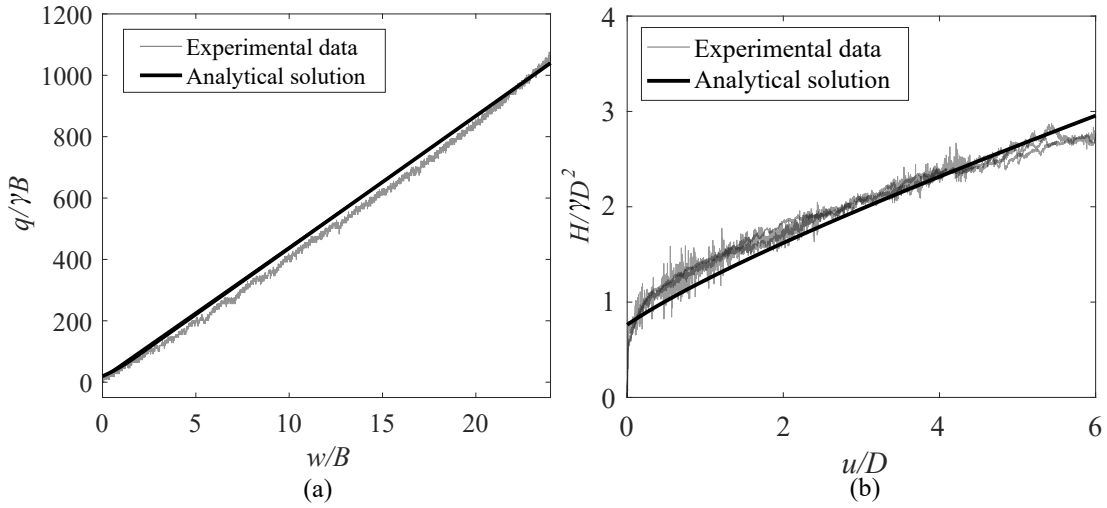


Figure 5.11. Estimated and experimental force-displacement histories for (a) penetration tests; (b) cutting tests in loose sand.

consistency condition

$$df = \frac{\partial f}{\partial \mathbf{F}} d\mathbf{F} + \frac{\partial f}{\partial V_0} dV_0 + \frac{\partial f}{\partial H_0} dH_0 = 0 \tag{5.15}$$

In the equation, the incremental force can be expressed as

$$d\mathbf{F} = \mathbf{D_e}(d\mathbf{u} - d\mathbf{u_p}) \tag{5.16}$$

where $D_e$ is the elastic stiffness, and its expression is shown in Equation 5.5. The hardening rules are

$$dV_0 = \left(\frac{\partial V_0}{\partial \mathbf{u_p}}\right)^T d\mathbf{u_p} = \frac{\partial V_0}{\partial w_p} dw_p, \quad dH_0 = \left(\frac{\partial H_0}{\partial \mathbf{u_p}}\right)^T d\mathbf{u_p} = \frac{\partial H_0}{\partial w_p} dw_p + \frac{\partial H_0}{\partial u_p} du_p \tag{5.17}$$

By taking Equations 5.16, 5.17 and the flow rule ($\mathrm{d}\mathbf{u_p} = \lambda \frac{\partial P}{\partial \mathbf{F}}$) into Equation 5.15, the consistency condition becomes

$$df = \left(\frac{\partial f}{\partial \mathbf{F}}\right)^T \mathbf{D_e} d\mathbf{u} - \lambda \left(\frac{\partial f}{\partial \mathbf{F}}\right)^T \mathbf{D_e} \frac{\partial P}{\partial \mathbf{F}} + \lambda \frac{\partial f}{\partial V_0} \left(\frac{\partial V_0}{\partial \mathbf{u_p}}\right)^T \frac{\partial P}{\partial \mathbf{F}} + \lambda \frac{\partial f}{\partial H_0} \left(\frac{\partial H_0}{\partial \mathbf{u_p}}\right)^T \frac{\partial P}{\partial \mathbf{F}} \tag{5.18}$$

Thus, the plastic multiplier $\lambda$ can be calculated as a function of the imposed incremental displacement

$$\begin{aligned} &\lambda = \frac{(\partial f/\partial \mathbf{F})^T \mathbf{D_e} \mathrm{d}\mathbf{u}}{H_c - H_a}, \\ &\text{with} \quad H_c = \left(\frac{\partial f}{\partial \mathbf{F}}\right)^T \mathbf{D_e} \frac{\partial P}{\partial \mathbf{F}}, \quad H_a = \frac{\partial f}{\partial V_0} \left(\frac{\partial V_0}{\partial \mathbf{u_p}}\right)^T \frac{\partial P}{\partial \mathbf{F}} + \frac{\partial f}{\partial H_0} \left(\frac{\partial H_0}{\partial \mathbf{u_p}}\right)^T \frac{\partial P}{\partial \mathbf{F}} \end{aligned} \tag{5.19}$$

The standard tangent modulus can be obtained by substituting Equation 5.19 back into Equation 5.16

$$d\mathbf{F} = \mathbf{D_{ep}} d\mathbf{u}, \quad \text{with} \quad \mathbf{D_{ep}} = \mathbf{D_e} - \frac{H_c}{H_c - H_a} \mathbf{D_e}. \tag{5.20}$$

Table 5.2. Parameters used in model

| **Parameters** | **Explanation** |
|---|---|
| $B$ (m) | Width of the object |
| $\gamma$ (N/m$^3$) | Unit weight of sand |
| $\phi$ | Friction angle of sand |
| $\phi_w$ | Sand-plate interface friction angle |
| $k_v$ | Elastic stiffness factor in vertical direction |
| $k_h$ | Elastic stiffness factor in horizontal direction |
| $\beta_1, \beta_3$ | Curvature factors for yield envelope |
| $\alpha_i (i = 1, 2, 3)$ | Factors for flow rule |

### 5.3.3. Implementation

The semi-analytical model is implemented by using displacement control, which allows the calculation of force-displacement history in the loading condition that the plate moves with prescribed displacement/motion. The procedure is described as follows:

(1) The input data is initialized, which includes model parameters, initial conditions, and magnitude of applied displacement paths. The required model parameters in this model are summarized in Table 5.2. The initial condition refers to the force $\mathbf{F}$, displacement $\mathbf{u}$ and loading capacities $V_0$, $H_0$ at the start of the loading process. The applied displacement paths are described by giving the vertical and horizontal displacement and the corresponding number of steps for each path.

(2) For the $n^{th}$ displacement increment $\Delta\mathbf{u}_{n+1}$, the updated force is initially assumed to be elastic. Therefore, $\mathbf{F}^T_{n+1} = \mathbf{F}_n + \mathbf{D}_e(\mathbf{u^p}_n)\Delta\mathbf{u}_{n+1}$, where the superscript 'T' stands for a trial state and subscript denotes the process step. In a certain step, the plastic displacement is preserved as the previous values, $\mathbf{u^p}_{n+1} = \mathbf{u^p}_n$. Thus, the elastic stiffness and loading capacities are fixed, with values determined by $\mathbf{u^p}_n$, i.e., $\mathbf{D}_e(\mathbf{u^p}_n)$, $V_0(\mathbf{u^p}_n)$ and $H_0(\mathbf{u^p}_n)$. If $f(\mathbf{F}^T_{n+1}, V_0, H_0) < 0$, the process at step $n+1$ is considered elastic.

(3) If the above yield condition is violated for the trial state, the force state surpasses the yield envelope. In this case, provided that yielding does not occur in the previous step, the intersection of force path and yield envelope is found by using the Bisection method, where the force is recorded as $\mathbf{F_m}$. The portion of the load path inside the yield envelope is evaluated by defining a quantity of $\kappa = |\mathbf{F_m} - \mathbf{F}|/|\mathbf{F}|$. Then, the force and displacement increments are calculated as $\kappa \mathbf{D}_e \Delta \mathbf{u}_{n+1}$ and $\kappa \Delta \mathbf{u}_{n+1}$. After the updates, the force state is now on the yield envelope. Based on the mathematical formulation in the previous section, the elastoplastic stiffness matrix can be calculated. Accordingly, force increments are computed and updated.

(4) Steps (2)-(3) are repeated until the entire force-displacement history is obtained.

## 5.4. Model validation

Computational results have been obtained in various loading conditions by using the developed model. To demonstrate model performance, results for three different plate trajectories are presented, where Figure 5.12 shows the specified trajectories. For Case 1, the plate penetrates into sand for 30 mm first and then moves in the direction with $w/u = 2$. After that, it cuts the sand purely horizontally for 30 mm. For Cases 2 and 3, the first and last paths are the same as those in Case 1, but the directions of the second path are different: the ratio of $w$ to $u$ is 1 in Case 2 and 1/2 in Case 3.

### 5.4.1. Predictions in dense sand

Figure 5.13-5.15 compare the computed results and experimental data of tests in dense sand. Overall, the model can capture the characteristics of the force-displacement history in the process, reflected by clearly showing the turning points at the junctions of paths. However, deficiencies do exist. The major one is that the local hardening and softening in forces cannot

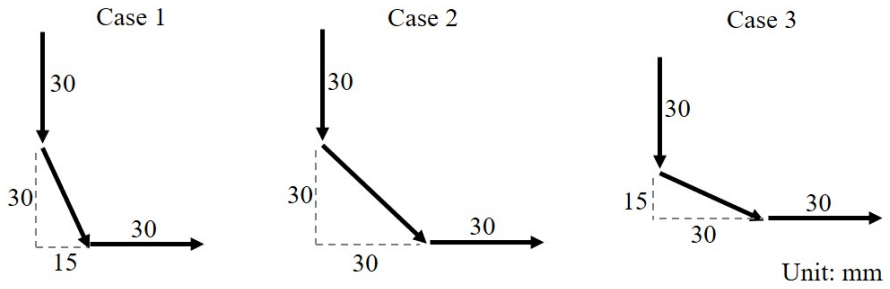


Figure 5.12. Trajectories of plate for case studies

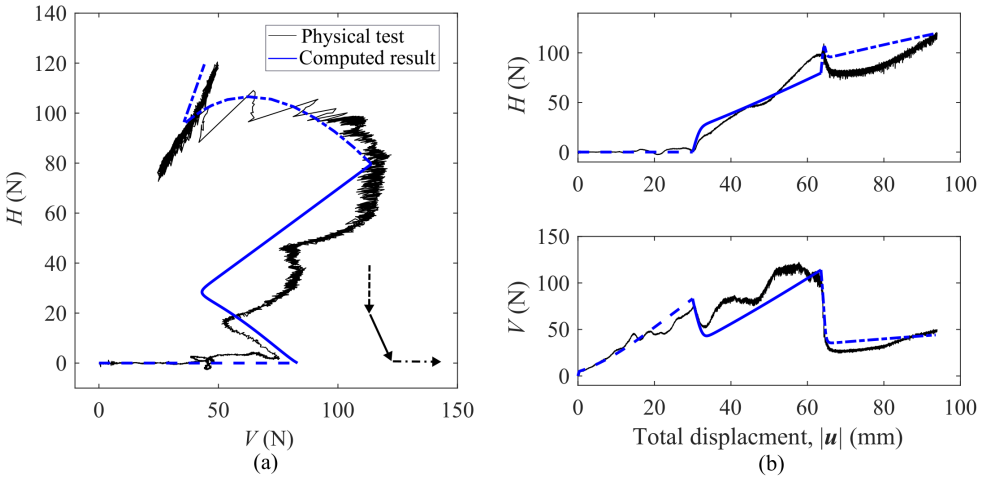


Figure 5.13. Comparison of experimental and computed results for Case 1 in dense sand, where the three line types are used to depict the result of three paths individually.

be predicted, which is indicated explicitly by the results of the second path. Additionally, for the soil responses in path 2 and 3, the vertical force decreases first and then increases, and the point at the transition is not predicted precisely.

### 5.4.2. Predictions in loose sand

The comparisons between the computed results and experimental data for tests in loose sand are shown in Figure 5.16-5.18. It is observed that the computed result matches the

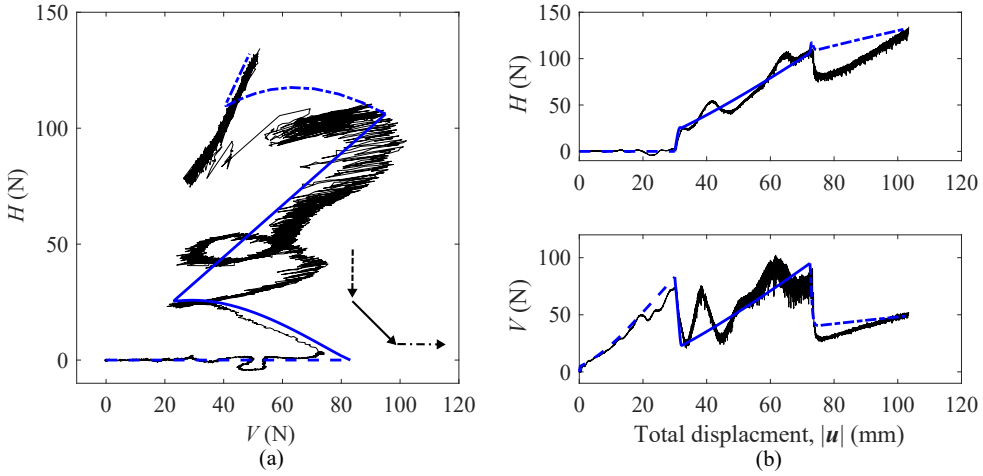


Figure 5.14. Comparison of experimental and computed results for Case 2 in dense sand.

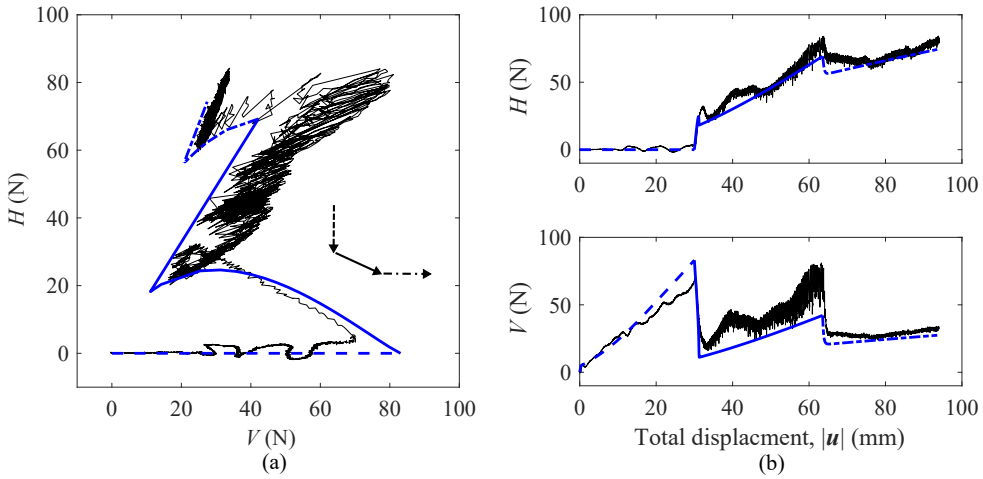


Figure 5.15. Comparison of experimental and computed results for Case 3 in dense sand.

experimental curve well. Since the forces generally evolve without local fluctuations for a plate moving loose sand, the model's major deficiency in predicting the local hardening and softening is not shown. Despite the excellent agreement, one may notice the mismatch between the prediction and physical test data for the second path of Case 1. This mismatch might be reduced by improving the flow rule.

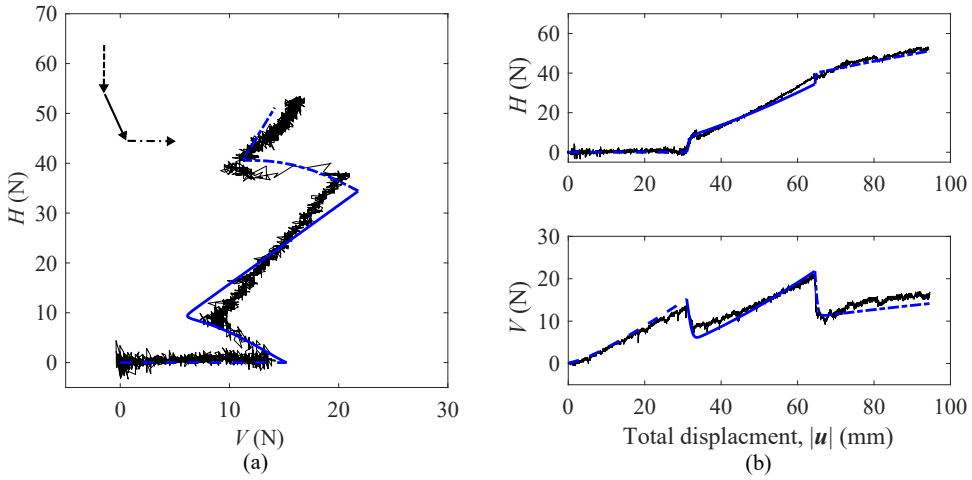


Figure 5.16. Comparison of experimental and computed results for Case 1 in loose sand.

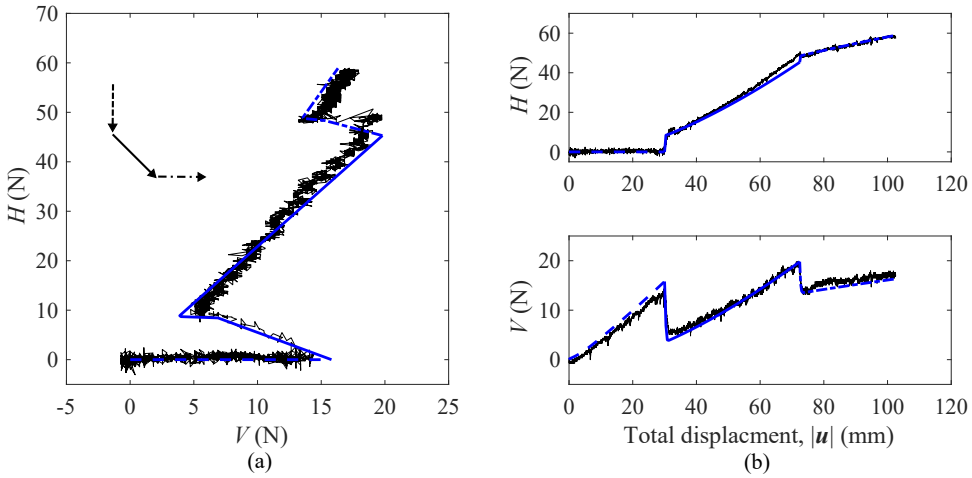


Figure 5.17. Comparison of experimental and computed results for Case 2 in loose sand.

## 5.5. Summary

This chapter presents a semi-analytical model for predicting the force-displacement response as a plate performs large translational movements in sand. The model is developed by first completing a unified analysis of experimental results. The model is implemented with displacement control, generating the force-displacement histories for a plate moving

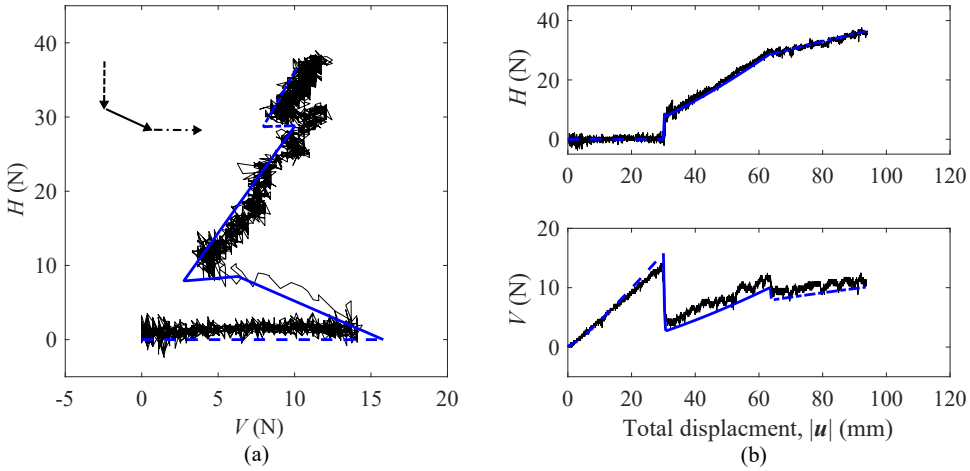


Figure 5.18. Comparison of experimental and computed results for Case 3 in loose sand.

along prescribed trajectories. Predictions are compared with experimental data to demonstrate and evaluate the performance of the model. The main findings and conclusions are as follows:

(1) Using normalization, it is found that the yield envelopes for the plate at various penetration depths, in sand with differing density, can be unified. The size of the yield envelope is controlled by the vertical and horizontal loading capacities, which expand with plastic displacements and calculated by using analytical models. The plate's plastic displacements are determined by adopting a non-associated flow rule, which is proposed based on the experimental data.

(2) By comparing with the experimental force-displacement histories, it is demonstrated that the model can substantially predict the soil response as a plate moves translationally in sand at both loose and dense state. However, the local hardening and softening of forces appearing in dense sand cannot be captured by the current model.

(3) The work mainly aims to develop a basic modeling framework for predicting soil response as the movement of the plate is large, and the model certainly has considerable potential to be improved, such as accommodating characterization of force-displacement histories under more complex motions and loading conditions for various soil types.

CHAPTER 6

# Theoretical model: semi-analytical model for plate with rotational movement

## 6.1. Introduction

Focus in the previous chapter was on developing a semi-analytical model that can predict the force-displacement response as a plate performs large translational movements in sand. However, the prediction is achievable only when the plate remains vertical and no rotational movement is involved. To overcome the limitations, an enhanced semi-analytical model for predicting the force-displacement history as a plate moves along a large complex (translational and rotational) trajectory is constructed in this chapter. The core concept of this model is similar to that presented in Section 5.1, while differences do exist. This model involves a new variable, i.e., the plate's inclination angle throughout the motion, and thus the yield envelopes, flow rule, and hardening laws need to be modified to accommodate it. To do it in a generalized way, the moment $M$ should be involved, which would require a 3D yield envelope. For sake of simplicity, we do not establish the direct relationship between $M$ and the rotational increments but decompose a rotational increment to translational displacements for reducing the model to 2D and calculating the force responses in $V$ and $H$.

In this chapter, the model is demonstrated by first presenting a unified analysis of the experimental results reported in Chapter 3 (Section 3.4) to extract important features. Then, the numerical modeling framework is described, including the features, formulation, and

implementation. Finally, the model is validated by comparing the predictions against the results from experiments.

## 6.2. Analysis of experimental results: loading capacity of an inclined plate

Based on the experimental result for swipe and cutting tests in Chapter 3 (Figure 3.18), the force path developed in the positive swipe and cutting test shows an envelope that is similar to the yield envelope obtained from the tests using a vertical plate. Hence, the yield envelope for an inclined plate is taken to be the force path, which is a key feature of the enhanced semi-analytical model. Besides, the development of the vertical and horizontal loading capacity was obtained from the penetration and positive cutting tests, respectively. The experimental results will be analyzed and used to construct the hardening laws in the semi-analytical model. The in-depth analysis and the determination of the yield envelope and hardening laws are presented in the following sections.

### 6.2.1. Positive swipe test: normalized yield envelopes

The yield envelopes for plate inclined at various angles are illustrated in Figure 6.1(b). They are obtained by managing the load paths of positive swipe tests performed at the penetration depth $D = 30\,\text{mm}$ (presented in Section 3.4.2.1). It is observed that the yield envelope rotates with the plate's inclination angle $\alpha$. More specifically, as $\alpha$ changes from $0^\circ$ to $60^\circ$, the orientation of the yield envelope $\beta$ increases from $0^\circ$ to $18^\circ$, where $\beta$ is defined as the angle between the long-axis of the yield envelope (in the shape of semi-ellipse) and the horizontal axis. This observation that the envelope rotations with rotation of the plate is also manifested in a previous study by performing numerical tests [**207**].

The normalization of the load paths takes three steps. As demonstrated in Figure 6.2(a), the envelope is firstly rotated counterclockwise with an angle of $\beta$ so that its long axis is along the horizontal axis, and the obtained vertical and horizontal forces are denoted as $V'$ and $H'$. The next two steps are the same as the method used for normalizing the yield envelopes of the vertical plate (described in Section 5.2.1), which are shifting the envelope to make its starting point at the origin of the axes, and dividing the vertical and horizontal force by maximum vertical force $V_0$ and maximum horizontal force $H_0$, respectively. By using the method, the load paths in Figure 6.1(b) are normalized, which are presented in Figure 6.2(b). Overall, the normalized yield envelopes are virtually identical, and the value of $V'/V_0$ at the peak of $H'/H_0$ is about 0.3.

With substituting $V^*$ by $V'$ and $H$ by $H'$, the normalized yield envelopes can be described by the same expression used for defining the yield envelopes of a vertical plate (Equation 5.6):

$$f = \left(\frac{H'}{H_0}\right)^{\beta_1} - \frac{\beta_3^{\beta_3/(\beta_3-1)}}{\beta_3 - 1}\left[\frac{V'}{V_0} - \left(\frac{V'}{V_0}\right)^{\beta_3}\right] \tag{6.1}$$

$$V' = V\cos\beta + H\sin\beta + V_{t0}, \quad H' = H\cos\beta - V\sin\beta$$

Similarly, in Equation 6.1, $\beta_1$ and $\beta_3$ can be varied to adjust the curvature of the fitting curve and shift the peak to any desired normalized vertical load ($0 < V'/V_0 < 1$). Note that $V_{t0}$ refers to the tension component of the maximum vertical force and its value is neglected in this section.

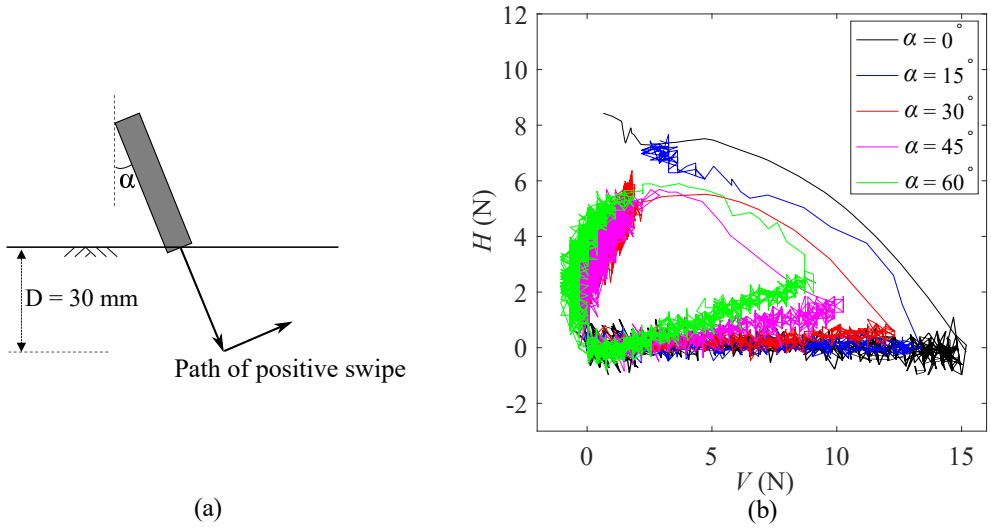


Figure 6.1. (a) Experimental setup and displacement path of the performed swipe tests; (b) obtained yield envelopes for plate inclined at various angles.

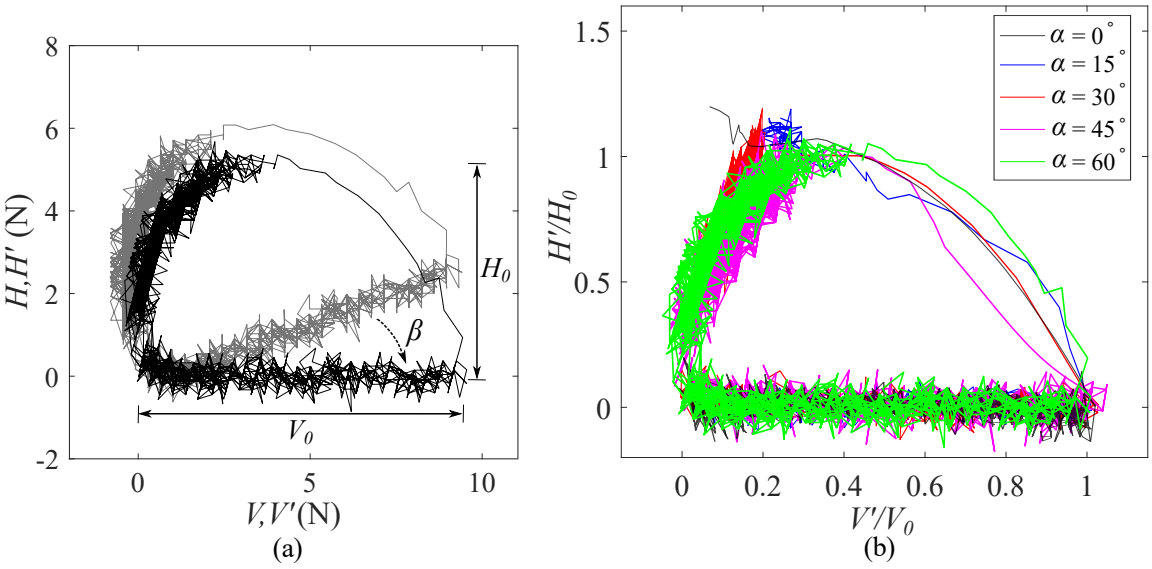


Figure 6.2. (a) Illustration of the first step to normalize the load paths obtained in positive swipe tests; (b) yield envelopes in normalized space.

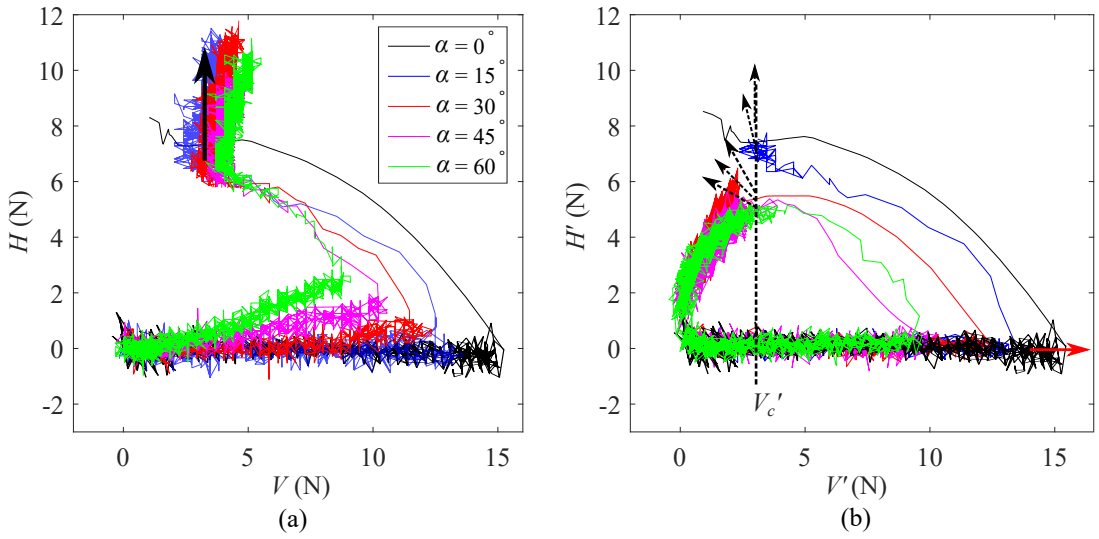


Figure 6.3. Directions of the incremental displacement (red arrow) on yield envelope (black lines) for three cases: (a) $D = 60\,\text{mm}$ in dense sand; (b) $D = 60\,\text{mm}$ in loose sand; (c) $D = 45\,\text{mm}$ in loose sand.

### 6.2.2. Positive swipe and cutting test: flow rule

The flow rule in this enhanced semi-analytical model is built on the basis of the flow rule for the vertical plate (presented in Section 5.2.2). The new flow rule should capture the experimental observations extracted from the positive swipe and cutting tests, which are illustrated in Figure 6.3. According to the load paths of positive cutting tests (Figure 6.3(a)), the incremental plastic displacement vector should be purely horizontal ($\Delta w^p = 0$) at the turning point of the load path, i.e., the point that $V$ changes from decreasing to increasing. At this point, the force ratios ($H/V$) are found to be approximately the same as $1/\tan\phi_w$ for the cases with various $\alpha$. Figure 6.3(b) shows the load paths of the positive swipe test under the $V' - H'$ coordinate system (after rotation), which has two distinct features. When $H'/V' = 0$, the incremental plastic displacement vector is purely vertical ($\Delta u^p = 0$). At the point that soil response enters plasticity (the experimental data becomes noisy), the

incremental plastic displacement vector should be normal to the inclined plate, where the $V'$ is found to be approximately the same for the cases with various $\alpha$. To capture the above features, the Equation defining the incremental plastic displacement ratio for a vertical plate (Equation 5.8) is modified for describing that for an inclined plate, which is expressed as

$$\frac{du_p}{dw_p} = \begin{cases} \eta \mathrm{H}(H') \tan^2\phi \tan\left[\frac{\pi}{2}\left(\frac{H}{V\tan\phi_w}\right)^{1.5}\right] & \frac{H}{V} < \frac{1}{\tan\phi_w} \\ \frac{1}{-\tan(\alpha V_c'/V')} & \frac{H}{V} \geq \frac{1}{\tan\phi_w} \end{cases} \tag{6.2}$$

In Equation 6.2, $\eta$ is the fitting parameter; $\mathrm{H}(H')$ is a Heaviside function which returns 0 or 1 when $H' = 0$ or $H' > 0$ respectively; $\phi$ is the friction angle of soil; $\phi_w$ is the friction angle at the soil-plate interface; $\alpha$ represents the inclination angle of the plate; $V_c'$ is the critical vertical force at which the incremental plastic displacement vector is normal to plate.

### 6.2.3. Penetration and positive cutting test: hardening law

According to Equation 6.1, the size of the yield envelope is controlled by the maximum vertical and horizontal force ($V_0$ and $H_0$) after the load path is rotated back. Similar to the concept of vertical loading capacity in the semi-analytical model for a vertical plate (Section 5.2.1), $V_0$ is assumed as the sum of the maximum vertical force in compression $V_{c0}$ and in tension $V_{t0}$. From a physical viewpoint, $V_{c0}$ and $V_{t0}$ can be understood as the resultant forces on the plate when the plate is penetrated and pulled out, respectively, at a certain depth; $H_0$ can be considered as the horizontal resistance generated from the cutting tests for a plate that is 'wished in place,' i.e., the horizontal resistance is 0 at the start of cutting. Based on the above analysis, the original force-displacement curves in the penetration and cutting process (Figure 3.20 and 3.19) can be converted for studying the development of $V_{c0}$

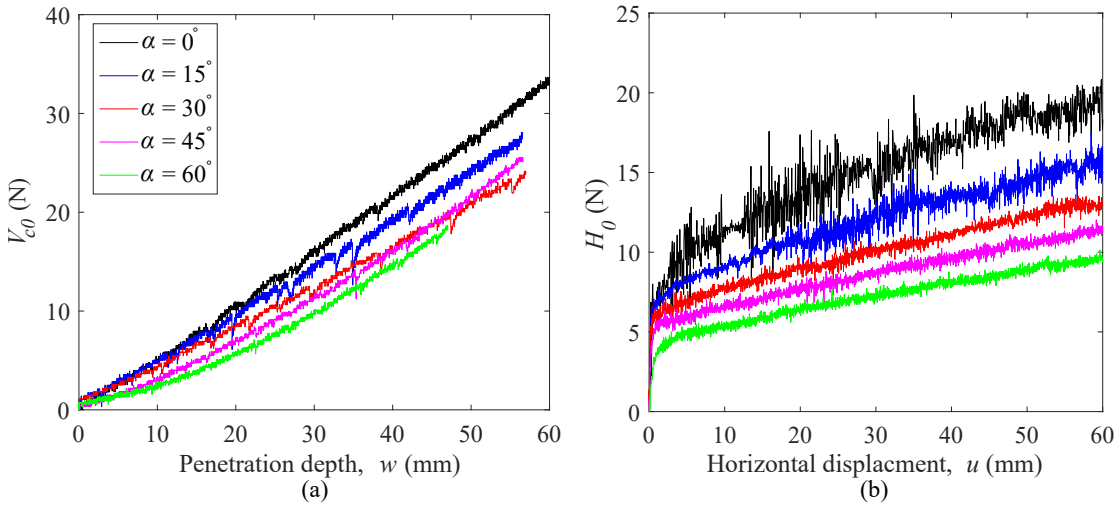


Figure 6.4. (a) Development of maximum vertical force $V_0$ with the vertical displacement; (b) development of maximum horizontal force $H_0$ with the horizontal displacement.

and $H_0$, which are illustrated in Figure 6.4. The value of $V_{c0}$ is calculated as the resultant force during the penetration process, and $H_0$ is computed by subtracting the horizontal force generated in the penetration from the total horizontal force. From the $V_{c0}$-$w$ curves, the rate of increase of $V_{c0}$ with respect to penetration depth decreases as the inclination angle of the plate becomes larger, which is similar to the observation in Figure 3.20. From the $H_0$-$u$ curves, at any same horizontal displacement $u$, $H_0$ normally decreases with increasing the inclination angle of the plate, even at the very beginning of the cutting process ($u \approx 0$), and the curves show more separation than those of $H$-$u$ (Figure 3.19).

A more detailed analysis on the development of $V_{c0}$ is conducted. Based on the experimental data presented in Figure 6.4(a), the ratio of the $V_{c0}$ for plate inclined at various $\alpha$ to that for a vertical plate (i.e. $V_{0\alpha}/V_{00}$) can be calculated for the entire penetration process, which is illustrated in Figure 6.5(a). It indicates that the force ratio $V_{0\alpha}/V_{00}$ generally evolves with the penetration depth $w$ linearly, and the relationship can be expressed by

$V_{0\alpha}/V_{00} = aw/B + b$. By using least-squares fitting, the parameters $a$ and $b$ can be obtained for the plate inclined at different angles. Figure 6.5(b) shows how parameters $a$ and $b$ vary with inclination of the plate $\alpha$. When $\alpha = \pi/12$ and $\pi/6$, parameter $a$ is close to 0; from $\alpha = \pi/6$, it increases with $\alpha$ linearly. This relationship can be described by the equation

$$a(\alpha) = \max(0, \alpha - \frac{\pi}{6})/21 - 0.0014 \tag{6.3}$$

where $\max(0, x)$ is a function returning the larger value between 0 and $x$. The performance of this equation is also shown in Figure 6.5(b). The parameter $b$ clearly decreases with the increase of $\alpha$, and a linear function can express the relationship

$$b(\alpha) = -0.63\alpha + 1.05 \tag{6.4}$$

In this equation, $-0.63$ and 1.05 are the fitted parameters based on the least-square method.

## 6.3. Numerical modeling

This section describes the formulation of the enhanced semi-analytical model for predicting the load-displacement response of a plate moving translationally and rotationally. The principal concepts adopted in the model are summarized as follows. At any condition of a plate moving in soil, a yield envelope in $V$-$H$ space will be established. Any changes of load within this envelope will only result in elastic deformation. The elastic behavior is linear, specified by a set of elastic constants. Load points touching the yield envelope can result in plastic deformation, which is determined by using the non-associated flow rule. A yield envelope is defined by its size and orientation. The size ($V_0$, $H_0$) of the yield envelope varies as the plate is rotated to different angles, pushed into the soil, or moved horizontally

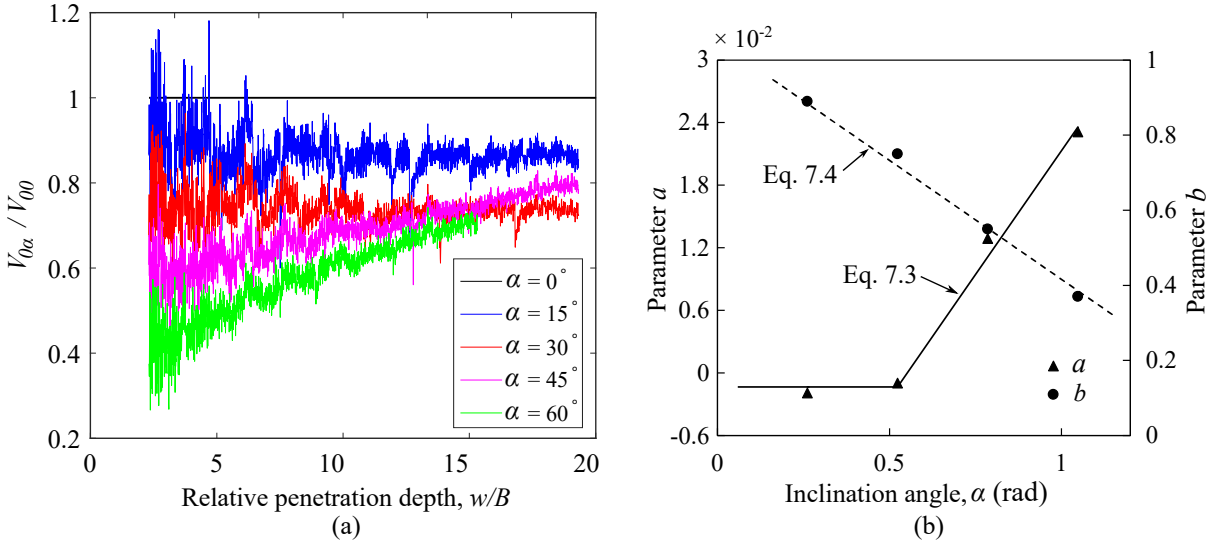


Figure 6.5. (a) The development of the ratio between the maximum vertical force of plate inclined at various angle $V_{0\alpha}$ and the maximum vertical force of the vertical plate $V_{00}$; (b) relationship between parameters $a$, $b$ and inclination angles of the plate.

further, and its orientation ($\beta$) changes with the inclination angle of the plate. Thus, the hardening law is specified by three relationships: the dependence of $V_0$ and $H_0$ on the plastic displacement increments; the dependence of $\beta$ on inclination angle of the plate. The first two relationships are established by combining analytical solutions, while the last is determined through correlation based on the experimental data.

### 6.3.1. Features of model

**6.3.1.1. Elastic response.** The elastic relationship between the load increments ($\mathrm{d}V$, $\mathrm{d}H$) and the corresponding elastic displacements ($\mathrm{d}w_e$, $\mathrm{d}u_e$) is

$$\begin{bmatrix} \mathrm{d}V \\ \mathrm{d}H \end{bmatrix} = 2B \begin{bmatrix} k_v & 0 \\ 0 & k_h \end{bmatrix} \begin{bmatrix} \mathrm{d}w_e \\ \mathrm{d}u_e \end{bmatrix} \tag{6.5}$$

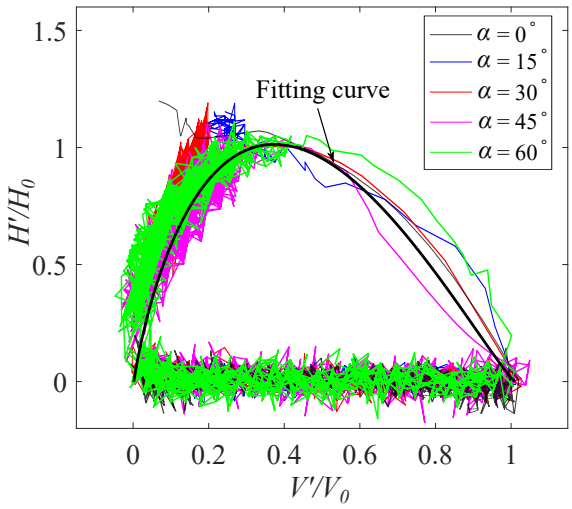


Figure 6.6. Fitting yield envelope with Equation 6.6.

where $B$ is the half-width of the plate, $k_v$ and $k_h$ are the elastic stiffness factors in the vertical and horizontal direction of the plate system, and their values mainly depend on the relative density of sand, the relative depths, and the inclination angle of the plate. For the sake of simplicity, the influence of the plate inclination angle on $k_v$ and $k_h$ is not considered in this study, and thus $k_v$ and $k_h$ (unit: kN/m$^2$) are determined by: $k_v/(\gamma B) = 13 + 20D/B$, $k_h/(\gamma B) = 40 + 50D/B$, which is the same as that used for a vertical plate in loose sand. Here the depth $D$ refers to the plastic vertical displacement $w_p$.

**6.3.1.2. Generalized yield envelope.** In Section 6.2.1 it was found that the experimental yield envelopes can be described by the form

(6.6)
$$f = \left(\frac{H\cos\beta - V\sin\beta}{H_0}\right)^{\beta_1} - \frac{\beta_3^{\beta_3/(\beta_3-1)}}{\beta_3 - 1}\left[\frac{V\cos\beta + H\sin\beta + V_{t0}}{V_0} - \left(\frac{V\cos\beta + H\sin\beta + V_{t0}}{V_0}\right)^{\beta_3}\right]$$

where $V_0$ and $H_0$ is the maximum vertical and horizontal force after the original yield envelope is rotated back. Inside the yield envelope $f < 0$ the behavior is elastic, governed

by Equation 6.5. For force points $(V, H)$ lying on the yield envelope, $f = 0$, and the plate behavior is elastoplastic. By using least-square method to fit the yield envelopes obtained from positive swipe tests, the best fit parameter values were derived for an inclined plate in sand: $\beta_1 = 0.90$, $\beta_3 = 0.95$, which are close to the values fitted for a vertical plate, i.e., $\beta_1 = 0.885$, $\beta_3 = 1.005$. When the plate's inclination angle is 0, i.e., the plate is vertical, the yield envelopes in the two models should be identical. Hence, to be consistent with the Equation 5.6 as well as keep the generality of Equation for describing the yield envelope, the parameters used for the vertical plate (in Equation 5.6) is adopted in this study. The fitting performance is illustrated in Figure 6.6, which indicates that the fitting curve can represent the experimental yield envelopes satisfactorily.

**6.3.1.3. Flow rule.** As presented in Section 6.2.2, the ratio of the incremental plastic displacements can be described by the Equation 6.2. To make the flow rule in the case of $\alpha = 0$ consistent with the original flow rule for a vertical plate (Equation 5.9), the parameter $\eta$ in Equation 6.2 is set as 7. Based on the experimental data shown in Figure 6.3(b), variable $V_c'$, referring to the critical vertical force at which the incremental plastic displacement vector is normal to plate, is determined as 2.5. After deciding the parameters, the flow rule is defined based on the ratio of the incremental plastic displacement without deriving the explicit expression of $P$, which is expressed as

$$\begin{bmatrix} \mathrm{d}u_p & \mathrm{d}w_p \end{bmatrix} = \lambda \begin{cases} \begin{bmatrix} 7\mathrm{sgn}(H')\tan^2\phi\tan\left[\frac{\pi}{2}\left(\frac{H}{V\tan\phi_w}\right)^{1.5}\right] & 1 \end{bmatrix} & \frac{H}{V} < \frac{1}{\tan\phi_w} \\ \begin{bmatrix} 1 & -\tan(2.5\alpha/V') \end{bmatrix} & \frac{H}{V} \geq \frac{1}{\tan\phi_w} \end{cases} \tag{6.7}$$

**6.3.1.4. Hardening law.** In this model, a yield envelope in $V$-$H$ space is defined by its size and orientation. The size of the yield envelope is controlled by the maximum vertical and horizontal force ($V_0$ and $H_0$) after it is rotated back, and its orientation ($\beta$) changes with the inclination angle of the plate. The methods for estimating these variables are discussed below.

As discussed in Section 6.2.3, $V_0$ is composed of the maximum vertical force in tension $V_{t0}$ and that in compression $V_{c0}$. The former is approximated by $V_{t0} = \tan\phi_w \gamma D^2 K_0$, and $V_{c0}$ is estimated by combining the experimental data and analytical method (described in Section 5.3.1.4). Based on the experimental analysis on the penetration tests (presented in Section 6.2.3), the development of an inclined plate's vertical force can be evaluated as

$$V_{0\alpha} = V_{00}(aw/B + b) \tag{6.8}$$

In the equation, the parameter $a$ and $b$ are functions of $\alpha$, expressed as Equation 6.3 and 6.4, respectively; $V_{00}$ is the maximum vertical force in compression for a vertical plate (i.e. $\alpha = 0°$), which can be determined by applying the analytical solution proposed by Durgunoglu and Mitchell [**204**], as described in Section 5.3.1.4. By combining the analytical solution with the experimental finding, $V_{c0}$ for an inclined plate can be computed, and its expression can be simplified as $V_{c0} = V_{c0}(D/B, \phi, \phi_w, \gamma, \alpha)$. Besides, as indicated in Figure 6.3(a), the vertical forces increase with the horizontal forces linearly and the force ratios are nearly constant after reaching the peak of $H$ in the cutting process. Similar to the observation for a vertical plate (presented in Section 5.3.1.4), the force ratio $H/V$ is analyzed to be equal to $1/\tan\phi_w$. Therefore, the development of maximum horizontal force has a contribution

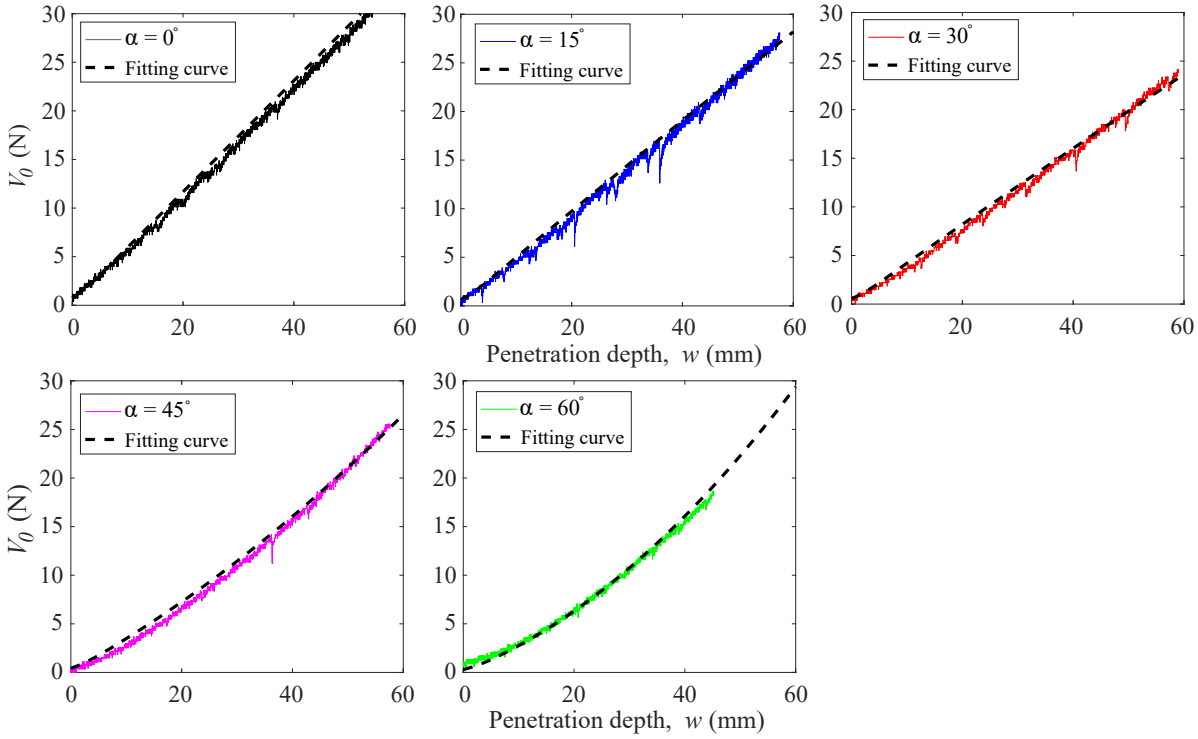


Figure 6.7. Estimated and experimental force-displacement histories of penetration tests

on $V_{c0}$, i.e., $\Delta V_{c0} = \Delta H_0 \tan\phi_w$. With all above analysis, the evolution of the maximum vertical force is expressed as

$$V_0 = V_0(D/B, u, \phi, \phi_w, \gamma, \alpha). \tag{6.9}$$

Figure 6.7 illustrates the comparison between the experimental force-displacement histories in penetration tests and the estimated responses by using the above method. It is observed that the estimation can match the test results well. In the computations, $\phi_w = 15.5°$ and $\phi = 30.7°$, which are the values determined in section 5.3.1.3 and section 5.3.1.4 for the loose sand (the same soil samples are used in this section). The same values will also be used for estimating $H_0$ in this section.

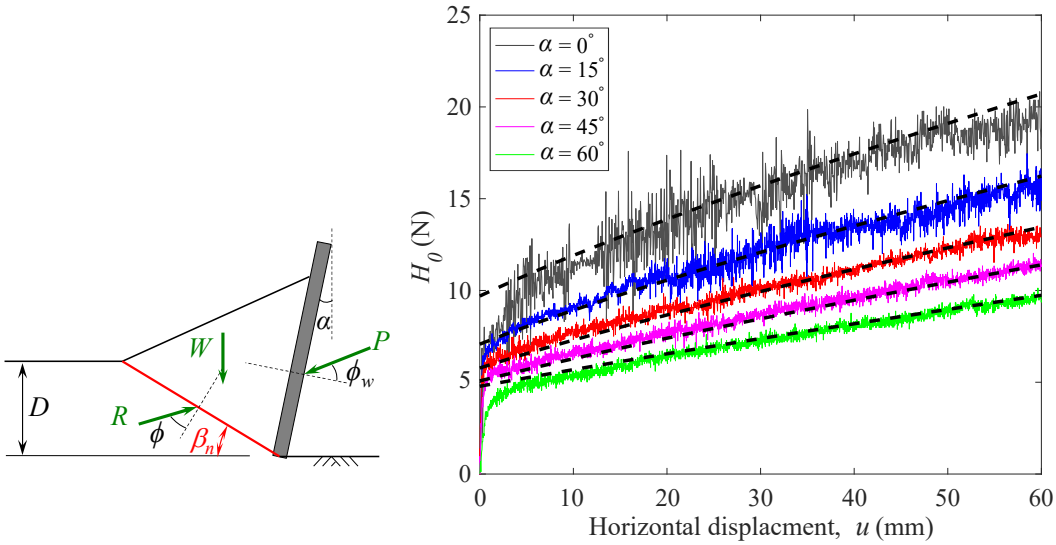


(a) (b)

Figure 6.8. Hardening law in $H_0$: (a) assumed deformation mode in the analytical model for cutting by an inclined plate; (b) estimated and experimental force-displacement histories in the positive cutting tests.

The method for calculating $H_0$ is developed based on the analytical solution for evaluating a vertical plate's horizontal loading capacity (presented in Section 5.3.1.4). Figure 6.8(a) shows the assumed deformation mode induced by an inclined plate in the cutting process, which is similar to that for a vertical plate (illustrated in Figure 5.9(a)). All deformation occurs along a single, straight slip surface that extends from the tip of the plate towards the soil surface at some unknown inclination angle $\beta$. A straight line approximates the unknown free surface, and potential volume change within the material is neglected. By using the Mohr-Coulomb yield criterion, the force $H$ required to displace the plate can be derived based on force equilibrium, which is expressed as

$$H = W \frac{\tan(\beta_n + \phi)}{1 + \tan(\alpha - \phi_w)\tan(\beta_n + \phi)}. \tag{6.10}$$

In this model, $W$ is estimated as

$$W = \gamma \left( D^2/(2\tan\beta_n) + uD + D^2 \tan\alpha/2 \right). \tag{6.11}$$

Similarly, based on the principal of minimum effort, the optimal $\beta_n$ in Equation 6.10 is evaluated by minimizing $H$ through solving $\partial H/\partial\beta_n = 0$. Thus, the optimal force $H$ (i.e. the minimum $H$) can be obtained:

$$H_0 = H_0(D, u, \alpha, \phi, \phi_w, \gamma). \tag{6.12}$$

Using this equation, the development of $H_0$ with the horizontal displacement $u$ for the plate inclined at different angles is estimated and compared with the experimental data, as illustrated in Figure 6.8(b). The comparison clearly indicates that the analytical method can calculate the force-displacement response reasonably.

The equation for estimating the orientation of the yield envelope $\beta$ for an inclined plate is developed based on experimental observations. Figure 6.9 shows the correlation between the $\beta$ and the inclination angle of the plate $\alpha$, where the $\beta$ is measured from Figure 6.1(b), i.e., yield envelopes for plates inclined at various angles. It is found that a quadratic function can describe the relationship between $\beta$ and $\alpha$

$$\beta = 0.3\alpha^2 + 0.03\alpha \tag{6.13}$$

where 0.3 and 0.03 are the fitting parameters.

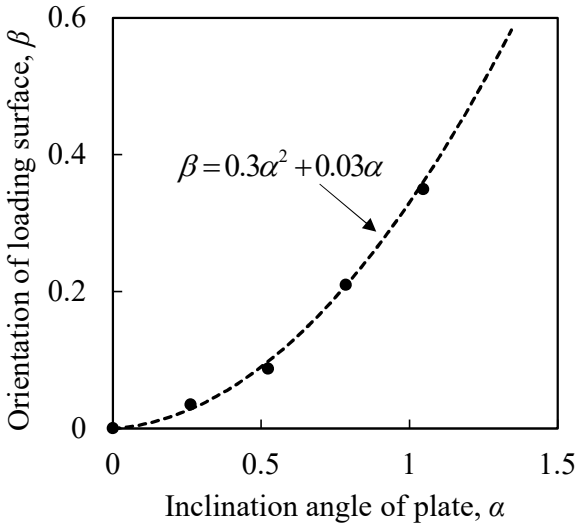


Figure 6.9. Correlation between the yield envelope's orientation and the plate's inclination angle.

By adopting the above hardening laws, the yield envelope's mobilization resulting from translational and rotational movements can be determined.

### 6.3.2. Mathematical formulation

With the defined features of elastic response, yield envelope, flow rule, and hardening rule, the elastoplastic force-displacement matrix can be derived. As a loading increment is purely elastic, the incremental forces d$\mathbf{F}$ is related to incremental displacements d$\mathbf{u}$ with the relationship illustrated in Equation 6.5.

When the stress state is on the yield envelope ($f(\mathbf{F}, V_0, H_0, \beta) = 0$) and the incremental loading causes plasticity, the force point remains on the yield envelope to satisfy the consistency condition

$$df = \frac{\partial f}{\partial \mathbf{F}} d\mathbf{F} + \frac{\partial f}{\partial V_0} dV_0 + \frac{\partial f}{\partial H_0} dH_0 + \frac{\partial f}{\partial \beta} d\beta = 0 \tag{6.14}$$

In the equation, the incremental force is expressed as

$$d\mathbf{F} = \mathbf{D_e}(d\mathbf{u} - d\mathbf{u_p}) \tag{6.15}$$

where $D_e$ is the elastic stiffness, and its expression is shown in Equation 6.5. The hardening of the internal variables is

$$\begin{aligned} dV_0 &= \frac{\partial V_0}{\partial V_{00}} \left(\frac{\partial V_{00}}{\partial \mathbf{u_p}}\right)^T d\mathbf{u_p} + \left(\frac{\partial V_0}{\partial \alpha}\right) d\alpha, \\ dH_0 &= \left(\frac{\partial H_0}{\partial \mathbf{u_p}}\right)^T d\mathbf{u_p} + \left(\frac{\partial H_0}{\partial \alpha}\right) d\alpha, \\ d\beta &= \frac{\partial \beta}{\partial \alpha} d\alpha \end{aligned} \tag{6.16}$$

By taking Equation 6.15, 6.16 and flow rule ($\mathrm{d}\mathbf{u_p} = \lambda \frac{\partial P}{\partial \mathbf{F}}$) into Equation 6.14, the consistency condition becomes

$$\begin{aligned} df = &\left(\frac{\partial f}{\partial \mathbf{F}}\right)^T \mathbf{D_e} d\mathbf{u} - \lambda \left(\frac{\partial f}{\partial \mathbf{F}}\right)^T \mathbf{D_e} \frac{\partial P}{\partial \mathbf{F}} + \lambda \frac{\partial f}{\partial V_0} \left(\frac{\partial V_0}{\partial \mathbf{u_p}}\right)^T \frac{\partial P}{\partial \mathbf{F}} + \lambda \frac{\partial f}{\partial H_0} \left(\frac{\partial H_0}{\partial \mathbf{u_p}}\right)^T \frac{\partial P}{\partial \mathbf{F}} \\ &+ \frac{\partial f}{\partial \beta} \frac{\partial \beta}{\partial \alpha} d\alpha + \frac{\partial f}{\partial V_0} \frac{\partial V_0}{\partial \alpha} d\alpha + \frac{\partial f}{\partial V_0} \frac{\partial H_0}{\partial \alpha} d\alpha = 0 \end{aligned} \tag{6.17}$$

Thus, the plastic multiplier $\lambda$ can be calculated as a function of the imposed incremental displacement $d\mathbf{u}$ and rotation angle $d\alpha$:

$$\begin{aligned} &\lambda = \frac{1}{H_c - H_a} \left( \left(\frac{\partial f}{\partial \mathbf{F}}\right)^T \mathbf{D_e} d\mathbf{u} + \frac{\partial f}{\partial \beta} \frac{\partial \beta}{\partial \alpha} d\alpha + \frac{\partial f}{\partial V_0} \frac{\partial V_0}{\partial \alpha} d\alpha + \frac{\partial f}{\partial H_0} \frac{\partial H_0}{\partial \alpha} d\alpha \right), \\ &\text{with} \quad H_c = \left(\frac{\partial f}{\partial \mathbf{F}}\right)^T \mathbf{D_e} \frac{\partial P}{\partial \mathbf{F}}, \quad H_a = \frac{\partial f}{\partial V_0} \left(\frac{\partial V_0}{\partial \mathbf{u_p}}\right)^T \frac{\partial P}{\partial \mathbf{F}} + \frac{\partial f}{\partial H_0} \left(\frac{\partial H_0}{\partial \mathbf{u_p}}\right)^T \frac{\partial P}{\partial \mathbf{F}} \end{aligned} \tag{6.18}$$

The incremental forces can be obtained by substituting Equation 6.18 back into Equation 6.15:

$$
\begin{aligned}
d\mathbf{F} &= \mathbf{D_e}\left(d\mathbf{u} - \lambda\frac{\partial P}{\partial \mathbf{F}}\right) \\
&= \frac{H_a}{H_a - H_c}\mathbf{D_e}d\mathbf{u} + \frac{1}{H_a - H_c}\frac{\partial f}{\partial \alpha}\mathbf{D_e}\frac{\partial P}{\partial \mathbf{F}}d\alpha \\
&= \mathbf{D^t_{ep}}d\mathbf{u} + \mathbf{D^r_{ep}}d\alpha
\end{aligned}
\tag{6.19}
$$

### 6.3.3. Implementation

The enhanced semi-analytical model is also implemented by using displacement control, which allows the calculation of force-displacement history in the loading condition that the plate moves along a large complex (translational and rotational) trajectory. The procedure is similar to that used in the model for a vertical plate, and the details are described as follows:

(1) Initializing input data, which includes model parameters, initial conditions, and the magnitude of applied displacement paths. The required parameters used in the enhanced model are summarized in Table 6.1. The initial condition refers to the force $\mathbf{F}$, translational displacement $\mathbf{u}$, inclination angle of the plate $\alpha$ and loading capacities $V_0$, $H_0$ at the start of the loading process. Besides, in this model, each applied path is described by giving the translational displacement (vertical and horizontal displacement, $u$ and $w$) and the rotational angle of the plate, as well as the number of steps used to perform the movement. It should be noted that the incremental translational movement has two components, i.e., the purely translational displacement, $d\mathbf{u_t}$ and the translational displacement generated by the plate's

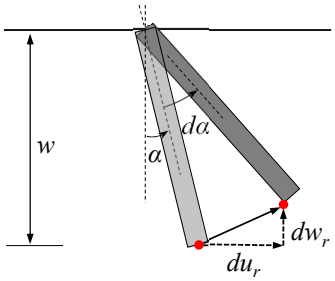


Figure 6.10. Schematic illustration of the translational displacement generated from plate's rotation.

Table 6.1. Parameters used in the enhanced semi-analytical model.

| **Parameters** | **Explanation** |
|---|---|
| $B$ (m) | Width of the object |
| $\gamma$ (N/m$^3$) | Unit weight of sand |
| $\phi$ | Friction angle of sand |
| $\phi_w$ | Sand-plate interface friction angle |
| $k_v$ | Elastic stiffness factor in vertical direction |
| $k_h$ | Elastic stiffness factor in horizontal direction |
| $\beta_1, \beta_3$ | Curvature factors for yield envelope |
| $\eta, V_c^{'}$ | Factors for flow rule |
| $a, b$ | Factors for estimating the hardening in $V_0$ |

rotation, $d\mathbf{u_r}$. The latter is illustrated in Figure 6.10, where $du_r$ and $dw_r$ is approximated by $wd\alpha$ and $-w\tan\alpha d\alpha$, respectively.

(2) For any given $n^{th}$ increment of displacement $\Delta\mathbf{u}_{n+1}$ and increment of rotational angle $\Delta\alpha_{n+1}$, the updated force is initially assumed to be elastic. Therefore, $\mathbf{F}_{n+1}^{T} = \mathbf{F}_n + \mathbf{D}_e(\mathbf{u^p}_n)\Delta\mathbf{u}_{n+1}$, where the superscript 'T' stands for a trial state and the subscript denotes the process step. In a certain step, the plastic displacement is preserved as the previous values, $\mathbf{u^p}_{n+1} = \mathbf{u^p}_n$. Thus, the elastic stiffness is fixed as its values is completely determined by $\mathbf{u^p}_n$, while the internal variables $V_0, H_0$ and $\beta$ is updated to $V_0(\mathbf{u^p}_n, \alpha_{n+1})$, $H_0(\mathbf{u^p}_n, \alpha_{n+1})$

and $\beta(\alpha_{n+1})$, respectively. If $f(\mathbf{F}^T_{n+1}, V_0, H_0, \beta) < 0$, the process at the step $n+1$ is considered elastic and then update the corresponding force and displacement.

(3) If the above yield condition is violated for the trial state, the force state surpasses the yield envelope. In this case, provided that yielding does not occur in the previous step, the intersection of the force path and yield envelope is found by using the Bisection method, where the force is recorded as $\mathbf{F_m}$. The portion of the load path inside the yield envelope is evaluated by defining a quantity $\kappa = |\mathbf{F_m} - \mathbf{F}|/|\mathbf{F}|$. Then, the force and displacement increments are calculated as $\kappa \mathbf{D}_e \Delta \mathbf{u}_{n+1}$ and $\kappa \Delta \mathbf{u}_{n+1}$. After the updates, the force state is now on the yield envelope. Based on the mathematical formulation in the previous section, the elastoplastic stiffness matrix can be calculated. Accordingly, force increments are computed and updated.

(4) Steps (2)-(3) are repeated until the entire force-displacement history is obtained.

## 6.4. Model validation

Computational results have been obtained in various loading conditions using the enhanced semi-analytical model. Three cases for which the plate moves along the trajectory composed of multiple complex paths are selected to demonstrate the model performance.

### 6.4.1. Case 1

Figure 6.11 (a) shows the specified plate's trajectory in Case 1. The plate penetrates the sand for 30 mm first, followed by a rotation of 10°. Then, it moves in the direction with $w/u$ = 1/2. Finally, the movement combining translation and rotation is performed. It should be noted that in experiments, the path that combines translation and rotation motion is executed by setting the start and end point of the path and rotating the joint 5 of robot

(described in Section 2.3.2) at a constant speed around the intersection between the plate and soil surface.

The comparisons between the prediction and experimental data for the Case 1 are illustrated in Figure 6.11(b) and (c). In general, the model can capture the characteristics of the force-displacement history in the process, reflected by clearly showing the turning points at the junctions of paths. However, deficiencies do exist. First, overall the horizontal force $H$ is underestimated, which is more notable after the plate is rotated. This is mainly because the model fails to capture the rapid increase of $H$ at the start of Path III in the experiment. Second, a mismatch is observed on the prediction of Path II. The predicted $V$ drops faster than the experimental result, and the predicted $H$ is larger. It is important to indicate that the mismatch appears at the start of the path with a displacement of 1.5 mm, which is actually a small portion of Path II. These deficiencies might result from the difference between the performed trajectories in the numerical and physical test, and the details will be discussed in the Section 6.4.3.

### 6.4.2. Case 2

In Case 2, the specified trajectory is more complex and composed of 6 continuous paths, as illustrated in Figure 6.12(a). The plate first penetrates sand for 30 mm and moves horizontally with a displacement of 10 mm. Then, the plate is rotated 6° and moved with $u = w = 3$ mm simultaneously, followed by a pure rotation of 9°. After that, it moves in the direction with $w/u = 1/2$. Finally, another movement that combines translation and rotation is performed.

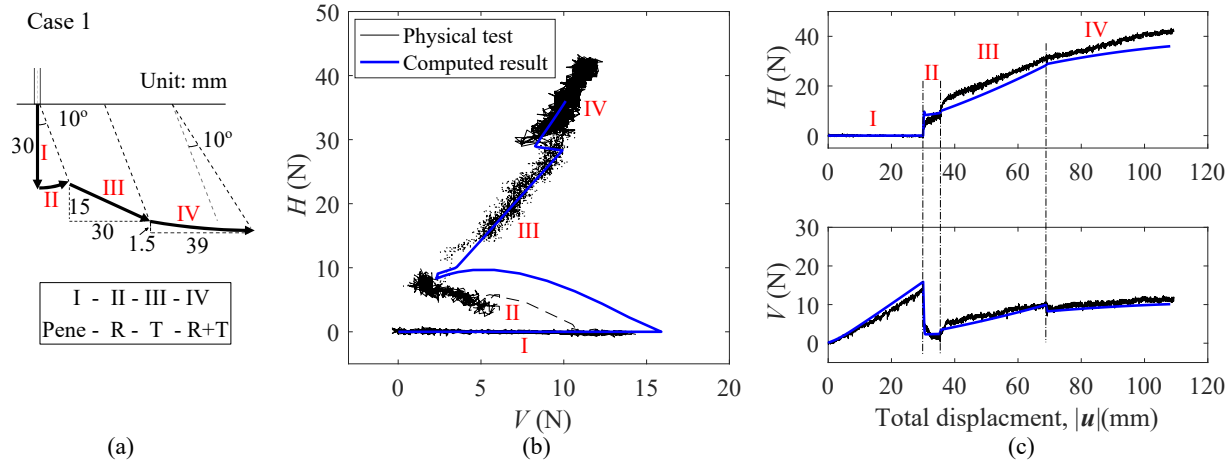


Figure 6.11. Case studies for the enhanced semi-analytical model in Case 1: (a) the specified trajectory of plate; the comparison between the experimental and computed results of (b) force path and (c) force-displacement histories. Note that in (a) 'pene' represents 'penetration,' 'T' represents 'translational movement,' 'RT' represents the combination of translational and rotational movement; and the different line types in (b) are used to distinguish the results generated from different paths.

Figure 6.12(b) and (c) shows the comparison between the computed and experimental force path and force-displacement histories, respectively. It is demonstrated that the computed result generally can match the experimental curve well. However, one may notice that the predictions in $V$ and $H$ are lower than the test result at the start of path V, which is similar to the observation in Path III of Case 1.

### 6.4.3. Case 3

As shown in Figure 6.13(a), the motions for Case 3 are the same as those in Case 2 except the first two paths. In Case 3, the plate penetrates sand for 20 mm first and then moves with a displacement of $u = w = 10$ mm.

Figure 6.13(b) and (c) shows the computed and experimental results in terms of force path and force-displacement histories, respectively. Comparing the experimental results of

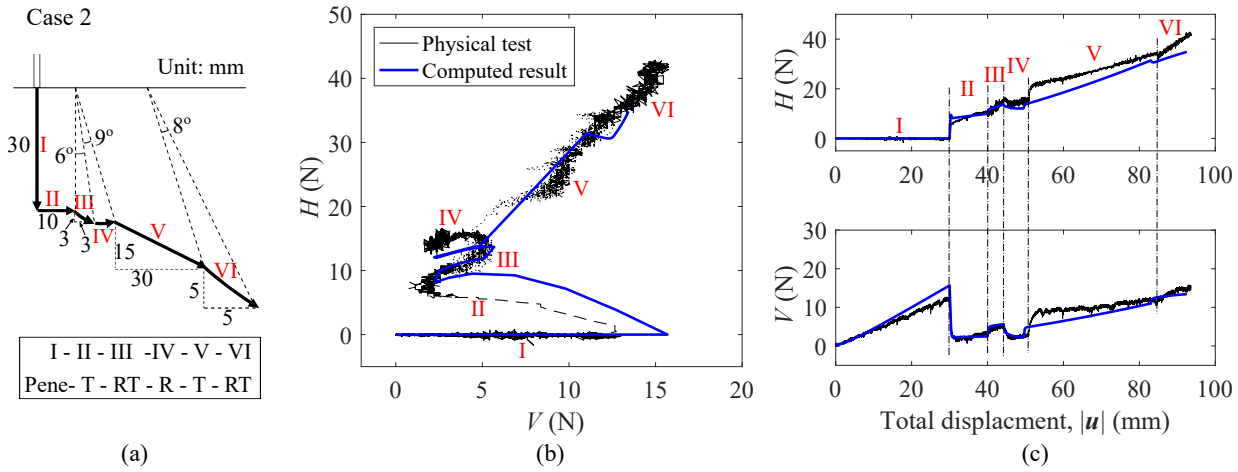


Figure 6.12. Case studies for the enhanced semi-analytical model in Case 2: (a) the specified trajectory of plate; the comparison between the experimental and computed results of (b) force path and (c) force-displacement histories.

Case 3 and Case 2, even though displacement histories before reaching the same intermediate point (at $w = 30\,\text{mm}$ and $u = 10\,\text{mm}$) are different, the force developments are nearly identical for the part where the performed paths are the same, i.e., path III – path VI. This characteristic, the displacement history has little influence on the soil response, can be captured by the semi-analytical model. Comparing the prediction with the experimental result for the Case 3, it is observed that the enhanced semi-analytical model generally can predict the complex force-displacement behavior in the process. At the same time, the major deficiency is similar to that of Case 2, i.e., the predicted $V$ and $H$ are lower than the test result at the start of path V.

### 6.4.4. Discussion on the case studies

The results of Case 1 - Case 3 indicate that the relatively poor match for all three cases generally appears when the plate undergoes a transition between a translational movement and a rotational movement, which might result from the difference between the performed

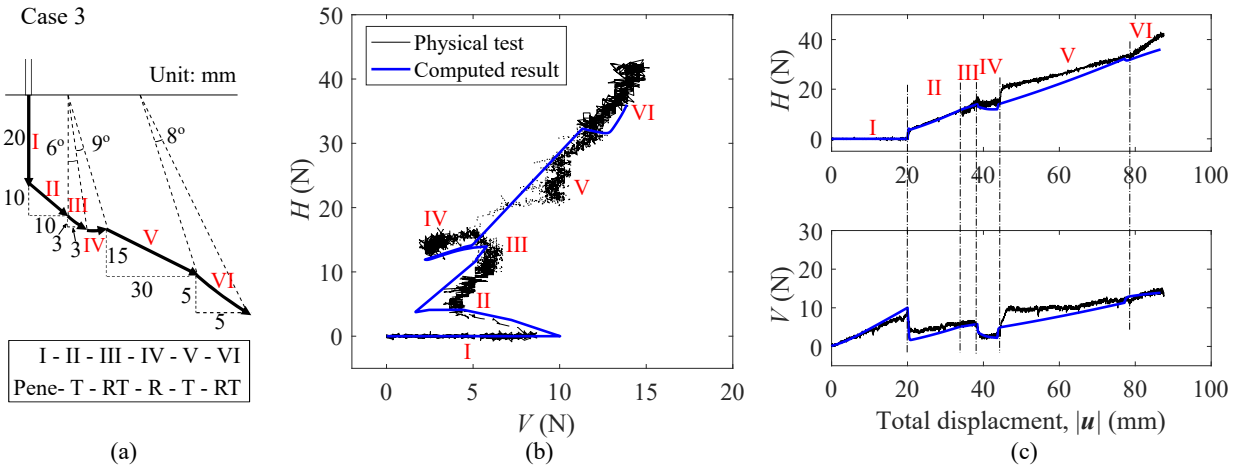


Figure 6.13. Case studies for the enhanced semi-analytical model in Case 3: (a) the performed trajectory of plate; the comparison between the experimental and computed results of (b) force path and (c) force-displacement histories.

trajectories in simulation and test. The difference is caused by the deviation of the executed robot's path in the junction of a linear movement and joint movement. Figure 6.14 shows two examples of the designed displacement paths (numerical test) and the executed ones (physical test). As indicated in Figure 6.14(a), for the transition from linear to joint movement, the robot' TCP first moves purely horizontally and then executes a path with a larger curvature than the designed one. This can cause $V$ to decrease at a slower rate than predicted, which is observed in Case 1 (Figure 6.11). Figure 6.14(b) indicates the transition from joint to linear movement. Instead of moving along the designed path straightly, the robot is executed to drift downward first and then moves along the linear path. The deflection can lead to an increase of $V$ and $H$, as observed in Case 2 and 3 (Figure 6.12 and 6.13). It is acknowledged that the difference between the designed and executed path does not completely account for the difference of the computed and experimental results but provides a reasonable explanation.

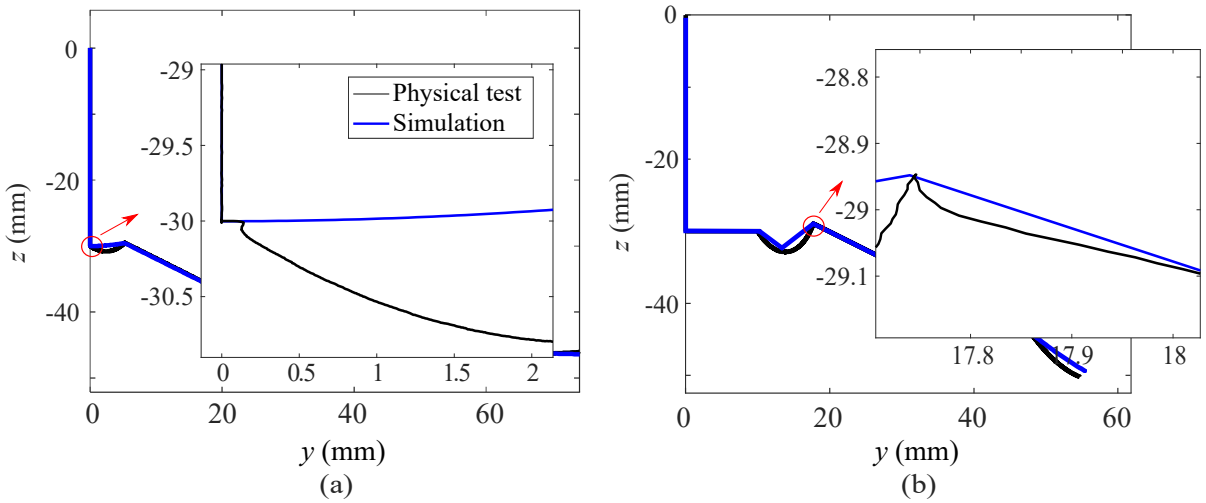


Figure 6.14. Examples of performed displacement paths in test and simulation: (a) Path I to Path II in Case 1; (b) Path IV to Path V in Case 2.

## 6.5. Summary

This chapter presents an enhanced semi-analytical model for predicting the force and displacement response as a plate moves along a large complex (translational and rotational) trajectory in loose sand. The model is developed by first completing a unified analysis of experimental results reported in Chapter 3 (Section 3.4). Based on the analysis, the numerical modeling framework, including the features, formulation, and implementation of the model, is built. To demonstrate and evaluate the enhanced semi-analytical model's performance, the soil responses in three cases that the plate performs multiple continuous complex paths are computed, and the predictions are compared against the experimental results. The main findings and conclusions are as follows:

(1) The yield envelopes for a plate inclined at various angles can be unified with normalization. At any condition, a yield envelope is defined by its size and orientation. The yield envelope's size is controlled by the maximum vertical and horizontal force and evolves with plastic displacements and inclination angle of the plate, while its orientation changes

with the inclination angle of the plate. The three variables ($V_0$, $H_0$, $\beta$) are calculated by using a semi-analytical, an analytical, and an experimental method, respectively. The plate's plastic displacements are determined by adopting a non-associated flow rule, which is built by enhancing the flow rule for a vertical plate with the capacity of capturing experimental observations extracted from the positive swipe and cutting tests.

(2) The computed force-displacement histories of the model are compared against the experimental data, demonstrating that the model can predict the soil response of a plate performing both translational and rotational movement with reasonable accuracy.

(3) The work aims to develop a basic modeling framework for predicting soil response when a plate moves along a translational and rotational trajectory. The proposed model is preliminary and possesses limitations than can be improved in future work. For example, the current model is developed only based on the test results obtained for loose sand. The investigations on soils with different properties are needed to improve the model's generality. Besides, the model cannot predict the soil response under the unloading condition, and the effect of the plate's inclination on the elastic modulus has not been considered.

CHAPTER 7

# Conclusion

The thesis is concerned with developing efficient techniques for predicting forces and deformations generated through soil-machine interaction. Specifically, a plasticity-based sequential kinematic model and a semi-analytical model (also known as macro-element model) derived from the generalized yield envelopes in geotechnical engineering were formulated and calibrated. The former can accurately predict soil responses, including soil deformation and force-displacement histories, with affordable computational cost. The latter is capable of generating force-displacement data in seconds to enable fast calculation for the purpose of design optimization and control algorithm development. Both techniques were developed based on experimental measurements for the most fundamental cases, including the particular cases of cutting and penetration. These measurements were completed with the essential help of the newly built experimental system that enables automated and efficient tests in SMI. In this final chapter, the principal conclusions of the work are summarized, and some possible directions for future research are discussed.

## 7.1. Main findings

The main findings are organized in terms of the development of laboratory (1), the SKM method (2-4), and the semi-analytical model (5-8):

(1) A new experimental system consisting of an industrial robot and a sand bed using fluidization was developed. It enables automated and efficient experimental studies in SMI

providing important data for the development of the theoretical models. In the system, the fluidized bed is used to prepare sand specimens, which allows the quick and repeatable preparation of a uniform sand bed with a broad range of relative density. The robot can move and track objects' movements and measure resistive forces with the accuracy required by small-scale tests. In particular, tests involving multi-axial motions can be easily conducted with the aid of the robot, which would otherwise require a complicated actuation and control system.

(2) The progression of soil deformation in two fundamental SMI processes, cutting and penetration, were investigated experimentally. For the cutting process, distinct soil responses are observed in loose and dense sand. In terms of the force-displacement histories, the force generally increases with the displacement in loose sand, while the force oscillates with a relatively large amplitude during the cutting process in dense sand. For the evolution of soil deformation in loose sand, a shear band sweeps over a small region first and then remains stationary for a period of time at one position while some temporary sweeps appear randomly. In dense sand, the shear band remains fixed for a long period of time until rapid and repeated sweeps precede a jump forward to a new location. In the penetration process, the evolution of soil deformation is investigated only on the sand at a dense state. The deformation patterns featured by shear localization forming, breaking down, and fading away are repeatedly observed in the process, and the force increases with the depth overall.

(3) The SKM model can quantitatively predict the progression of soil deformation under biaxial compression in loose and dense sand. While the measured incremental deformations indicate that the shear band takes place close to the peak stress ratio, the SKM model implies that it can appear much earlier and continuously form at variable locations to produce the

full observed evolution of soil deformation, i.e., soil deforms in a diffuse and non-homogeneous mode at first, followed by the appearance of a distinct shear band.

(4) For the cutting process, the SKM model can capture the distinct responses of loose and dense sand observed in experiments, including force-displacement histories and the evolution of soil deformation. More importantly, the SKM model identifies and explains sand's deformation mechanism in the cutting process: continuous discontinuity (localized deformation) propagates over regions. As it propagates, the sand on the localized region is hardening or softening, accompanying compaction or dilation.

(5) The experimental loading capacity for a vertical plate in loose and dense was measured. Through the experimental analysis, some critical features were extracted for developing the semi-analytical model. It was found that the elastic stiffness of the plate system evolves with the relative penetration depth linearly. The $V$-$H$ yield envelopes for the plate at various penetration depths of sands with different densities can be unified. The yield envelope's size is controlled by vertical and horizontal loading capacities, which are expanded with plastic displacements. Additionally, the plate's plastic displacements can be described by a non-associated flow rule, which is derived based on experimental data.

(6) Based on the experimental analysis, a semi-analytical model inspired by the generalized yield envelopes in geotechnical engineering was formulated. The model can simulate the process of a vertical plate moving in sand translationally and generate the force-displacement response in seconds. By comparing with the experimental observations, it is demonstrated that the model can substantially capture the response of sand at both loose and dense state.

(7) The experimental measurements were conducted to examine an inclined plate's loading capacity. It is found that the yield envelopes for a plate inclined at various angles can be unified with normalization. At any condition, a generalized yield envelope can be defined

by its size and orientation. The yield envelope's size is controlled by the maximum vertical and horizontal force, which evolves with plastic displacements and the inclination angle of the plate. The orientation of the yield envelope changes with the plate's inclination angle. The plate's plastic displacements can be described by a non-associated flow rule built by enhancing the flow rule for a vertical plate. The enhancement refers to the added capacity of capturing experimental observations extracted from the positive swipe and cutting tests.

(8) Based on the in-depth experimental analysis for an inclined plate's loading capacity, an enhanced semi-analytical model was built. This model can predict the force-displacement response for a more complex loading scenario, i.e., a plate undergoing translational and rotational movement with large displacement. The model's prediction was compared with the experimental data, showing that the model can reproduce the important features of the observed behaviors.

## 7.2. Future directions

In general, this study focuses only on the case that a plate moves in dry sand without unloading. The material type and configuration are only a small subset of the possibilities encountered in SMI applications. This work aims to open an opportunity to start a comprehensive study in this field. Some future directions in terms of the SKM and semi-analytical models are provided explicitly as follows.

### 7.2.1. SKM technique with enhanced kinematics and constitutive model

In Section 4.4, an SKM model for simulating the penetration process was developed, and the model produces a prediction that can match the experimental results as a whole. However, several shortcomings of the model are identified, such as prediction accuracy, generality, and

stability. These shortcomings could be improved by expanding the SKM formulation to include combined loading and enriched kinematics of sufficient complexity. For example, the more advanced constitutive models that account for hardening and softening (e.g., Extended Mohr-Coulomb model [**189**]) can be considered. One of the most critical tasks to achieve the goal is to invent an effective method to estimate the energy dissipation rate within an increment. Ideally, the estimation should be purely stress-independent. Future Efforts could be devoted to using a fictitious flow rule [**190**] or hyperplastic method [**191**].

### 7.2.2. Macro-element model

Force-displacement results obtained in the tests that a vertical plate moves translationally were compared with the prediction of the first semi-analytical model in Section 5.4. In general, it was found that the model performed well, reproducing the important features of the observed behavior in a satisfactory manner (both qualitatively and quantitatively). However, the local hardening and softening of forces appearing in dense sand cannot be captured by the model. Such an improvement might require deriving more complicated hardening laws.

The enhanced semi-analytical model presented in Chapter 6 provides a basic modeling framework for predicting soil response when a plate moves along a complex translational and rotational trajectory. This basic model has considerable limitations that could be overcome in future research. For example, the current model was developed based on the test results obtained from loose sand. The investigations on soils with different properties are needed to improve the model's generality, which requires a more extensive series of experiments. Additionally, the current model can only be used under the loading condition, which means that the soil response generated from the plate's retreat cannot be predicted. Another

improvement could be made by considering the effect of the plate's inclination on the elastic modulus.

### 7.2.3. Other material types

This work focuses only on dry sand (frictional material). Looking further ahead, expansion to fine-grained soil amenable to simplified constitutive modeling represents an interesting and promising area of future work, one in which the model formulation may in fact become simpler in many respects. While experimentally more difficult to investigate, fine-grained materials such as clay may be easier to assess within the framework of the SKM technique, especially on account of the fact that dissipation no longer depends on the stress state for a pressure-independent yield condition. Moreover, simplifications in the semi-analytical model most likely arise with respect to characterizing the yield surface and plastic flow rule.

# References


[1] "Caterpillar-d10." http://jasonrossearthmoving.com.au/equipment/caterpillar-d10/. Caterpillar-D10-Jason Ross Earthmoving.

[2] "Non-renewable resource." https://en.wikipedia.org/wiki/Non-renewable_resource#/media/File:Coal_mine_Wyoming.jpg. Wikimedia Foundation.

[3] "Solutions for construction machinery:ringfeder." https://www.ringfeder.com/industry-solutions/construction-machinery/.

[4] "Selge construction company-earthmoving: Midwest civil contractor." https://www.selgeconstruction.com/our-services/earthmoving/. Accessed: 2018-05.

[5] S. Moreland, K. Skonieczny, D. Wettergreen, V. Asnani, C. Creager, and H. Oravec, "Inching locomotion for planetary rover mobility," in *2011 Aerospace Conference*, pp. 1–6, IEEE, 2011.

[6] M. Goeller, A. Roennau, A. Gorbunov, G. Heppner, and R. Dillmann, "Pushing around a robot: Force-based manual control of the six-legged walking robot lauron," in *2011 IEEE International Conference on Robotics and Biomimetics*, pp. 2647–2652, IEEE, 2011.

[7] "Meet esa's spacebok robot." https://earthsky.org/space/meet-esas-spacebok-robot. EarthSky.

[8] J. Desrues, *La localisation de la déformation dans les matériaux granulaires*. PhD thesis, 1984.

[9] E. McKyes and O. Ali, "The cutting of soil by narrow blades," *Journal of Terramechanics*, vol. 14, no. 2, pp. 43–58, 1977.

[10] R. Godwin, "A review of the effect of implement geometry on soil failure and implement forces," *Soil and Tillage Research*, vol. 97, no. 2, pp. 331–340, 2007.

[11] J. P. Hambleton, S. Stanier, D. J. White, and S. W. Sloan, "Modelling ploughing and cutting processes in soils," *Australian Geomechanics*, vol. 49, no. 4, pp. 147–156, 2014.

[12] J. Hambleton and A. Drescher, "Modeling wheel-induced rutting in soils: Indentation," *Journal of Terramechanics*, vol. 45, no. 6, pp. 201–211, 2008.

[13] J. Hambleton and A. Drescher, "On modeling a rolling wheel in the presence of plastic deformation as a three-or two-dimensional process," *International Journal of Mechanical Sciences*, vol. 51, no. 11-12, pp. 846–855, 2009.

[14] J. Guo, L. Ding, H. Gao, T. Guo, G. Liu, and H. Peng, "An apparatus to measure wheel–soil interactions on sandy terrains," *IEEE/ASME Transactions on Mechatronics*, vol. 23, no. 1, pp. 352–363, 2018.

[15] H. Yamashita, P. Jayakumar, M. Alsaleh, and H. Sugiyama, "Physics-based deformable tire–soil interaction model for off-road mobility simulation and experimental validation," *Journal of Computational and Nonlinear Dynamics*, vol. 13, no. 2, p. 021002, 2018.

[16] K. Fukami, M. Ueno, K. Hashiguchi, and T. Okayasu, "Mathematical models for soil displacement under a rigid wheel," *Journal of Terramechanics*, vol. 43, no. 3, pp. 287–301, 2006.

[17] K. Saengprachatanarug, M. Ueno, Y. Komiya, and E. Taira, "Measurement of soil deformation at the ground contact surface of a traveling wheel," *Engineering in Agriculture, Environment and Food*, vol. 2, no. 1, pp. 14–23, 2008.

[18] S. Wakabayashi, H. Sato, and S.-I. Nishida, "Design and mobility evaluation of tracked lunar vehicle," *Journal of Terramechanics*, vol. 46, no. 3, pp. 105–114, 2009.

[19] J. Y. Wong, C. Senatore, P. Jayakumar, and K. Iagnemma, "Predicting mobility performance of a small, lightweight track system using the computer-aided method ntvpm," *Journal of Terramechanics*, vol. 61, pp. 23–32, 2015.

[20] J. B. Raymond and P. Jayakumar, "The shearing edge of tracked vehicle–soil interactions in path clearing applications utilizing multi-body dynamics modeling & simulation," *Journal of Terramechanics*, vol. 58, pp. 39–50, 2015.

[21] K. Liu, P. Ayers, H. Howard, A. Anderson, and J. Kane, "Multi-pass rutting study for turning wheeled and tracked vehicles," *Transactions of the ASABE*, vol. 54, no. 1, pp. 5–12, 2011.

[22] C. Li, P. B. Umbanhowar, H. Komsuoglu, D. E. Koditschek, and D. I. Goldman, "Sensitive dependence of the motion of a legged robot on granular media," *Proceedings of the National Academy of Sciences*, vol. 106, no. 9, pp. 3029–3034, 2009.

[23] P. Holmes, R. J. Full, D. Koditschek, and J. Guckenheimer, "The dynamics of legged locomotion: Models, analyses, and challenges," *SIAM review*, vol. 48, no. 2, pp. 207–304, 2006.

[24] F. Qian, T. Zhang, W. Korff, P. B. Umbanhowar, R. J. Full, and D. I. Goldman, "Principles of appendage design in robots and animals determining terradynamic performance on flowable ground," *Bioinspiration & biomimetics*, vol. 10, no. 5, p. 056014, 2015.

[25] C. Li, A. O. Pullin, D. W. Haldane, H. K. Lam, R. S. Fearing, and R. J. Full, "Terradynamically streamlined shapes in animals and robots enhance traversability through densely cluttered terrain," *Bioinspiration & biomimetics*, vol. 10, no. 4, p. 046003, 2015.

[26] R. Grandia, D. Pardo, and J. Buchli, "Contact invariant model learning for legged robot locomotion," *IEEE Robotics and Automation Letters*, vol. 3, no. 3, pp. 2291–2298, 2018.

[27] R. Armour, K. Paskins, A. Bowyer, J. Vincent, and W. Megill, "Jumping robots: a biomimetic solution to locomotion across rough terrain," *Bioinspiration & biomimetics*, vol. 2, no. 3, p. S65, 2007.

[28] A. Irawan and K. Nonami, "Optimal impedance control based on body inertia for a hydraulically driven hexapod robot walking on uneven and extremely soft terrain," *Journal of Field Robotics*, vol. 28, no. 5, pp. 690–713, 2011.

[29] J. Maciejewski and A. Jarzebowski, "Laboratory optimization of the soil digging process," *Journal of Terramechanics*, vol. 39, no. 3, pp. 161–179, 2002.

[30] H. Taghavifar and A. Mardani, "Applying a supervised ann (artificial neural network) approach to the prognostication of driven wheel energy efficiency indices," *Energy*, vol. 68, pp. 651–657, 2014.

[31] M. Mori, M. Fujishima, Y. Inamasu, and Y. Oda, "A study on energy efficiency improvement for machine tools," *CIRP annals*, vol. 60, no. 1, pp. 145–148, 2011.

[32] M. Sutoh, K. Nagaoka, K. Nagatani, and K. Yoshida, "Design of wheels with grousers for planetary rovers traveling over loose soil," *Journal of Terramechanics*, vol. 50, no. 5-6, pp. 345–353, 2013.

[33] J. Knappett, M. Brown, M. Bransby, P. Hudacsek, N. Morgan, D. Cathie, A. Maconochie, G. Yun, A. Ripley, N. Brown, *et al.*, "Capacity of grillage foundations under horizontal loading," *Géotechnique*, vol. 62, no. 9, pp. 811–823, 2012.

[34] R. Yong and A. Hanna, "Finite element analysis of plane soil cutting," *Journal of terramechanics*, vol. 14, no. 3, pp. 103–125, 1977.

[35] M. Naderi-Boldaji, R. Alimardani, A. Hemmat, A. Sharifi, A. Keyhani, M. Z. Tekeste, and T. Keller, "3d finite element simulation of a single-tip horizontal penetrometer–soil interaction. part i: Development of the model and evaluation of the model parameters," *Soil and Tillage Research*, vol. 134, pp. 153–162, 2013.

[36] M. O. Ciantia, M. Arroyo, J. Butlanska, and A. Gens, "Dem modelling of cone penetration tests in a double-porosity crushable granular material," *Computers and Geotechnics*, vol. 73, pp. 109–127, 2016.

[37] I. Shmulevich, Z. Asaf, and D. Rubinstein, "Interaction between soil and a wide cutting blade using the discrete element method," *Soil and Tillage Research*, vol. 97, no. 1, pp. 37–50, 2007.

[38] N. Phuong, A. Van Tol, A. Elkadi, and A. Rohe, "Numerical investigation of pile installation effects in sand using material point method," *Computers and Geotechnics*, vol. 73, pp. 58–71, 2016.

[39] R. Ambati, X. Pan, H. Yuan, and X. Zhang, "Application of material point methods for cutting process simulations," *Computational Materials Science*, vol. 57, pp. 102–110, 2012.

[40] P. Sonar, S. Modi, and I. Sharma, "Estimating forces during ploughing of a granular bed," *Journal of Fluid Mechanics*, vol. 875, pp. 376–410, 2019.

[41] J. Pratt, C.-M. Chew, A. Torres, P. Dilworth, and G. Pratt, "Virtual model control: An intuitive approach for bipedal locomotion," *The International Journal of Robotics Research*, vol. 20, no. 2, pp. 129–143, 2001.

[42] K. Konolige, "A gradient method for realtime robot control," in *Proceedings. 2000 IEEE/RSJ International Conference on Intelligent Robots and Systems (IROS 2000)(Cat. No. 00CH37113)*, vol. 1, pp. 639–646, IEEE, 2000.

[43] D. Negrut, A. Tasora, M. Anitescu, H. Mazhar, T. Heyn, and A. Pazouki, "Solving large multibody dynamics problems on the gpu," in *GPU Computing Gems Jade Edition*, pp. 269–280, Elsevier, 2012.

[44] E. McKyes, *Soil cutting and tillage*, vol. 7. Elsevier, 1985.

[45] R. Godwin and M. O'Dogherty, "Integrated soil tillage force prediction models," *Journal of Terramechanics*, vol. 44, no. 1, pp. 3–14, 2007.

[46] N. Meyer, A. Nernheim, and U. Köhler, "Geosynthetic-soil interaction under cyclic loading," in *3rd European Geosynthetics Conference, Munich, Germany*, vol. 103, pp. 635–639, 2004.

[47] G. Gottardi, G. Houlsby, and R. Butterfield, "Plastic response of circular footings on sand under general planar loading," *Géotechnique*, vol. 49, no. 4, pp. 453–470, 1999.

[48] G. Ishigami, A. Miwa, K. Nagatani, and K. Yoshida, "Terramechanics-based model for steering maneuver of planetary exploration rovers on loose soil," *Journal of Field robotics*, vol. 24, no. 3, pp. 233–250, 2007.

[49] R. Butterfield and K. Andrawes, "An air activated sand spreader for forming uniform sand beds," *Géotechnique*, vol. 20, no. 1, pp. 97–100, 1970.

[50] S. Miura and S. Toki, "A sample preparation method and its effect on static and cyclic deformation-strength properties of sand," *Soils and foundations*, vol. 22, no. 1, pp. 61–77, 1982.

[51] M. El Sawwaf and A. K. Nazir, "Behavior of repeatedly loaded rectangular footings resting on reinforced sand," *Alexandria Engineering Journal*, vol. 49, no. 4, pp. 349–356, 2010.

[52] M. Raghunandan, A. Juneja, and B. Hsiung, "Preparation of reconstituted sand samples in the laboratory," *International Journal of Geotechnical Engineering*, vol. 6, no. 1, pp. 125–131, 2012.

[53] C. Chen, Q. Quan, Z. Deng, and S. Jiang, "Vibratory compaction method for preparing lunar regolith drilling simulant," *Advances in Space Research*, vol. 58, no. 1, pp. 145–154, 2016.

[54] B. W. Byrne, *Investigations of suction caissons in dense sand*. PhD thesis, University of Oxford Oxford, UK, 2000.

[55] D. White, A. Barefoot, and M. Bolton, "Centrifuge modelling of upheaval buckling in sand," *International Journal of Physical Modelling in Geotechnics*, vol. 1, no. 2, pp. 19–28, 2001.

[56] K. Miura, K. Maeda, M. Furukawa, and S. Toki, "Mechanical characteristics of sands with different primary properties," *Soils and Foundations*, vol. 38, no. 4, pp. 159–172, 1998.

[57] D. L. Presti, S. Pedroni, and V. Crippa, "Maximum dry density of cohesionless soils by pluviation and by ASTM D 4253-83: A comparative study," *Geotechnical Testing Journal*, vol. 15, no. 2, pp. 180–189, 1992.

[58] B. Walker and T. Whitaker, "An apparatus for forming uniform beds of sand for model foundation tests," *Geotechnique*, vol. 17, no. 2, pp. 161–167, 1967.

[59] T. N. Dave and S. Dasaka, "Assessment of portable traveling pluviator to prepare reconstituted sand specimens," *Geomechanics and Engineering*, vol. 4, no. 2, pp. 79–90, 2012.

[60] C. Fretti, D. L. Presti, and S. Pedroni, "A pluvial deposition method to reconstitute well-graded sand specimens," *Geotechnical testing journal*, vol. 18, no. 2, pp. 292–298, 1995.

[61] C. Hariprasad, M. Rajashekhar, and B. Umashankar, "Preparation of uniform sand specimens using stationary pluviation and vibratory methods," *Geotechnical and Geological Engineering*, vol. 34, no. 6, pp. 1909–1922, 2016.

[62] B. Maillot, "A sedimentation device to produce uniform sand packs," *Tectonophysics*, vol. 593, pp. 85–94, 2013.

[63] Y. P. Vaid and D. Negussey, "Relative density of pluviated sand samples," *Soils and Foundations*, vol. 24, no. 2, pp. 101–105, 1984.

[64] N. S. Rad and M. T. Tumay, "Factors affecting sand specimen preparation by raining," *Geotechnical Testing Journal*, vol. 10, no. 1, pp. 31–37, 1987.

[65] J. Kolbuszewski, "An experimental study of the maximum and minimum porosities of sands," in *Proceedings of the 2nd international conference on soil mechanics and foundation engineering, Rotterdam*, vol. 1, pp. 158–165, 1948.

[66] Y. Vaid and D. Negussey, "Preparation of reconstituted sand specimens," in *Advanced triaxial testing of soil and rock*, ASTM International, 1988.

[67] R. W. Boulanger, C. J. Curras, B. L. Kutter, D. W. Wilson, and A. Abghari, "Seismic soil-pile-structure interaction experiments and analyses," *Journal of Geotechnical and Geoenvironmental Engineering*, vol. 125, no. 9, pp. 750–759, 1999.

[68] M. N. Hussien, T. Tobita, S. Iai, and M. Karray, "Soil-pile-structure kinematic and inertial interaction observed in geotechnical centrifuge experiments," *Soil Dynamics and Earthquake Engineering*, vol. 89, pp. 75–84, 2016.

[69] Y.-S. Fang, T.-J. Chen, and B.-F. Wu, "Passive earth pressures with various wall movements," *Journal of Geotechnical Engineering*, vol. 120, no. 8, pp. 1307–1323, 1994.

[70] F. Qian and D. I. Goldman, "The dynamics of legged locomotion in heterogeneous terrain: universality in scattering and sensitivity to initial conditions.," in *Robotics: Science and Systems*, pp. 1–9, 2015.

[71] C. Li, S. T. Hsieh, and D. I. Goldman, "Multi-functional foot use during running in the zebra-tailed lizard (callisaurus draconoides)," *Journal of Experimental Biology*, pp. jeb–061937, 2012.

[72] C. Li, T. Zhang, and D. I. Goldman, "A terradynamics of legged locomotion on granular media," *Science*, vol. 339, no. 6126, pp. 1408–1412, 2013.

[73] R. D. Maladen, Y. Ding, C. Li, and D. I. Goldman, "Undulatory swimming in sand: subsurface locomotion of the sandfish lizard," *science*, vol. 325, no. 5938, pp. 314–318, 2009.

[74] P. Umbanhowar and D. I. Goldman, "Granular impact and the critical packing state," *Physical Review E*, vol. 82, no. 1, p. 010301, 2010.

[75] D. Geldart, "Types of gas fluidization," *Powder technology*, vol. 7, no. 5, pp. 285–292, 1973.

[76] D. Geldart and A. R. Abrahamsen, "Homogeneous fluidization of fine powders using various gases and pressures," *Powder Technology*, vol. 19, no. 1, pp. 133–136, 1978.

[77] Z. Yang, Y. Tung, and M. Kwauk, "Characterizing fluidization by the bed collapsing method," *Chemical Engineering Communications*, vol. 39, no. 1-6, pp. 217–232, 1985.

[78] S. Ergun, "Fluid flow through packed columns," *Chem. Eng. Prog.*, vol. 48, pp. 89–94, 1952.

[79] F. Blake, "The resistance of packing to fluid flow," *Transactions of the American Institute of Chemical Engineers*, vol. 14, no. 3, pp. 415–421, 1922.

[80] S. P. Burke and W. Plummer, "Gas flow through packed columns1," *Industrial & Engineering Chemistry*, vol. 20, no. 11, pp. 1196–1200, 1928.

[81] J. Wu, B. Yu, and M. Yun, "A resistance model for flow through porous media," *Transport in Porous Media*, vol. 71, no. 3, pp. 331–343, 2008.

[82] I. Gasho, "Blower application basics." Website, 8 2009. last checked: 06.09.2019.

[83] F. Zenz, "Bubble formation and grid design," in *Institution of Chemical Engineers Symposium Series*, pp. 136–139, 1968.

[84] D. Geldart and J. Baeyens, "The design of distributors for gas-fluidized beds," *Powder Technology*, vol. 42, no. 1, pp. 67–78, 1985.

[85] ASTM:D4253-16, "Standard test methods for maximum index density and unit weight of soils using a vibratory table," *ASTM International, West Conshohocken, PA*, 2016.

[86] ASTM:D4254-16, "Standard test methods for minimum index density and unit weight of soils and calculation of relative density," *ASTM International, West Conshohocken, PA*, 2016.

[87] N. Brady and R. Weil, "Organisms and ecology of the soil," in *Nature and Properties of Soil*, vol. 11, (Prentice Hall, Upper Saddle River, New Jersey, USA), pp. 328–360, 1996.

[88] N. Gravish, P. B. Umbanhowar, and D. I. Goldman, "Force and flow at the onset of drag in plowed granular media," *Physical Review E*, vol. 89, no. 4, p. 042202, 2014.

[89] WES, "Trafficability of soils: Development of testing instruments," Tech. Rep. 3-240, U.S. Army Engineer Waterways Experiment Station, Vicksburg, MS, 1965.

[90] J. Mulqueen, J. Stafford, and D. Tanner, "Evaluation of penetrometers for measuring soil strength," *Journal of Terramechanics*, vol. 14, no. 3, pp. 137–151, 1977.

[91] S. Grunwald, B. Lowery, D. Rooney, and K. McSweeney, "Profile cone penetrometer data used to distinguish between soil materials," *Soil and Tillage Research*, vol. 62, no. 1-2, pp. 27–40, 2001.

[92] B. Coutermarsh, "Velocity effect of vehicle rolling resistance in sand," *Journal of Terramechanics*, vol. 44, no. 4, pp. 275–291, 2007.

[93] P. Ayers and H. Bowen, "Predicting soil density using cone penetration resistance and moisture profiles," *Transactions of the ASAE*, vol. 30, no. 5, pp. 1331–1336, 1987.

[94] H. J. Luth and R. D. Wismer, "Performance of plane soil cutting blades in sand," *Transactions of the ASAE*, vol. 14, no. 2, pp. 255–0259, 1971.

[95] J. Y. Wong, *Theory of ground vehicles*. John Wiley & Sons, 2008.

[96] A. Kumar, Y. Chen, M. A.-A. Sadek, and S. Rahman, "Soil cone index in relation to soil texture, moisture content, and bulk density for no-tillage and conventional tillage," *Agricultural Engineering International: CIGR Journal*, vol. 14, no. 1, pp. 26–37, 2012.

[97] P. Ayers and J. Perumpral, "Moisture and density effect on cone index," *Transactions of the ASAE*, vol. 25, no. 5, pp. 1169–1172, 1982.

[98] G. Pillinger, A. Géczy, Z. Hudoba, and P. Kiss, "Determination of soil density by cone index data," *Journal of Terramechanics*, vol. 77, pp. 69–74, 2018.

[99] D. R. Freitag, "A dimensional analysis of the performance of pneumatic tires on soft soils.," Tech. Rep. 3-688, U.S. Army Waterways Experiment Station, 1965.

[100] J.-Y. Wong and A. Reece, "Prediction of rigid wheel performance based on the analysis of soil-wheel stresses part i. performance of driven rigid wheels," *Journal of Terramechanics*, vol. 4, no. 1, pp. 81–98, 1967.

[101] S. Wu, J. Hu, and J. Wong, "Behaviour of soil under a lugged wheel," tech. rep., CARLETON UNIV OTTAWA (ONTARIO), 1984.

[102] L. R. Khot, V. M. Salokhe, H. Jayasuriya, and H. Nakashima, "Experimental validation of distinct element simulation for dynamic wheel–soil interaction," *Journal of Terramechanics*, vol. 44, no. 6, pp. 429–437, 2007.

[103] L. Ding, Z. Deng, H. Gao, K. Nagatani, and K. Yoshida, "Planetary rovers' wheel—soil interaction mechanics: new challenges and applications for wheeled mobile robots," *Intelligent Service Robotics*, vol. 4, no. 1, pp. 17–38, 2011.

[104] R. Bauer, W. Leung, and T. Barfoot, "Experimental and simulation results of wheel-soil interaction for planetary rovers," in *Intelligent Robots and Systems, 2005.(IROS 2005). 2005 IEEE/RSJ International Conference on*, pp. 586–591, IEEE, 2005.

[105] Y. Koren and Y. Koren, *Robotics for engineers*, vol. 168. McGraw-Hill New York et al, 1985.

[106] R. M. Murray, *A mathematical introduction to robotic manipulation*. CRC press, 2017.

[107] G. Gottardi and R. Butterfield, "On the bearing capacity of surface footings on sand under general planar loads," *Soils and Foundations*, vol. 33, no. 3, pp. 68–79, 1993.

[108] K. Georgiadis, "The influence of load inclination on the undrained bearing capacity of strip footings on slopes," *Computers and Geotechnics*, vol. 37, no. 3, pp. 311–322, 2010.

[109] J. B. Hansen, "A revised and extended formula for bearing capacity," 1970.

[110] A. S. Vesic, "Bearing capacity of shallow foundations," *Foundation Engineering Handbook.*, pp. 121–147, 1975.

[111] A. B. Vesic, "Bearing capacity of deep foundations in sand," *Highway research record*, no. 39, 1963.

[112] T. Kimura, O. Kusakabe, and K. Saitoh, "Geotechnical model tests of bearing capacity problems in a centrifuge," *Géotechnique*, vol. 35, no. 1, pp. 33–45, 1985.

[113] R. Butterfield and J. Ticof, "The use of physical models in design. discussion," *Proceedings 7th ECSMFE, Brighton*, vol. 4, pp. 259–261, 1979.

[114] G. Ricceri and P. Simonini, "Interaction diagrams for shallow footings on sand," in *Proceedings of the 12th International Conference on Soil Mechanics and Foundation Engineering, Rio de Janeiro*, pp. 13–18, 1989.

[115] D. Loukidis, T. Chakraborty, and R. Salgado, "Bearing capacity of strip footings on purely frictional soil under eccentric and inclined loads," *Canadian Geotechnical Journal*, vol. 45, no. 6, pp. 768–787, 2008.

[116] G. Houlsby and M. Cassidy, "A plasticity model for the behaviour of footings on sand under combined loading," *Géotechnique*, vol. 52, no. 2, pp. 117–129, 2002.

[117] M. Cassidy, B. Byrne, and G. Houlsby, "Modelling the behaviour of circular footings under combined loading on loose carbonate sand," *Géotechnique*, vol. 52, no. 10, 2002.

[118] B. Bienen, B. Byrne, G. Houlsby, and M. Cassidy, "Investigating six-degree-of-freedom loading of shallow foundations on sand," *Géotechnique*, vol. 56, no. 6, pp. 367–380, 2006.

[119] L. Govoni, S. Gourvenec, and G. Gottardi, "Centrifuge modelling of circular shallow foundations on sand," *International Journal of Physical Modelling in Geotechnics*, vol. 10, no. 2, pp. 35–46, 2010.

[120] C. Martin, "Exact bearing capacity calculations using the method of characteristics," *Proc. IACMAG. Turin*, pp. 441–450, 2005.

[121] J. Desrues and G. Viggiani, "Strain localization in sand: an overview of the experimental results obtained in grenoble using stereophotogrammetry," *International Journal for Numerical and Analytical Methods in Geomechanics*, vol. 28, no. 4, pp. 279–321, 2004.

[122] M. Niedostatkiewicz, D. Lesniewska, and J. Tejchman, "Experimental analysis of shear zone patterns in cohesionless for earth pressure problems using particle image velocimetry," *Strain*, vol. 47, pp. 218–231, 2011.

[123] R. I. Borja and J. E. Andrade, "Critical state plasticity. part vi: Meso-scale finite element simulation of strain localization in discrete granular materials," *Computer Methods in Applied Mechanics and Engineering*, vol. 195, no. 37-40, pp. 5115–5140, 2006.

[124] J. Tejchman, *Shear localization in granular bodies with micro-polar hypoplasticity*. Springer Science & Business Media, 2008.

[125] J. Tejchman and J. Górski, "Computations of size effects in granular bodies within micro-polar hypoplasticity during plane strain compression," *International Journal of Solids and Structures*, vol. 45, no. 6, pp. 1546–1569, 2008.

[126] K. A. Alshibli, M. I. Alsaleh, and G. Z. Voyiadjis, "Modelling strain localization in granular materials using micropolar theory: numerical implementation and verification," *International journal for numerical and analytical methods in geomechanics*, vol. 30, no. 15, pp. 1525–1544, 2006.

[127] M. Gutierrez and I. Vardoulakis, "Energy dissipation and post-bifurcation behaviour of granular soils," *International journal for numerical and analytical methods in geomechanics*, vol. 31, no. 3, pp. 435–455, 2007.

[128] I. Vardoulakis, "Bifurcation analysis of the triaxial test on sand samples," *Acta Mechanica*, vol. 32, no. 1-3, pp. 35–54, 1979.

[129] J. Desrues, R. Chambon, M. Mokni, and F. Mazerolle, "Void ratio evolution inside shear bands in triaxial sand specimens studied by computed tomography," *Géotechnique*, vol. 46, no. 3, pp. 529–546, 1996.

[130] J. Sulem and I. Vardoulakis, *Bifurcation analysis in geomechanics*. CRC Press, 1995.

[131] I. Vardoulakis and B. Graf, "Calibration of constitutive models for granular materials using data from biaxial experiments," *Géotechnique*, vol. 35, no. 3, pp. 299–317, 1985.

[132] J. Desrues, "Shear band initiation in granular materials: experimentation and theory," *Geomaterials Constitutive Equations and Modelling*, pp. 283–310, 1990.

[133] T. Yoshida, "Shear banding in sands observed in plane strain compression," *Localization and Bifurcation Theory for Soils and Rock*, pp. 165–179, 1995.

[134] W. W. Harris, G. Viggiani, M. A. Mooney, and R. J. Finno, "Use of stereophotogrammetry to analyze the development of shear bands in sand," *Geotechnical Testing Journal*, vol. 18, no. 4, pp. 405–420, 1995.

[135] R. J. Finno, W. Harris, M. A. Mooney, and G. Viggiani, "Shear bands in plane strain compression of loose sand," *Geotechnique*, vol. 47, no. 1, pp. 149–165, 1997.

[136] G. Scarpelli and D. Wood, "Experimental observations of shear band patterns in direct shear tests," in *Proc. IUTAM Conf. Def. and Failure of Gran. Materials*, p. 473–484, Balkema, 1982.

[137] P. Lade, J. A. Yamamuro, and B. D. Skyers, "Effects of shear band formation in triaxial extension tests," *Geotechnical Testing Journal*, vol. 19, no. 4, pp. 398–410, 1996.

[138] A. Saada, L. Liang, J. Figueroa, and C. Cope, "Bifurcation and shear band propagation in sands," *Geotechnique*, vol. 49, no. 3, pp. 367–385, 1999.

[139] N. Gravish, P. B. Umbanhowar, and D. I. Goldman, "Force and flow transition in plowed granular media," *Physical review letters*, vol. 105, no. 12, p. 128301, 2010.

[140] K. Roscoe, "The determination of strains in soils by an x-ray method," *Civ. Engng Publ. Wks Rev.*, vol. 58, pp. 873–876, 1963.

[141] G. Milligan, *The Behaviour of Rigid and Flexible Retaining Walls in Sand.* PhD thesis, University of Cambridge, 1974.

[142] E. Andò, S. Hall, G. Viggiani, J. Desrues, and P. Bésuelle, "Experimental micromechanics: grain-scale observation of sand deformation," 2012.

[143] S.-A. Tan and T.-F. Fwa, "Influence of voids on density measurements of granular materials using gamma radiation techniques," *Geotechnical Testing Journal*, vol. 14, no. 3, pp. 257–265, 1991.

[144] R. Butterfield, R. Harkness, and K. Andrews, "A stero-photogrammetric method for measuring displacement fields," *Geotechnique*, vol. 20, no. 3, pp. 308–314, 1970.

[145] J. Desrues, R. Chambon, M. Mokni, and F. Mazerolle, "Void ratio evolution inside shear bands in triaxial sand specimens studied by computed tomography," *Géotechnique*, vol. 46, no. 3, pp. 529–546, 1996.

[146] A. J. Jaworski and T. Dyakowski, "Application of electrical capacitance tomography for measurement of gas-solids flow characteristics in a pneumatic conveying system," *Measurement Science and Technology*, vol. 12, no. 8, p. 1109, 2001.

[147] M. Niedostatkiewicz, J. Tejchman, Z. Chaniecki, and K. Grudzień, "Determination of bulk solid concentration changes during granular flow in a model silo with ect sensors," *Chemical Engineering Science*, vol. 64, no. 1, pp. 20–30, 2009.

[148] T. Chu, W. Ranson, and M. A. Sutton, "Applications of digital-image-correlation techniques to experimental mechanics," *Experimental mechanics*, vol. 25, no. 3, pp. 232–244, 1985.

[149] D. White, W. Take, and M. Bolton, "Soil deformation measurement using particle image velocimetry (piv) and photogrammetry," *Geotechnique*, vol. 53, no. 7, pp. 619–631, 2003.

[150] A. L. Rechenmacher and R. J. Finno, "Digital image correlation to evaluate shear banding in dilative sands," *Geotechnical Testing Journal*, vol. 27, no. 1, pp. 13–22, 2003.

[151] D. Lesniewska and D. M. Wood, "Observations of stresses and strains in a granular material," *Journal of engineering mechanics*, vol. 135, no. 9, pp. 1038–1054, 2009.

[152] K. Roscoe, "The stability of short pier foundations in sand," *British Welding Journal*, pp. 343–354, 1956.

[153] R. Butterfield and G. Gottardi, "A complete three-dimensional failure envelope for shallow footings on sand," *Géotechnique*, vol. 44, no. 1, pp. 181–184, 1994.

[154] C. Martin and G. Houlsby, "Combined loading of spudcan foundations on clay: laboratory tests," *Géotechnique*, vol. 50, no. 4, pp. 325–338, 2000.

[155] C. M. Martin, *Physical and numerical modelling of offshore foundations under combined loads*. PhD thesis, Oxford University, UK, 1994.

[156] B. W. Byrne and G. T. Houlsby, "Experimental investigations of the response of suction caissons to transient combined loading," *Journal of geotechnical and geoenvironmental engineering*, vol. 130, no. 3, pp. 240–253, 2004.

[157] M. Cassidy, B. Byrne, and M. Randolph, "A comparison of the combined load behaviour of spudcan and caisson foundations on soft normally consolidated clay," *Géotechnique*, vol. 54, no. 2, pp. 91–106, 2004.

[158] F. A. Villalobos, B. W. Byrne, and G. T. Houlsby, "An experimental study of the drained capacity of suction caisson foundations under monotonic loading for offshore applications," *Soils and foundations*, vol. 49, no. 3, pp. 477–488, 2009.

[159] H. G. Poulos and E. H. Davis, *Pile foundation analysis and design*. No. Monograph, 1980.

[160] G. Meyerhof and V. Sastry, "Bearing capacity of rigid piles under eccentric and inclined loads," *Canadian Geotechnical Journal*, vol. 22, no. 3, pp. 267–276, 1985.

[161] G. Meyerhof, "Behaviour of pile foundations under special loading conditions: 1994 rm hardy keynote address," *Canadian geotechnical journal*, vol. 32, no. 2, pp. 204–222, 1995.

[162] F. S. C. Tan, *Centrifuge and theoretical modelling of conical footings on sand.* PhD thesis, University of Cambridge, 1990.

[163] M. Bransby and M. Randolph, "Combined loading of skirted foundations," *Géotechnique*, vol. 48, no. 5, pp. 637–655, 1998.

[164] H. Taiebat and J. Carter, "A failure surface for circular footings on cohesive soils," *Géotechnique*, vol. 60, no. 4, pp. 265–273, 2010.

[165] Z. Shen, S. Bie, and L. Guo, "Undrained capacity of a surface circular foundation under fully three-dimensional loading," *Computers and Geotechnics*, vol. 92, pp. 57–67, 2017.

[166] J. Hambleton and A. Drescher, "Modeling wheel-induced rutting in soils: Rolling," *Journal of Terramechanics*, vol. 46, no. 2, pp. 35–47, 2009.

[167] B. Pan, H. Xie, Z. Guo, and T. Hua, "Full-field strain measurement using a two-dimensional savitzky-golay digital differentiator in digital image correlation," *Optical Engineering*, vol. 46, no. 3, p. 033601, 2007.

[168] B. Pan, K. Qian, H. Xie, and A. Asundi, "Two-dimensional digital image correlation for in-plane displacement and strain measurement: a review," *Measurement science and technology*, vol. 20, no. 6, p. 062001, 2009.

[169] T. Belytschko, Y. Y. Lu, and L. Gu, "Element-free galerkin methods," *International journal for numerical methods in engineering*, vol. 37, no. 2, pp. 229–256, 1994.

[170] P. Lancaster and K. Salkauskas, "Surfaces generated by moving least squares methods," *Mathematics of computation*, vol. 37, no. 155, pp. 141–158, 1981.

[171] E. Hamm, F. Tapia, and F. Melo, "Dynamics of shear bands in a dense granular material forced by a slowly moving rigid body," *Physical Review E*, vol. 84, no. 4, p. 041304, 2011.

[172] K. A. Murphy, K. A. Dahmen, and H. M. Jaeger, "Transforming mesoscale granular plasticity through particle shape," *Physical Review X*, vol. 9, no. 1, p. 011014, 2019.

[173] E. Kashizadeh, "Theoretical and experimental analysis of the cutting process in sand," *MPhil Thesis*, 2018.

[174] W.-F. Chen, *Limit analysis and soil plasticity*. Elsevier, 2013.

[175] E. Kashizadeh, J. Hambleton, and S. Stanier, "A numerical approach for modelling the ploughing process in sands," *Analytical Methods in Petroleum Upstream Applications*, p. 159, 2015.

[176] A. Drescher, I. Vardoulakis, and C. Han, "A biaxial apparatus for testing soils," *Geotechnical Testing Journal*, vol. 13, no. 3, pp. 226–234, 1990.

[177] C. Han and A. Drescher, "Shear bands in biaxial tests on dry coarse sand," *Soils and Foundations*, vol. 33, no. 1, pp. 118–132, 1993.

[178] Z. Jin and J. P. Hambleton, "Simulation of the cutting process in softening and hardening soils," *Geotechnical Special Publication*, vol. 2019, no. GSP 310, pp. 11–19, 2019.

[179] D. M. Wood and K. Belkheir, "Strain softening and state parameter for sand modelling," *Geotechnique*, vol. 44, no. 2, pp. 335–339, 1994.

[180] M. Bolton, "Strength and dilatancy of sands," *Geotechnique*, vol. 36, no. 1, pp. 65–78, 1986.

[181] F. Han, E. Ganju, R. Salgado, and M. Prezzi, "Effects of interface roughness, particle geometry, and gradation on the sand–steel interface friction angle," *Journal of Geotechnical and Geoenvironmental Engineering*, vol. 144, no. 12, p. 04018096, 2018.

[182] Z. Shi, M. Huang, and J. P. Hambleton, "Possibilities and limitations of the sequential kinematic method for simulating evolutionary plasticity problems," *Computers and Geotechnics (under review)*, 2021.

[183] D. Johnson, "Yield-line analysis by sequential linear programming," *International Journal of Solids and Structures*, vol. 32, no. 10, pp. 1395–1404, 1995.

[184] G. Milani and P. B. Lourenço, "A discontinuous quasi-upper bound limit analysis approach with sequential linear programming mesh adaptation," *International Journal of Mechanical Sciences*, vol. 51, no. 1, pp. 89–104, 2009.

[185] J. Hambleton and S. Sloan, "A perturbation method for optimization of rigid block mechanisms in the kinematic method of limit analysis," *Computers and Geotechnics*, vol. 48, pp. 260–271, 2013.

[186] J. Maciejewski and A. Jarz e̛bowski, "Application of kinematically admissible solutions to passive earth pressure problems," *International Journal of Geomechanics*, vol. 4, no. 2, pp. 127–136, 2004.

[187] M. ApS, "Mosek optimization toolbox for matlab," *User's Guide and Reference Manual, Version*, vol. 4, 2019.

[188] V. Murthy, "Principles and practices of soil mechanics and foundation engineering," *New York: Marcek Decker INC*, 2002.

[189] D. M. Wood, *Geotechnical modelling*. CRC Press, 2014.

[190] A. Drescher and E. Detournay, "Limit load in translational failure mechanisms for associative and non-associative materials," *Geotechnique*, vol. 43, no. 3, pp. 443–456, 1993.

[191] G. T. Houlsby and A. M. Puzrin, *Principles of hyperplasticity: an approach to plasticity theory based on thermodynamic principles*. Springer Science & Business Media, 2007.

[192] M. Cassidy, C. Gaudin, M. Randolph, P. Wong, D. Wang, and Y. Tian, "A plasticity model to assess the keying of plate anchors," *Géotechnique*, vol. 62, no. 9, p. 825, 2012.

[193] M. O'Neill, M. Bransby, and M. Randolph, "Drag anchor fluke soil interaction in clays," *Canadian Geotechnical Journal*, vol. 40, no. 1, pp. 78–94, 2003.

[194] R. Nova and L. Montrasio, "Settlements of shallow foundations on sand," *Géotechnique*, vol. 41, no. 2, pp. 243–256, 1991.

[195] C. Martin and G. Houlsby, "Combined loading of spudcan foundations on clay: numerical modelling," *Géotechnique*, vol. 51, no. 8, pp. 687–699, 2001.

[196] S. Grange, P. Kotronis, and J. Mazars, "A macro-element to simulate 3d soil–structure interaction considering plasticity and uplift," *International Journal of Solids and Structures*, vol. 46, no. 20, pp. 3651–3663, 2009.

[197] C. Cremer, A. Pecker, and L. Davenne, "Modelling of nonlinear dynamic behaviour of a shallow strip foundation with macro-element," *Journal of Earthquake Engineering*, vol. 6, no. 02, pp. 175–211, 2002.

[198] S. W. Sloan, "Substepping schemes for the numerical integration of elastoplastic stress–strain relations," *International journal for numerical methods in engineering*, vol. 24, no. 5, pp. 893–911, 1987.

[199] J. Simo and R. Taylor, "A return mapping algorithm for plane stress elastoplasticity," *International Journal for Numerical Methods in Engineering*, vol. 22, no. 3, pp. 649–670, 1986.

[200] H. Taiebat and J. Carter, "Numerical studies of the bearing capacity of shallow foundations on cohesive soil subjected to combined loading," *Géotechnique*, vol. 50, no. 4, pp. 409–418, 2000.

[201] A. M. Page, G. Grimstad, G. R. Eiksund, and H. P. Jostad, "A macro-element pile foundation model for integrated analyses of monopile-based offshore wind turbines," *Ocean Engineering*, vol. 167, pp. 23–35, 2018.

[202] Z. Li, P. Kotronis, and S. Escoffier, "Numerical study of the 3d failure envelope of a single pile in sand," *Computers and Geotechnics*, vol. 62, pp. 11–26, 2014.

[203] Y. Tian and M. J. Cassidy, "Modeling of pipe–soil interaction and its application in numerical simulation," *International Journal of Geomechanics*, vol. 8, no. 4, pp. 213–229, 2008.

[204] H. T. Durgunoglu and J. K. Mitchell, "Static penetration resistance of soils," 1973.

[205] Z. Li, P. Kotronis, S. Escoffier, and C. Tamagnini, "Macroelement modeling for single vertical piles," 2015.

[206] R. W. Bell, "The analysis of offshore foundations subjected to combined loading," 1991.

[207] T. Lu, *Failure envelopes for an embeded plate in plastic material obeying associated and non-associated flow rules*. PhD thesis, Northwestern University, 2018.

[208] L. Anand and C. Gu, "Granular materials: constitutive equations and strain localization," *Journal of the Mechanics and Physics of Solids*, vol. 48, no. 8, pp. 1701–1733, 2000.

[209] M. A. Sutton, S. R. McNeill, J. Jang, and M. Babai, "Effects of subpixel image restoration on digital correlation error estimates," *Optical Engineering*, vol. 27, no. 10, p. 271070, 1988.

[210] H. Bruck, S. McNeill, M. A. Sutton, and W. Peters, "Digital image correlation using newton-raphson method of partial differential correction," *Experimental mechanics*, vol. 29, no. 3, pp. 261–267, 1989.

[211] P. Zhou and K. E. Goodson, "Subpixel displacement and deformation gradient measurement using digital image/speckle correlation," *Optical Engineering*, vol. 40, no. 8, pp. 1613–1621, 2001.

[212] P. Bing, X. Hui-Min, X. Bo-Qin, and D. Fu-Long, "Performance of sub-pixel registration algorithms in digital image correlation," *Measurement Science and Technology*, vol. 17, no. 6, p. 1615, 2006.

[213] H. Lu and P. Cary, "Deformation measurements by digital image correlation: implementation of a second-order displacement gradient," *Experimental mechanics*, vol. 40, no. 4, pp. 393–400, 2000.

[214] S. A. Stanier, J. Blaber, W. A. Take, and D. White, "Improved image-based deformation measurement for geotechnical applications," *Canadian Geotechnical Journal*, vol. 53, no. 5, pp. 727–739, 2015.

[215] B. Pan, "Reliability-guided digital image correlation for image deformation measurement," *Applied optics*, vol. 48, no. 8, pp. 1535–1542, 2009.

[216] H. W. Schreier and M. A. Sutton, "Systematic errors in digital image correlation due to undermatched subset shape functions," *Experimental Mechanics*, vol. 42, no. 3, pp. 303–310, 2002.

[217] Y. Chen, J. Lee, and A. Eskandarian, *Meshless methods in solid mechanics*. Springer Science & Business Media, 2006.

[218] J. Dolbow and T. Belytschko, "An introduction to programming the meshless element f reegalerkin method," *Archives of computational methods in engineering*, vol. 5, no. 3, pp. 207–241, 1998.

[219] Z. Jin, J. Tang, P. B. Umbanhowar, and J. Hambleton, "Preparation of sand beds using fluidization," 2019.

APPENDIX A

# Strain measurement for observing localization using particle image velocimetry

## A.1. Introduction

Strain localization into zones, such as shear banding, is a fundamental phenomenon commonly observed in soils, which can lead to global failure of geotechnical structures, such as human-built embankments, footings, and retaining walls [**208, 123**]. The localization might appear as single, multiple, or pattern of shear zones depending on both initial and boundary conditions [**121**]. The zone of localization can be plane or curved, and both shear and volumetric deformation can occur [**122**]. Knowledge of the pattern of shear zones and distribution of shear and volumetric strain in the zones is vital for understanding the mechanism of soil deformation and developing either theoretical or numerical models [**123, 124, 125, 126, 127**].

Different techniques have been used to visualize deformation in soils in various laboratory tests: colored layers and markers [**133**], X-rays [**140, 141, 142**], $\gamma$-rays [**143**], stereophotogrammetry [**144, 121, 145**], electrical capacitance tomography [**146, 147**], and digital image correlation (DIC) or particle image velocimetry (PIV) [**148, 149, 150, 151**]. Among these methods, PIV is an optical non-invasive technique, which is implemented by comparing successive pairs of deforming specimen's digital photographs. The method enables

the estimations of the displacements at user-defined discrete positions for each pair of photographs, and then the strains (i.e., gradients of the displacements) are generally determined by differentiating the displacement field.

Many efforts have been devoted to improving the accuracy of the displacement estimation in PIV/DIC [**209, 210, 211, 212, 213, 214**] to enhance the measurement of strain field. However, the actual displacement field of the tested object cannot be perfectly restored due to the unavoidable influence of noise. In instances where strains are directly computed by differentiating the displacement field, the noises/errors might be even amplified. For example, if the error of displacement is $\pm 0.02$ pixels (the universally accepted displacement estimation accuracy of DIC [**167**]), and the subset size is 20 pixels, the error of strain calculated by forward difference is 0.2%. An error of this extent might hide the underlying strain information and limit the observation of strain localization.

Rather than improving the estimation of displacements, the objective of this study is to present a simple and effective technique to extract strain distribution from the displacement field obtained by PIV. The main idea of the method is to use moving least square (MLS) interpolants [**170**] to fit the displacement fields on local domains of the finite element mesh, then compute the strains by taking derivatives of these interpolants. In this appendix, the implementation of strain field measurement is described firstly, followed by a discussion about the critical parameter selection in the technique. Then virtual tests and a physical test involving strain localization are performed, and strain fields are calculated to validate the effectiveness of the proposed method.

## A.2. Procedure of strain field measurement

This section illustrates the method and implementation for measuring the strain field, including the estimation of the displacement field and the calculation of strains from the estimated displacements at discrete positions.

### A.2.1. Computation of displacement field

In a typical PIV-DIC analysis, a region of interest (ROI) is first defined within the initial ("reference") image of the model and populated with a mesh of subsets of user-defined size. The displacement of these subsets in subsequent ("target") images are found based on their cross-correlation. The integer pixel displacements can be obtained from the calculation of cross-correlation, and then subpixel displacements are determined by interpolating the correlation peak.

In this study, the displacement field is estimated by using the GeoPIV-RG [**214**], which is a free MATLAB-designed image analysis module for geotechnical and structural engineering research. The overarching framework controlling the computation process is the reliability-guided (RG) method proposed by Pan [**215**]. Each reference subset is allowed to deform using a shape function describing first-order deformations in conjunction with image-intensity interpolation techniques to improve the correlation between the reference and target subsets via optimization [**216**]. An initial "seed" subset is first analyzed, and then the subsequent computations are preconditioned using the results from the previously computed neighboring subset that has the highest correlation. The reference image is updated when the correlation coefficient for either the seed or one of the subsets contravenes user-defined thresholds. In this way, the displacements of the user-defined subsets in the whole process are calculated.

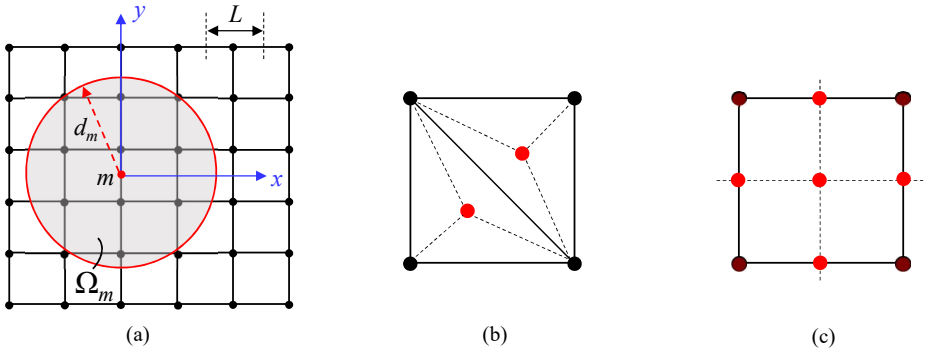


Figure A1. (a) Finite element mesh with a generic point $m$, and the local support domain $\Omega_m$ shaded; (b) configuration for calculating strains with triangular element used in GeoPIV_RG; (c) configuration for calculating strains by MLS method. Note red points and black points indicate the positions at which the strains and displacements are calculated, respectively.

It is demonstrated that the GeoPIV-RG allows improved deformation measurements for geotechnical applications with the evidence that rigid-body displacements can be detected to a precision of 0.001 px.

### A.2.2. Calculation of strain field by using MLS interpolants

The main idea of this method is to use MLS interpolants [**170**] to fit the displacement fields on local domains of the element mesh. The strains are then extracted by taking derivatives of these interpolants. The details are described as follows.

To calculate the derivative at any point $m$ (with coordinates $\mathbf{x}_m$) in the whole domain, a local domain $\Omega_m$ is defined with the origin at $m$ and local coordinates $x$ and $y$, as shown in Figure A1(a). The radius of the domain is $d_m$, and only nodes inside $\Omega_m$ contribute to evaluation of the interpolation of the displacement field. The displacement field is approximated by a polynomial function with order $k$:

$$u(\mathbf{x}) \approx \hat{u}(\mathbf{x}) = \sum_{j=1}^{k} p_i(\mathbf{x}) a_i(\mathbf{x}) = \mathbf{p}^T(\mathbf{x})\mathbf{a}(\mathbf{x}) \tag{A.1}$$

where $\mathbf{p}$ is a basis and $\mathbf{p}^T = [1xy]$ for a linear basis in two dimensions. In MLS, the unknown coefficients in $\mathbf{a}$ are determined by minimizing a function $J$, which sums up the weighted error of squared displacement for all nodes inside the support domain:

$$J(\mathbf{a}(\mathbf{x})) = \sum_{i=1}^{n} W(\mathbf{x} - \mathbf{x}_i)(\hat{u}_i - u_i)^2 = \sum_{i=1}^{n} W(\mathbf{x} - \mathbf{x}_i)(\mathbf{p}^T(\mathbf{x}_i)\mathbf{a}(\mathbf{x}) - u_i)^2 \tag{A.2}$$

where $W$ is a weight function; $i$ identifies the number of nodes in the local domain $\Omega_m$; $u_i$ refers to the displacement at $\mathbf{x} = \mathbf{x}_i$. Function $J$ is minimized by differentiating it with respect to the unknown coefficients $\mathbf{a}(\mathbf{x})$:

$$\frac{\partial J}{\partial \mathbf{a}} = \mathbf{0} \tag{A.3}$$

which leads to the following equation:

$$\mathbf{A}(\mathbf{x})\mathbf{a}(\mathbf{x}) = \mathbf{B}(\mathbf{x})\mathbf{U}(\mathbf{x}) \tag{A.4}$$

where the matrix are given by

$$\begin{aligned}
&\mathbf{A}(\mathbf{x}) = \sum_{i=1}^{n} W(\mathbf{x} - \mathbf{x}_i)(\mathbf{p}(\mathbf{x}_i)\mathbf{p}^T(\mathbf{x}_i) \\
&\mathbf{B}(\mathbf{x}) = [W(\mathbf{x} - \mathbf{x}_1)(\mathbf{p}(\mathbf{x}_1) \quad W(\mathbf{x} - \mathbf{x}_2)(\mathbf{p}(\mathbf{x}_2) \quad ... \quad W(\mathbf{x} - \mathbf{x}_n)(\mathbf{p}(\mathbf{x}_n)] \\
&\mathbf{U}^T(\mathbf{x}) = [u_1 \quad u_2 \quad ... \quad u_n]
\end{aligned} \tag{A.5}$$

The coefficients in **a** are determined as:

$$\mathbf{a(x)} = \mathbf{A}^{-1}(\mathbf{x})\mathbf{B}(\mathbf{x})\mathbf{U}(\mathbf{x}) \tag{A.6}$$

Then, the derivatives, i.e. strains, are given by $\hat{u}_{,x} = a_2$ and $\hat{u}_{,y} = a_3$ (for the case of a linear basis). The same procedure is adopted for calculating the strain at any point in the full field to obtain the strain distribution. It is noted that the positions at which one performs the strain calculation are not constrained by the grid/subsets set for estimating displacements.

In the calculation, the weight function ($W$) plays an important role. A properly constructed weight function, which can give unique solutions when determining the unknown coefficients **a**, should have three features: (1) it has compact support, meaning that its magnitude should be zero outside the support domain; (2) it should be positive for all nodes within the support domain; (3) it has its maximum value at the selected point and decreases monotonically when moving outwards. There are various functions satisfying the above properties [**217, 218**], and the cubic spline weight function described by Dolbow and Belytschko [**218**] is used in this study:

$$W(\mathbf{x}-\mathbf{x}_i) \equiv W(r) = \begin{cases} 2/3 - 4r^2 + 4r^3 & \text{for} \quad r \leq 1/2 \\ 4/3 - 4r + 4r^2 - 4r^3/3 & \text{for} \quad 1/2 < r < 1 \\ 0 & \text{for} \quad r > 1 \end{cases} \tag{A.7}$$

where $r = d_i/d_m$, $d_i = |\mathbf{x} - \mathbf{x}_i|$, and $d_m$ is the size of the local support domain, as shown in Figure A1(a).

### A.2.3. Selection of the local support domain size

The size of the local support domain, $d_m$, is a key factor influencing the calculation result. A support domain with a large size contains more data points (nodal displacements) to complete the local fitting. Thus, the influence of noise in the displacement field on the strain calculation is weakened, and naturally, the smoothness of the strain field will be improved. However, if the size is too large, the values of strain at neighboring positions tend to be equal, resulting in an over-smoothed strain field.

To specifically show the influence of $d_m$ on the accuracy of strain calculation, sets of artificial images representing deformation with strain localization are employed and analyzed with using various $d_m$. The artificial images are used since they can be subjected to precisely prescribed deformations and avoid the problems induced by camera lens distortions and camera-target movements [**214**]. As shown in Figure A2(a)-(b), the reference image is generated in MATLAB by randomly projecting 20000 black dots on a white background with a size of $1000 \times 1000$ pixels (px). Then, the deformation of simple shear is imposed in a zone at the mid of the image to create the deformed image. The width of the shear band is 100 px, and the magnitude of the imposed shear strain ($\gamma_{xy}$) ranges from 0.25% to 5%. In the analysis of the displacement field, the subset size ($L$) is set to be 25 px. For the generated images, the minimum standard deviation of the subset intensities ($\sigma_{Is}$) is examined to be 31, which satisfies the requirements on the contrast of subsets [**214**]. Based on the estimated displacement field, the strains are calculated by using the MLS method with adopting various $d_m$. The positions performing the strain calculation are indicated schematically by the red points in Figure A1(c), where the black points represent the center of subsets, at which the displacements are estimated.

The accuracy of the strain measurement is quantified by the normalized mean absolute errors, $NMAE_X$, calculated as $NMAE_X = MAE/X$, where $MAE$ is the mean absolute difference between the theoretical and calculated strains over the full field, and $X$ is the magnitude of the strain imposed in the localized zone. Figure A2(c) presents the change of $NMAE_{\gamma_{xy}}$ with the size of the local support domain as different shear strains are imposed. For the cases in which the shear strain is relatively large ($\gamma_{xy} = 1\%$, $5\%$), $NMAE_{\gamma_{xy}}$ almost keeps constant at first, and then increases monotonically with increaseing $d_m/L$. When a small shear strain is imposed ($\gamma_{xy} = 0.25\%$, $0.5\%$, $0.75\%$), the $NMAE_{\gamma_{xy}}$ decreases firstly, followed by an increase with the $d_m/L$. Besides, the figure indicates that as the imposed shear strain decreases, the $d_m/L$ generating the minimum $NMAE_{\gamma_{xy}}$ increases, which suggests that a larger $d_m$ is preferred when the shear strain to be measured is small. Overall, it is illustrated that a proper local support domain size should be selected carefully for observing the strain localization accurately in practice, and the above result can provide a reference on the selection.

## A.3. Experimental evaluation and results

In this section, virtual tests and a physical test are performed to verify the effectiveness of the MLS method.

### A.3.1. Virtual test

For performing virtual tests, a reference image with a size of $2000 \times 1000$ px is firstly generated by projecting 40000 black dots on a white background, which is shown in Figure A3(a). Then, the deformed image is created by imposing the deformation of simple shear and/or compaction on a shear band with a width of 100 px (shown in Figure A3(b)). The angle

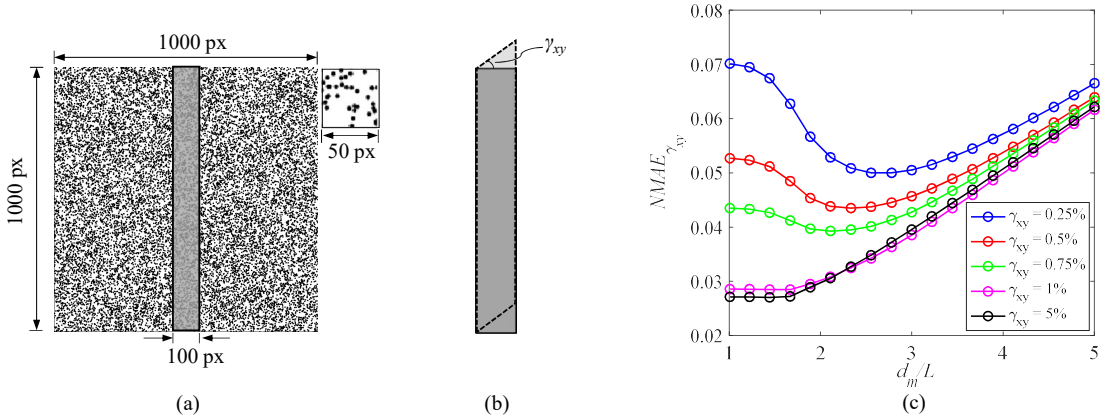


Figure A2. Evaluation of the influence of local support domain size ($d_m$) on the calculation accuracy: (a) artificial image and grey shade indicates the zone imposing strain localization; (b) imposed simple shear deformation in the localized area; (c) normalized mean absolute errors of the calculated shear strains with using different local support domain size.

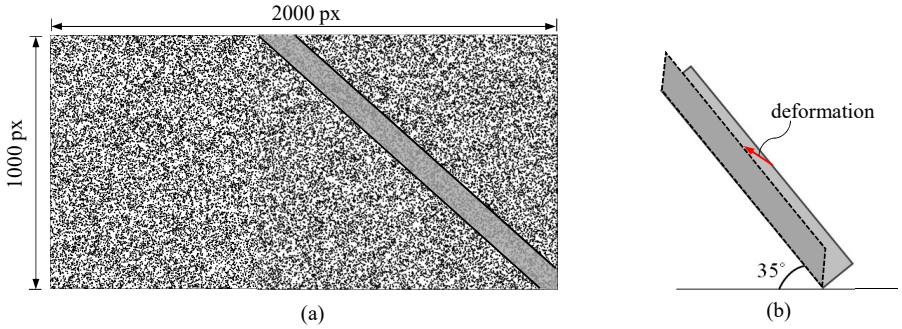


Figure A3. Artificial image and imposed deformations: (a) reference image and the grey shade indicates the zone imposing strain localization; (b) simple shear combined with compaction in the localized zone.

between the shear band and the horizontal is 35°. For a pair of images, the strain field is calculated by using both GeoPIV_RG and MLS interpolants. The configurations adopted to perform the calculations in the two methods are schematically described in Figure A1(b)-(c). In this section, the full-field maximum shear stain ($\gamma_{max}$) and volumetric strain ($\epsilon_v$) are evaluated to interpret the results.

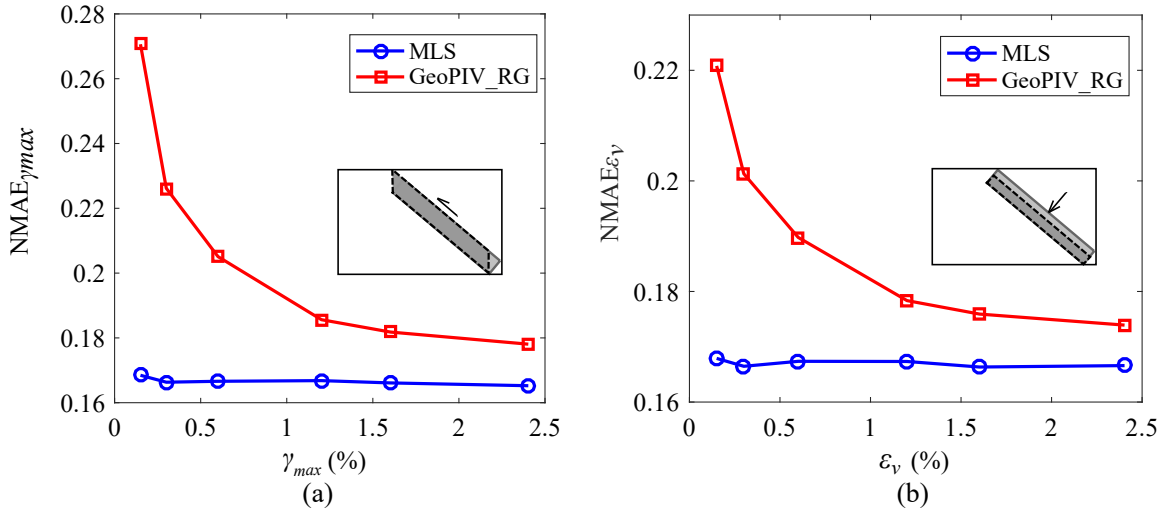


Figure A4. Normalized mean absolute error of (a) maximum shear strains as only simple shear is imposed on the shear band with various magnitudes; (b) volumetric strains as only compaction is imposed on the shear band with different magnitudes.

To quantitatively compare the performance of the methods (MLS and the one used in GeoPIV_RG), test images representing two types of deformation are employed: (1) simple shear is exclusively imposed on the shear band with various magnitudes, and (2) compaction is induced at different magnitudes on the shear band without shear. Figure A4(a)-(b) show the evolution of $NMAE_{\gamma_{xy}}$ and $NMAE_{\epsilon_v}$ with the imposed $\gamma_{xy}$ and $\epsilon_v$, respectively. For both cases, the $NMAE$ of strains calculated by the MLS method is smaller than that measured by GeoPIV_RG. The smaller the imposed strain is, the bigger the difference of $NMAE$ obtained from the two methods, and more effective the MLS method is.

We also plot the calculated strain fields (Figure A5 and Figure A6) to show the performance of the MLS method more intuitively. The strain fields are obtained from the test images imposing shear strain of 0.57% and volumetric strain of 0.04% on the shear band. For taking the influence of subset size into consideration, the displacement field is analyzed

with using $L = 25\,\text{px}$, $50\,\text{px}$, respectively. Based on each of the estimated displacement fields, the strains are computed by the two methods. Figure A5 shows the calculated maximum shear strain fields, where the grey lines indicate the boundaries of the preassigned shear band. Comparing the strain fields obtained with using different subset sizes, the zone of shear band is captured more precisely as $L = 25\,\text{px}$, while the strain fields are smoother as $L = 50\,\text{px}$. Comparing Figure A5(a) with Figure A5(b), it is observed that the strain fields computed by the MLS method are smoother, especially in the area where no shear strain is imposed. The effectiveness of the MLS method is more pronounced in the measurement of volumetric strain fields, which is illustrated in Figure A6. For the strain fields obtained from GeoPIV_RG (Figure A6(a)), a highly irregular strain distribution above the shear band is observed when $L = 25\,\text{px}$, and information of limited valuable is delivered. The irregularity is alleviated for $L = 50\,\text{px}$; however, the shape of the shear band is jagged and significantly different from what is preassigned. Comparing Figure A6(b) with Figure A6(a), it is identified that the smoothness and regularity of the strain fields are greatly improved by using the MLS method.

### A.3.2. Physical test

To evaluate the effectiveness of the MLS method in practical observation, we conducted a cutting test and calculated the incremental strain fields during the test by the two methods. The test was performed on the silica sand, obtained from Ottawa, Illinois (supplied by U.S. Silica Company). The particles are round in shape and range in size from $0.075\,\text{mm}$ to $0.425\,\text{mm}$ with a mean diameter of $D_{50} = 0.19\,\text{mm}$. In the test, the sand bed was prepared in a loose state with relative density $D_r = 18\%$ using fluidization [**219**]. After that, a plate was pushed vertically into the sand at a depth of 27 mm. Then, it was moved horizontally

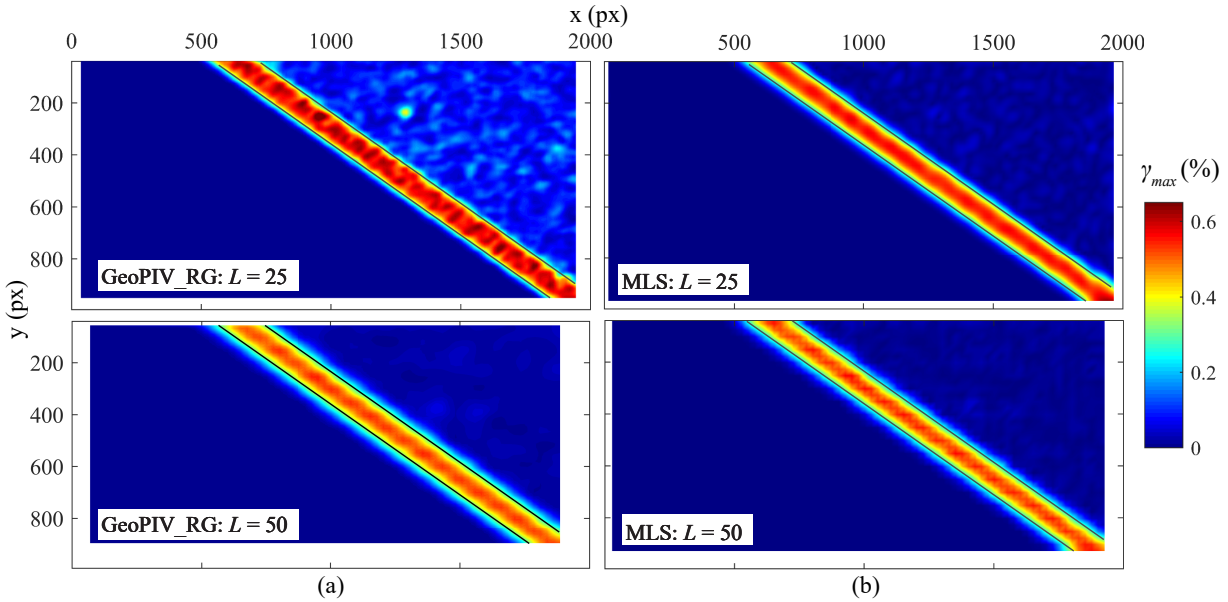


Figure A5. Shear strain field calculated by using (a) GeoPIV_RG; (b) MLS method. Note: the imposed shear strain is 0.57%, and the volumetric strain is 0.04%.

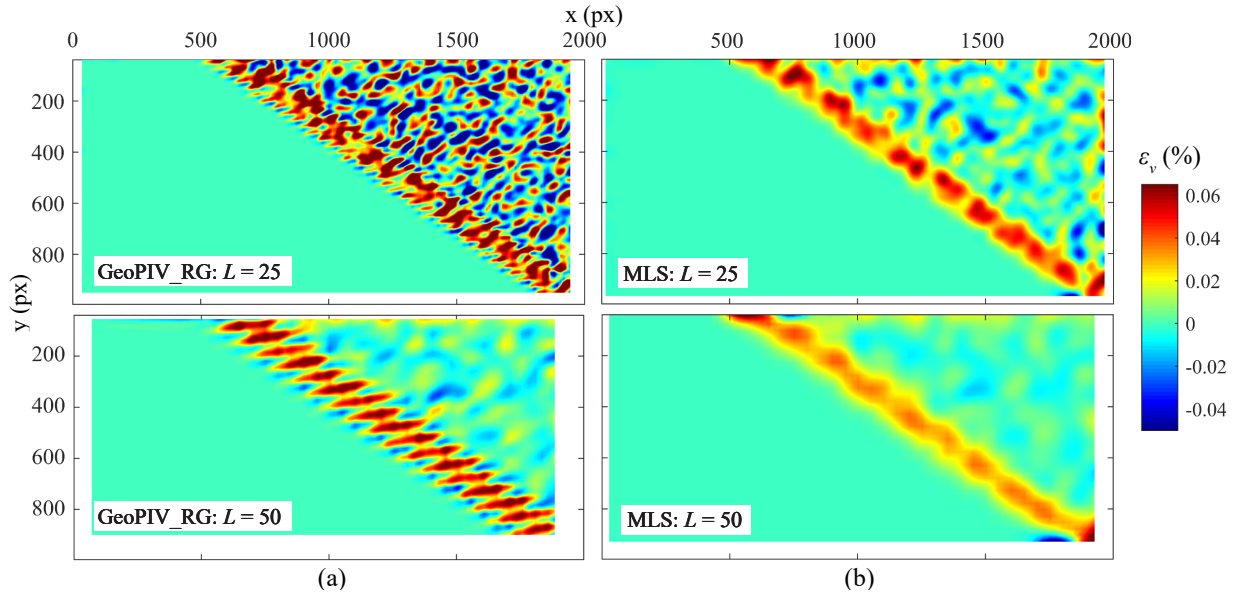


Figure A6. Volumetric strain field calculated by using (a) GeoPIV_RG; (b) MLS method. Note: the imposed shear strain is 0.57%, and the volumetric strain is 0.04%.

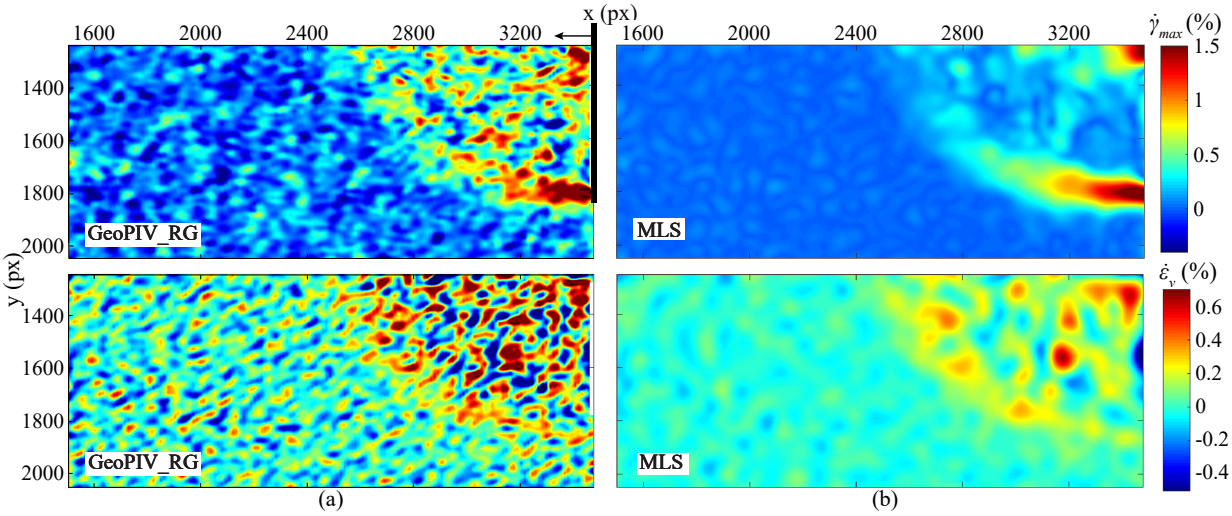


Figure A7. At the cutting displacement of 1 mm, the incremental shear strain field (top) and volumetric strain field (bottom) obtained by using (a) GeoPIV_RG; and (b) MLS method. Note: the incremental strains correspond to the incremental displacement of 0.1 mm, and black block represents the plate.

at a rate of 0.1 mm/s to cut the sand, and the pictures were taken per 0.1 s simultaneously during the process.

We used the subset size of 25 px to analyze the displacement field. For the test pictures, the minimum standard deviation of the subset intensities ($\sigma_{Is}$) is 25, satisfying the requirement on the contrast of subsets [**214**]. Figure A7(a) and (b) illustrate the incremental strain fields obtained from GeoPIV_RG and MLS method, respectively, which are plotted in pixel-based space. It is noted that the incremental strain fields are produced with a displacement of 0.1 mm when the cutting displacement $u = 1$ mm. From Figure A7(a), it is observed the strain fields measured by GeoPIV_RG, especially the volumetric strain field, are abnormal. By contrast, the strain fields computed by the MLS method (show in Figure A7(b)) are more rational as the abnormal patterns are alleviated, and the zone of strain localization can be detected.

## A.4. Summary

This study presents a technique using MLS interpolants to calculate strain distribution from the displacements at discrete positions obtained by PIV. The implementation of strain field measurement is described, and the influence of local support domain size on the calculation is investigated. Additionally, virtual tests and a physical test involving strain localization were performed. Through measuring the strain fields of the tests, the effectiveness of the MLS method is validated. The main conclusions are as follows:

(1) This technique mainly has three advantages: (1) the calculation process can be easily implemented when the displacements at discrete positions are obtained; (2) the strain can be calculated at arbitrary position in the full field, which means the positions for performing the strain calculation are not constrained by the grid/subsets defined for estimating displacements; (3) the local support domain size can be set arbitrarily, even vary at different positions, which might be helpful for obtaining optimal results with respect to different cases.

(2) The local support domain size $d_m$ is a key factor influencing the calculation result. As the imposed strains are different, the $d_m$ generating optimal estimation varies. The test performed in this study indicates that the $d_m$ corresponding to the minimum $NMAE_{\gamma_{xy}}$ increases with the decrease of the imposed shear strain, suggesting that a larger $d_m$ is preferred when the shear strain to be measured is small. In practice, a proper local support domain size should be selected carefully for observing the strain localization accurately.

(3) The proposed method is effective in measuring the strain field for observing strain localization. Based on the results of the virtual tests and a physical test, it is demonstrated that the MLS method can significantly improve the smoothness and regularity of the strain

fields to obtain valuable information of strain localization, especially for the volumetric strain field.